ABSTRACT

Implications of Soil Geochemistry for Understanding Agricultural Cultivation
by the Ancient Maya

Katarena Shiner, M.S.

Co-Mentor: Julie A. Hoggarth, Ph.D.
Co-Mentor: Stephen I. Dworkin, Ph.D.

The size and extent of Classic Maya population was dependent on the ability to produce crops through sustainable agricultural activities. The Maya used diverse cultivation systems including ditched fields. This study characterizes the geochemistry of soil profiles in a Maya ditched field near Baking Pot, Belize in order to investigate the effect of climate on Maya agriculture. The carbon isotopic composition of soil organic matter reveals that prior to Maya occupation the landscape was occupied by a mixed C_3 and C_4 plant community. Maya agricultural activity is recognized in the soil profiles by the most positive $\delta^{13}C$ values and a decline in soil phosphorous concentration, both of which are indicative of the cropping of maize. A return to more negative $\delta^{13}C$ values in the upper part of the soil profiles is indicative of cessation of Maya agricultural activity and a return to higher proportions of C_3 plants.

Implications of Soil Geochemistry for Understanding Agricultural Cultivation by the Ancient Maya

by

Katarena Shiner, B.S.

A Thesis

Approved by the Department of Geosciences

Steven Driese, Ph.D., Chairperson

Submitted to the Graduate Faculty of
Baylor University in Partial Fulfillment of the
Requirements for the Degree
of

Master of Science

Approved by the Thesis Committee

Stephen Dworkin, Ph.D., Co-Chairperson

Julie Hoggarth, Ph.D., Co-Chairperson

Steven Driese, Ph.D.

Joseph White, Ph.D.

Accepted by the Graduate School
December 2019

J. Larry Lyon, Ph.D., Dean

Page bearing signatures is kept on file in the Graduate School.

TABLE OF CONTENTS

LIST OF FIGURES

LIST OF TABLES

ACKNOWLEDGMENTS

I would like to thank my thesis advisors Dr. Julie Hoggarth and Dr. Steve Dworkin of Baylor University. Their doors were always open whenever I needed help or had a question about my research or writing. They consistently provided me direction, while allowing me to do my work. I would also like to acknowledge my committee members Dr. Joseph White and Dr. Steve Driese of Baylor University for their valuable input and comments on my thesis. Finally, I would like to thank Gary Stinchcomb for assistance with the mean annual precipitation data.

DEDICATION

To Erik and my family:
for their unfailing support and encouragement throughout my years of study.

CHAPTER ONE

Introduction

The growth and complexity that has been noted for Classic Maya civilization was dependent on their ability to produce crops through sustainable agriculture practices. Large populations require intensive agriculture, with soil that is replenished with nutrients naturally or anthropogenically (Sharer and Traxler, 2006). One of the primary crops grown in Mesoamerica was maize (*Zea mays*), which is the most visible cultigen in the paleoecological record and was the most important source of calories in Mesoamerica (Kaplan and Lynch, 1999; Kennett and Beach, 2013; Piperno et al., 2009; Piperno and Smith, 2012; Smith, 1997; Wahl et al. 2007). The Classic Maya were susceptible to drought and other climate variabilities due to their reliance on maize agriculture, as identified in archaeological and historic records (Hoggarth et al., 2016, 2017).

In the semitropical Belize Valley, the Maya experienced wet (June to November) and dry (December to May) seasons, and had to account for each season in their agricultural cultivation cycle (Lucero, 2011). Raised fields were built on seasonal flood plains that would otherwise have been unusable for agriculture, creating ideal growing conditions for agriculture during the wet season (Kennett and Beach, 2013). Evidence for intensive agriculture has been identified within a ditch field system in the western periphery of the site of Baking Pot, located approximately 10 km east of the modern town of San Ignacio and on the alluvial banks of the Belize River (Audet and Awe, 2004). This system of ditches in the Belize Valley were identified in 1980, based on examination of aerial photographs (Kirke 1980). Since that time, LiDAR data suggest that the ditched field system spans over 20km in linear ditch pathways (Ebert et al., 2016). Studies suggest the Maya used the fields for multiple reasons including: transportation, water management, and agriculture (Beach et al., 2009; Beach et al., 2011). Ceramics found in the same section as the ditches indicate that they were likely built during the Late Classic period (Conlon and Powis, 2004; Awe et al., 2014). Despite this information, questions remain over whether the ditches were established earlier in time and what types of plants were cultivated in this area. Many questions have been tested through the excavation of the ditched field systems. First, were the fields made by the Maya, or formed naturally? Second, if the ditched fields were built by the Maya, how intensive were their agricultural and water management systems? Intensive agricultural and water management systems would allow for populations to increase during the Classic period.

To further understand the vegetation cultivated in this area and the impact of climate on Maya agricultural practices, this study investigates soil geochemistry including the concentration of metals and the carbon isotopic composition of bulk soil organic matter from soil profiles. The concentration of metals within a soil is an indicator of weathering intensity that is primarily controlled by a combination of temperature and the abundance of precipitation. The carbon isotopic composition of soil organic matter can be used to identify corn cropping because the preindustrial average $\delta^{13}C$ value of C_3 plants is −26‰ PDB and the average $\delta^{13}C$ value of C_4 plants is −12‰ PDB (Webb et al., 2004; Tipple and Pagani 2007). Most of the tropical plants native to the Maya lowlands in Belize are C_3 in nature (Webb et al., 2004). The only C_4 plant known to be cultivated in this area is maize, indicating that unless the area was previously a grassland (of which are 50% are C_4 plants), high $\delta^{13}C$ values indicate the presence of cultivated maize (Tieszen et al., 1993; Webb et al., 2004). Therefore, an identifiable transition in carbon isotope ratios in soil profiles can be used to identify the transition from grassland/forest cover at Baking Pot to agricultural practices focused on growing maize.

Therefore, the goals of this study are to: 1.) investigate Maya agricultural practices using the carbon isotopic composition of soil organic matter, 2.) discern climatic changes during Maya occupation using elemental concentrations in soil profiles as an indicator of mineral weathering intensity, and 3.) investigate the impact of changing climate on the Maya culture.

CHAPTER TWO

Background

Research Area

Maya

The cultural history of the Maya can be divided into two distinct epochs, pre-Hispanic and the Post Conquest period (Beach et al, 2008). The pre-Hispanic period can be further subdivided into many cultural time periods, including the Archaic (8000-2000 BCE), the Preclassic period (ca. 2000 BCE-CE 250), the Classic period (ca. CE 250-900/1100), and the Post Classic period (ca. CE 900-1100/1500) (Sharer and Traxler, 2006). The Preclassic Period is subdivided into the Early Preclassic (2000-1000 BCE), the Middle Preclassic (1000-400 BCE), the Late Preclassic (400 BCE-CE 100), and the Terminal Preclassic (100-250 CE) (Sharer and Traxler, 2006). The Classic Period is subdivided into the Early Classic (ca. CE 250-600), the Late Classic (ca. CE 600-800), and the Terminal Classic (ca. CE 800-900) periods (Sharer and Traxler, 2006). The Post Classic Period is subdivided into the Early Postclassic (900-1250 CE), and the Late Postclassic (1250-1500 CE) (Beach et al., 2008).

Throughout the Maya lowlands, cultural developments occurred in a cyclical fashion, with periods of growth in political centralization and complexity followed by periods of decline, such as the periods of depopulation that are noted for the Terminal Preclassic and Terminal Classic periods (Beach et al., 2008). The Classic Maya collapse that occurred between 750-1000 CE was not simultaneous throughout Central America.

Whereas some sites experienced growth, others were abandoned permanently, abandoned for centuries, or never abandoned (Beach et al., 2008).

Belize River Valley

The Maya lowlands consist of the geographic area that encompasses southern Mexico, Belize, Guatemala, and parts of Honduras and El Salvador. Within this diverse area, Belize and southeastern Mexico can be divided into two tectono-morphological regions (Gischler and Lomando, 1999). The northern region is made of low-relief limestone of Tertiary and Quaternary age (Gischler and Lomando, 1999). In the southern region, the Maya Mountains are composed of Paleozoic shales, schists, granites, and Cretaceous limestones (Gischler and Lomando, 1999). The Yucatan carbonate platform is in the north where deformation is minimal (Marshall et al., 2007).

Located in western Belize, the Belize River Valley is associated geologically with a denuded karst plateau north of the Maya Mountains. During the Classic period, the area was home to several medium-sized political centers including Cahal Pech, Lower Dover, Xunantunich, Buenavista del Cayo, and Baking Pot (Figure 1). The location of the archaeological site of Baking Pot in western Belize lies along the southern bank of the Belize River, which drains fluviokarst topography (Beach et al., 2008) from its confluence near the town of San Ignacio to the Caribbean Sea.

Baking Pot

Radiocarbon dates from the site core at Baking Pot indicate that the earliest occupation of the site occurred during the Middle Preclassic period between 400 – 200 cal BCE (Hoggarth et al. 2014). During the Late Preclassic, the Maya Lowlands experienced population and settlement growth along with wetland agriculture expansion. It is during this same period when evidence suggests low-level construction in Group A at Baking Pot's site core (Sharer and Traxler, 2006; Hoggarth et al., 2014). Monumental construction expanded at Baking Pot in the Early Classic period (CE 250-600). Occupation continued during the Classic Period with a marked increase in construction and population during the Late Classic period (CE 600-800) (Hoggarth et al., 2014). Whereas Baking Pot experienced growth during this time, other sites in the Belize River Valley such as Xunantunich, underwent population decline or little growth (Yaeger, 2008).

Ditch fields were identified near Baking Pot in 1980, based on examination of aerial photographs (Kirke 1980). The ditches were arranged in a lattice system with straight waterways and rectangular plots between 50 – 120 m^2 (Awe et al., 2014; Kirke, 1980). Ceramics found in the same section as the ditches indicate that they were likely built during the Late Classic period when Baking Pot experienced population growth (Conlon and Powis, 2004; Awe et al., 2014; Hoggarth et al., 2014). This study builds on these previous examinations of Baking Pot's ditched field complex and focuses on using soil geochemistry and related methods to identify changes in agricultural signatures associated with the clearing of forest area, period of cultivation, and the cessation of use of the ditches around the time of abandonment in relation to climatic changes at the end of the Classic period.

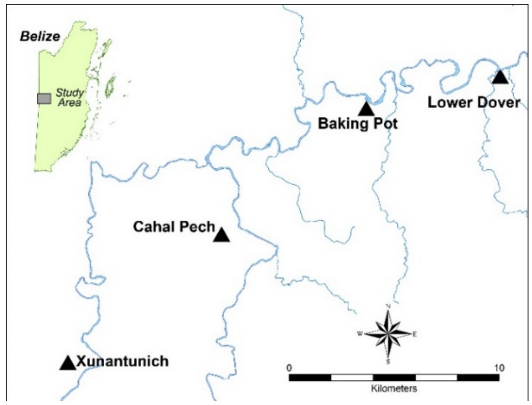

Figure 1: Map of the Belize River Valley (map by Claire Ebert, 2019)

Climate

Modern climate. The Maya lowlands, and therefore the Belize River Valley, is seasonally influenced by the Intertropical Convergence Zone (ITCZ) and the Bermuda High (Beach et al., 2008). The ITCZ and Bermuda High cause distinctive wet (June to October) and dry (December to May) seasons (Akers et al., 2019; Beach et al., 2008). The mean annual precipitation (MAP) range within the Belize River Valley is 1,350 to 3,700 mm/yr (Akers et al. 2016). The area is also influenced by the El Nino/Southern Oscillation (ENSO). ENSO causes variability in the climate over time and can influence tropical storm activity (Boose et al., 2003).

Paleoclimate. Paleoclimate evidence from precisely dated speleothems suggests that there were multiple droughts in the Maya lowlands at the end of the Classic Period (Akers et al., 2019; Evans et al., 2018; Medina-Elizalde et al. 2011; Kennett et al. 2012). Oxygen and carbon isotope ratios measured from speleothems in the Box Tunich (BZBTI) cave in the Belize River Valley and the Yok Balum (YOK-I) cave in southern Belize indicate that multiple multidecadal droughts occurred (Akers et al., 2019;

Kennett et al., 2012). The Yok Balum cave speleothem records indicate that severe droughts occurred between 200-300, 820-870, 1020-1100, 1530-1580, and 1765-1800 CE (Kennett et al., 2012). Speleothem records from the Box Tunich cave, located south east of Baking Pot, indicate that severe droughts occurred between 390-450, 695-860, 990-1090 CE that impacted the Maya Civilization (Akers et al., 2019). Baking Pot was occupied during the first severe drought in the Early Classic period. Occupation and population growth continued into the Late Classic (600-770 CE), indicating growth occurred at least partially during the severe drought between 820-870 CE (Kennet et al., 2012). Severe droughts had a significant impact on Classic Maya civilization, with general synchronicity between the timing of droughts and the collapse of political systems along with demographic decline in the mid-eighth to ninth centuries (Hoggarth et al. 2016; Kennett et al. 2012; Lucero 2011).

Maya Agriculture

Background. The size and extent of Classic Maya populations was influenced by their ability to produce and maintain sustainable agricultural systems. The primary crops grown in Mesoamerica were maize (*Zea mays*), squash (*Cucurbita pepo/Cucurbita argyrosperma*), and the common bean (*Phaseolus vulgaris*) (Kaplan and Lynch, 1999; Kennett and Beach, 2013; Piperno et al., 2009; Piperno and Smith, 2012; Smith, 1997). Swidden agriculture was the earliest form of cultivation by the Maya in which multiple crops were planted together, clearing, and burning were implemented (Sharer and Traxler, 2006). Fields become depleted of nutrients after multiple years of cultivation, therefore the Maya would leave fields fallow while new fields were cleared and planted

(Sharer and Traxler, 2006). Swidden agriculture was used by smaller population densities in areas that were large enough for extensive agriculture (Sharer and Traxler, 2006). Large populations throughout the Maya lowlands were in need of intensive agriculture, with soil that is replenished of nutrients naturally or anthropogenically (Sharer and Traxler, 2006). Methods of intensive agriculture include: house gardens, terraces, wetland agriculture systems (raised fields/ditch fields), and irrigation (Dunning et al. 1998; Sharer and Traxler, 2006). Terracing is used by the Maya in the highlands and hilly areas of the lowlands (Sharer and Traxler, 2006), allowing agriculture in areas that otherwise would not be conducive to cultivation. Intensive agricultural systems used at Baking Pot include terraces and wetland agriculture systems. This study focuses on the use of ditched fields in a wetland agriculture system.

Agricultural debate. During the 1960s-1980s a debate took place in the archaeological community on the ability of the Maya to live off swidden agriculture alone in the Maya lowlands. The most important aspect of an environment to a culture is the ability of the environment to produce sustainable agriculture (Meggers, 1954). There were discrepancies on population estimates in the Maya lowlands (Cowgill, 1962; Coe, 1965; Andrews, 1965) and the agricultural production estimates in an area of limited agricultural potential (Meggers, 1954). As population density estimates increased the belief that the Maya used only the swidden method decreased (Dunning et al. 2004). A study by Ursula Cowgill (1962), questioned modern farmers in the Maya lowlands on their use of fields over time, the amount of maize yielded after one to three years of use, and the time required for soil fertility to replenish after one to three years agricultural use. The results indicated swidden agriculture could provide subsistence to 100-200 people per square mile (Cowgill, 1962). This study increased the belief that the Maya could use swidden agriculture to sustain their populations in the lowlands due to the thought by some that lowland populations were within this range (Dunning et al. 2004). A study done by William Coe (1965) at the site of Tikal, Guatemala and a study by Wyllys Andrews (1965) who observed house mounds and monumental structures throughout the Maya lowlands, indicated the populations in the lowlands exceeded the 100-200 people per square mile limit; therefore, this evidence suggested that swidden agriculture would not be enough to maintain large populations overtime. With more archaeologists agreeing with the large population density estimates another forms of cultivation were necessary.

Wetland Fields

Wetland fields. Wetland fields were first identified in the 1970s and 1980s by air and aerial photographs indicating the Maya were using intensive canal systems (Siemens et al. 1972; Turner et al., 1974; Kirke et al., 1980). Turner (1974) and Siemens (1972) were quick to hypothesize the connection of the canal systems to agriculture use. This form of intensive agriculture would solve the disconnect between high populations in the Maya Lowlands and the lack of environmental potential for wide spread agriculture (Meggers, 1954). Others debated the use of the canals after their identification arguing the canal systems were not built by the Maya, but naturally occurring. One leading argument for the natural canal system pattern was that they were gilgai (Turner et al., 1981). Gilgai are formed in expandable clays in season wet and dry environments, they are large cracks on the surface formed when clays dry in the dry season, being the canals, while the raised areas could be formed when clays expand during the wet season (Wood et al., 1978). Another argument for the canal pattern forming naturally is the precipitation of gypsum during sea level rise in the Preclassic, while the aggraded areas formed from aggradation of clays due to increased erosion (Pope et al., 1996; Beach et al., 2009). They were both dismissed as the primary cause of the canal systems because gilgai have smaller hummock depressions and neither form deep linear canal features to that extent (Beach et al., 2009)

Locations and use. Wetland fields were used by ancient populations at multiple sites across the Maya lowlands, Mesoamerica (Jacob, 1995), ancient China, New Guinea, and Angkor Wat (Beach et al., 2019). Throughout the literature, the term "wetland fields" is used to encompass multiple agricultural fields including raised fields and ditched fields (drained fields/channelized fields) (Jacob, 1995). Areas that are prone to seasonal or permanent inundation like riverine lands and depressions (bajos, akalches, savannas, swamps, and marshes) are popular sites for ditch fields (Jacob 1995; Lundell 1937; Siemens 1972). In some areas, the Maya used the water in the canals in raised fields to raise fish as food (Sharer and Traxler, 2006). Ditched fields in river valleys are replenished in nutrients by silt deposited during flooding events (Sharer and Traxler, 2006), this likely helped with replenishing soil fertility at Baking Pot. Multiple studies suggest that the Maya used the fields for multiple other reasons including transportation and water management (Beach et al., 2009; Beach et al., 2011).

Previous studies. Wetland fields were used by the ancient Maya at several sites across the northern and southern lowland area (Jacob, 1995). Isotopic methods were utilized to understand wetland fields at Birds of Paradise Fields (BOP) and Chan Cahal

Fields near Blue Creek, Belize by Beach et al., (2009). At the BOP locality 10 canal profiles were analyzed for their carbon isotopic composition with depth. At BOP 1, in the sub canal sediments the soil had a $\delta^{13}C$ of -24.7‰, which increased gradually up-profile to -19.6‰, followed by a decrease in the surface soil to -27.3‰ (Beach et al., 2009). BOP 1 also had macrobotanical, phytolith, and pollen evidence of grasses and charcoal indicating agricultural anthropogenic impacts on the soil (Beach et al., 2009). Similar results were found in canals 3, 7, and 10. Soil from Chan Cahal locality exhibited similar isotopic trends at the 66T canal from $\delta^{13}C$ of -28.2‰ in the Preclassic sub-canal sediments, which increased to -24.1‰ for the Late Classic canal fill and returned to -28.3‰ at the surface (Beach et al., 2011). Using the correlation between phytoliths, pollen, and the positive changes in the $\delta^{13}C$ values, it was hypothesized that maize cultivation caused the increase in $\delta^{13}C$ within the preserved horizon displaying the influence of C_4 plants.

Another study was conducted by Kristofer Johnson, David Wright, and Richard Terry (2007), at the site of Aguateca in the Petexbatun Region of Guatemala with similar results. In 2002, 14 soil profiles in wetlands around Aguateca were examined in the field and later analyzed for $\delta^{13}C$ values (Johnson et al., 2007). Within Profile 1, classified as an Aquertic Argiudolls the $\delta^{13}C$ of the soil organic matter (SOM) was -20.3 ‰ between 40-80 cm depth and decreased to approximately -28‰ near the surface (Johnson et al., 2007). The higher values with a difference of 7.7 ‰ indicates the change was associated with the introduction of *Zea mays* cultivation (Johnson et al., 2007). Similarly in Profile 4, between 25-75cm the SOM $\delta^{13}C$ value was -19.07 ‰ and decreased to -24.9 ‰ near the surface displaying an overall change of 4.6 ‰ (Johnson et al., 2007). The significant change from the subsurface to the surface was interpreted to indicate that there was cultivation of *Zea mays* within the wetland fields near Aguateca.

Soils

The soils in the Baking Pot ditched field area are broadly classified as USDA Ultisols. Ultisols are formed in humid environments with seasonal rainfall (Soil Survey Staff 2014). Ultisols are strongly weathered and have an upper horizon that is commonly a light-colored grayish horizon overlying a yellowish brown to reddish argillic (clay accumulation) or kandic (very low cation-exchange capacity) subsoil horizon (Soil Survey Staff 2014). They commonly form on old terrain and parent material that is felsic and noncalcareous (Markewich et al., 1991). The field and canal profiles near Baking Pot were relatively deep, extending down to 2.6 meters from the modern surface without any sign of bedrock. Given that the field system at Baking Pot is located on a flood plain of the Belize River, the soils are likely cumulate and experienced sediment accumulation due to periodic flooding events. The canal and field soil profiles do not have distinct horizonation past the A horizon (Figure 2). Soil color is brown to light gray within the A horizon followed by multiple inferred clay-rich reddish brown to orange subsoil Bw or Bt horizons. The soils in this region are in the Udic moisture regime with isohyperthermic temperature regimes (Beach et al., 2008). Ultisols are highly weathered soils leached of most cations and nutrients, making them generally poor soils for agriculture.

Figure 2: Canal 8 displaying little horizonation past the A horizon (depth of profile 210 cm)

Geochemical Background

C_3 vs C_4 Plants

The different photosynthetic pathways of C_3 and C_4 plants result in distinct $\delta^{13}C$ values within the organic matter of the soil. During C_3 photosynthesis, atmospheric CO_2 is fixed to ribulose 1,5-bisphosphate (RuBP) by the Rubisco enzyme (Tipple and Pagani 2007). Fixation to Rubisco forms an enzyme-bound molecule, 2-carboxy-3-ketorabinitol-1,5-bisophate, that is hydrolyzed to two molecules of 3-phosphoglycerate (Tipple and Pagani 2007). The two 3-phosphoglycerate molecules are phosphorylated to 1,3-bisphoglycerate and reduced to glyceraldehydes-3-phospate (G3P) (Tipple and Pagani 2007). The creation of G3P is a three-carbon sugar, thus the origin of the name C_3 plant.

The C_4 photosynthetic pathway has a series of biochemical reactions before the Calvin-Benson cycle that take place within two cell types: mesophyll and bundle-sheath cells (Tipple and Pagani 2007). Prior to the Calvin-Benson cycle within the mesophyll cells, aqueous bicarbonate (HCO_3^-) is fixed to phosphoenolpyruvate (PEP) by phosphoenolpyruvate-carboxylase (PEP-C) which yields a four-carbon acid named, oxaloacetate (Tipple and Pagani 2007). Oxaloacetate (four-carbon acid) is the origin of the title C_4 plants. Oxaloacetate is transported from the mesophyll cell to the bundle-sheath cells (Tipple and Pagani 2007). The oxaloacetate is then decarboxylated causing a release of CO_2 that is used in the Calvin-Benson cycle (Tipple and Pagani 2007). The attraction of PEP-C for HCO_3^- causes enzyme saturation of CO_2, allowing C_4 plants to decrease stomatal width along with a reduction in transpiration (Taiz and Zeiger 1998). The higher rate of carbon assimilation make C_4 plants more conducive under conditions of high water-stress (Tipple and Pagani 2007). Therefore, C_4 plants are better adapted to dry, hot, and high-light environments (Sage et al. 1999). More than two-thirds of subtropical grasses are C_4 plants (Sage 2001).

Isotopes

Soil organic-carbon isotope ratios are influenced by changes in vegetation (Beach et al., 2006, 2008, 2009; Wright et al., 2009). The carbon isotopic composition of plants is a function of the carbon isotopic composition of the atmosphere ($\delta^{13}C_{CO2}$) and the partial pressure of atmospheric carbon dioxide ($_pCO_2$) inside the leaf (p_i) compared to atmospheric pCO_2 (p_a) (Tipple and Pagani 2007; Farquhar et al. 1989). The $\delta^{13}C$ value in C_3 plants is represented by Equation 1 below where *a* is the fractionation of the carbon isotope that takes place during diffusion of CO_2 into the leaf (4.4‰) and *b* is the fractionation resulting from carboxylation by Rubisco (27‰) (Tipple and Pagani 2007; Farquhar 1983). The $\delta^{13}C$ value in C_4 plants is represented by Equation 2 where all variable are the same and b_4 is the "fractionation associated with carboxylation of PEP-C

(-5.7‰), and Φ is the proportion of carbon fixed by PEP-C that leaks out of the bundle sheath cell" (Tipple and Pagani 2007; Farquhar 1983).

$$\delta^{13}Cc_{3plants} = \delta^{13}Cco_2 - a - (b - a)\frac{p_i}{p_a} \tag{1}$$

$$^{13}Cc_{4plants} = \delta^{13}Cco_2 - a - (b_4 + b\Phi - a)\frac{p_i}{p_a} \tag{2}$$

The range of $\delta^{13}C$ values for C_3 plants is between −23‰ to −34‰ PDB, with a preindustrial average value of −26‰ (Smith, 1971; Webb et al., 2004). Most of the tropical plants native to the Maya lowlands in Belize are C_3 (Webb et al., 2004). C_4 plants make up approximately half of the tropical grasses and two-thirds of subtropical grasses, including maize and have a carbon isotope range of −9‰ to −17‰, with an average preindustrial value of approximately −12‰ (Smith, 1971; Webb et al., 2004; Tipple and Pagani 2007).

Maize is the only C_4 plant known to be cultivated in this area and if it is present for extended periods of time then comparable amounts of C_4-derived carbon will be retained in the soil for hundreds to thousands of years; therefore, high $\delta^{13}C$ values can indicate the presence of cultivated maize (Tieszen et al., 1993; Webb et al., 2004). An identifiable transition in carbon isotope ratios can be used to identify the transition from grassland/forest cover in a region, to agricultural practices focused on growing maize.

Other influences on the $\delta^{13}C$ of soil organic matter are temperature, relative humidity, canopy effects, and water-use efficiency (Tieszen, 1991; Johnson et al., 2007). The $\delta^{13}C$ of soil organic matter (SOM) can decrease by 1-3‰ with an increase in depth within the soil profile when there is little to no change in vegetation (Balesdent et al., 1993; Powers and Schlesinger, 2002). Enrichment of SOM $\delta^{13}C$ in deeper soil horizons is attributed to: (1) soil microbes causing fractionation of ^{13}C in vegetation litter, (2) soil microbes preferentially decomposing vegetation litter and SOM, (3) soil carbon mixing, and (4) introduction of ^{13}C reduced CO_2 from fossil fuel combustion in the atmosphere (the Suess effect) (Boutton, 1996; Ehleringer et al., 2000).

The most important factors that impact the ^{13}C in SOM at deep depths are soil microbes causing fractionation of ^{13}C in vegetation litter and soil carbon mixing (Ehleringer et al., 2000). These factors have not produced a $\delta^{13}C$ enrichment of more than 4‰; therefore, a change between the subsoil and the surface of more than 4‰ is commonly explained by a change in vegetation from C_3 to C_4 plants (Martinelle et al., 1996).

Elements in Soil

The formation of soil is controlled by climate, organisms, relief, parent material, and the extent of diagenesis (Jenny, 1941). The concentration of different elements within an ancient soil can give insight into the paleoclimate and paleoenvironment of an area. The amount of chemical weathering is related to mean annual precipitation (MAP) and the mean annual temperature (MAT) (Sheldon et al., 2002). When precipitation and temperature increase, alkali and alkaline earth elements are depleted within soils through hydrolysis as primary soil minerals are converted to clay minerals (Sheldon et al., 2002). The base cations lost during weathering include MgO, CaO, Na_2O, and K_2O; therefore, these elements are the most useful for determination of the degree of weathering within a soil (Retallack 2001). Key soil-forming chemical reactions include hydrolysis, oxidation, hydration, dissolution, alkalization, reduction, dehydration, and precipitation (Retallack

2001). Major trends in these chemical reactions over time during burial can be inferred through the calculation of molecular weathering ratios (Retallack 2001).

Hydrolysis through the reaction of carbonic acid and cation rich minerals creates clay minerals and cations within soils (Retallack 2001). Hydrolysis causes the breakdown of silicate minerals and accumulation of clay minerals within soil (Retallack 2001). The cations are removed through aqueous transport or biologic agents (Retallack 2001). The extent of hydrolysis is estimated using molecular weathering ratios of alumina/bases, alkaline earth metals/alumina, silica/alumina, and barium/strontium (Retallack 2001). When alumina/bases are near 100 this indicates the soil is well developed and likely and Oxisol or Ultisol (Retallack 2001).

Maize has a high nutrient requirement, although variations in nutrient demand vary between different maize genotypes (Zhu et al., 2005). Therefore, the phosphorus concentration in soil can give insight into the potential productivity of the soil or how much phosphorus was depleted due to intensive agriculture. The presence of phosphorus in soil is controlled by an inorganic and organic cycle (Tate and Salcedo, 1988). The inorganic cycle consists of transformation of pedological phosphorus through changing acidity and leaching in the soil (Tate and Salcedo, 1988). Iron, aluminum, and calcium phosphates are not very soluble and significantly influence the concentration of phosphorus into soils (Tate and Salcedo, 1988). The organic cycle is driven by the use of phosphorus in living cells during the energy transport process (Tate and Salcedo, 1988). Microorganisms within the soil are a source of potential nutrients, including phosphorus, and are the primary agents of organic decomposition in soil (Tate and Salcedo, 1988). Additionally, phosphorus is more abundant near the surface than in the lower horizons due to the accumulation of organic matter (Zhu et al., 2005). In present day agricultural soils fertilization increases phosphorus on the surface accompanied by slow passage of phosphorus into the lower horizons (Zhu et al., 2005). In both instances, phosphorus availability is highest at the surface and decreases significantly into the deeper subsoil horizons (Zhu et al., 2005).

CHAPTER THREE

Methods

Field Methods

Location

The ditched field system studied for this project is located in the western periphery of Baking Pot, in an area of land owned by the Bedran family and associated with the Bedran Plazuela group (Figure 3). Baking Pot is approximately 9.4 km from the town of San Ignacio, Belize (Ebert et. al 2016).

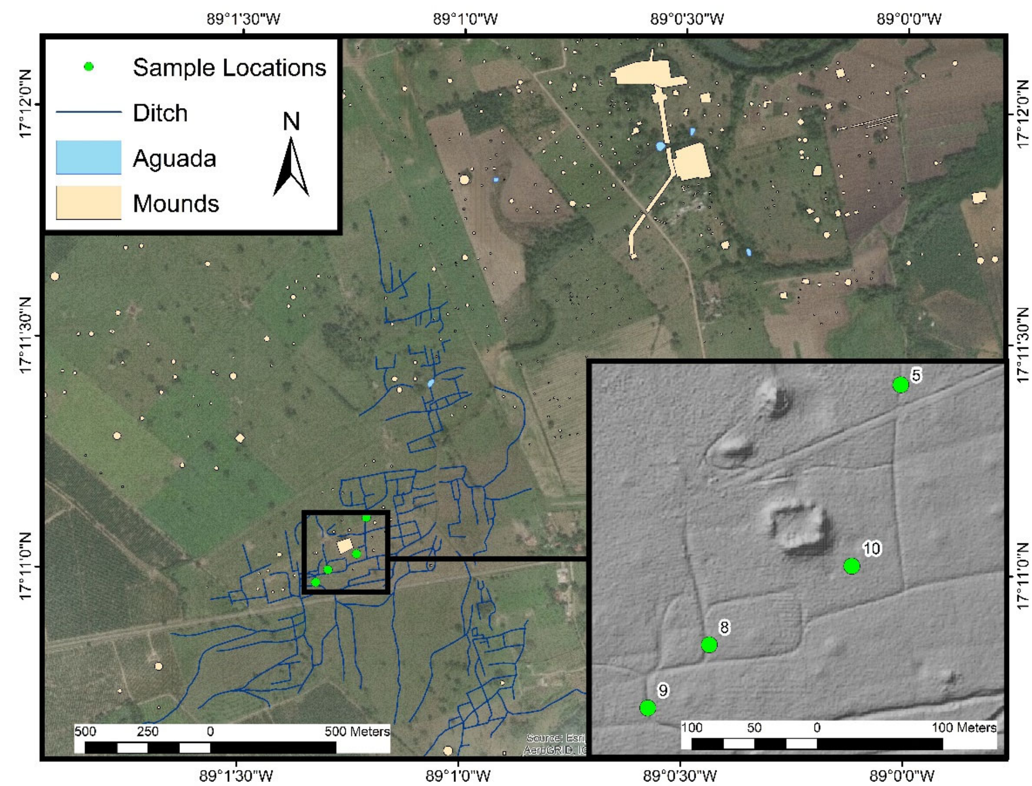

Figure 3: An aerial view of the ditched fields south west of Baking Pot and the locations of excavations.

Sample Collection

Sites were chosen for excavation based on the proximity to the archeological site of the Bedran Group within the ditched field, and evidence of modern anthropogenic alteration to the canal. Three canal types are located at within the field ranging between narrow shallow canals (Type A) to steep meandering creek like canals (Type C) (Kirke, 1980; Ebert et al., 2016). Type A and type B were the primary types chosen for observation. At each site, samples were collected from two profiles: 1.) the field profile, where maize likely grew and 2.) the canal profile, where water drained from the field (Figure 4). Soil profiles were exposed in both the fields and the canals by digging trenches with a backhoe. Samples were collected from the trenches every ten centimeters from the surface. Field sites one and two were collected during the summer of 2017 as part of preliminary research and were therefore not excavated as deep as sites excavated during 2018. Sites five, eight, nine and ten were collected during the summer of 2018 and excavated to approximately 2.5 m, below the level in which the visible soil change for the canal was identified.

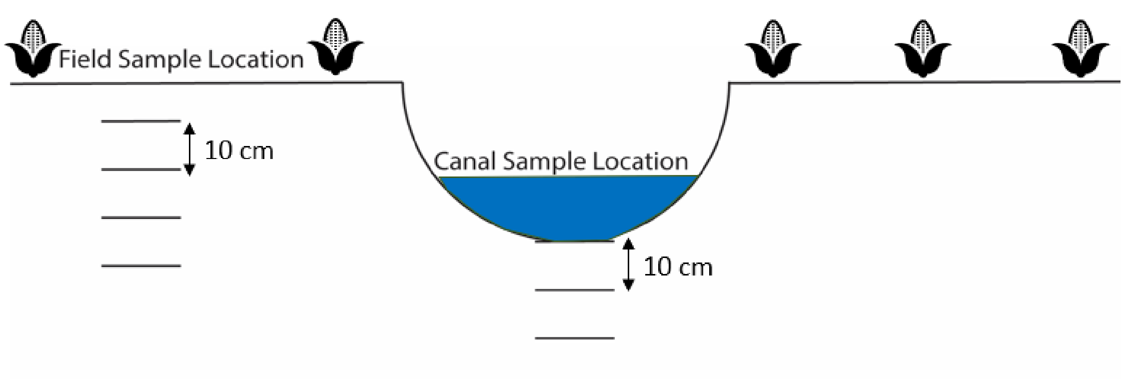

Figure 4: The relationship between the location of field samples collected and canal samples collected.

Lab Methods

Isotope Methods

Carbon and nitrogen isotope ratios were measured using stable isotope mass-spectrometry. Approximately, 20-30 g of soil were dried in an oven at 70-80°F (21.1-26.7°C) and then ground with a SPEX Shatterbox®. Approximately 30 mg from each sample were weighed into a tin capsule and combusted in a Costech EA (model 4010) to assess carbon and nitrogen content. The gases were conveyed from the EA to a Thermo Scientific™ Delta V™ Isotope Ratio Mass Spectrometer where carbon and nitrogen isotope ratios were measured.

Mixing Model

A mixing model was constructed to determine the abundance of C_4 plants contributing to the SOM (Figure 5). The endmember value for C_3 plants was assumed to be -26.7‰ PDB and the endmember value for C_4 plants was -12.5‰ PDB.

$$\%C_4 = 7.0423 * \delta^{13}C + 188.03 \tag{3}$$

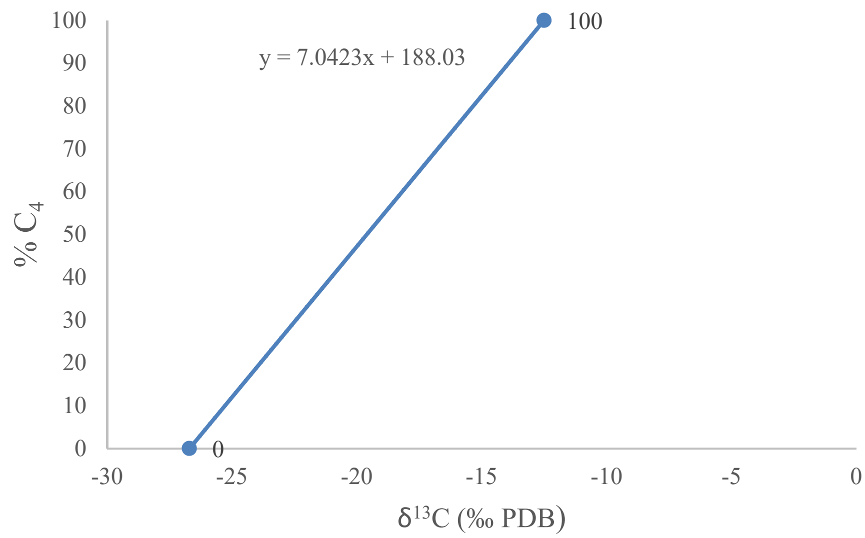

Figure 5: Mixing model used to calculate the abundance of C_4 plants.

Elemental Analysis

Major elements concentrations were measured using a Rigaku wavelength dispersive X-ray fluorescence (XRF) instrument. Soil samples were made into glass discs by weighing out 0.6000 +/- 0.0001 grams of powered sample which were then mixed with 6.000 +/- .0003 grams of lithium borate (flux). The concentrations of eleven elements was determined including Na, Mg, Al, Si, K, Ca, Ti, Fe, P, Mn and Zr. The transfer functions for the soil-forming chemical reaction hydrolysis is presented in equation 4 below (Retallack 2001).

$$Hydrolysis = \frac{Al_2O_3}{CaO + MgO + K_2O + Na_2O} \tag{4}$$

Mean Annual Precipitation

The chemical index of alteration without potash (CIA-K), is a precipitation proxy based on the modern relationship of MAP with the major-element chemical analyses of 126 North American Soils (Sheldon et al., 2002). Sheldon, Retallack, and Tanka (2002) conducted various trials to discern the most accurate relationship between these cations and the degree of weathering within paleosols. The most robust relationship was between the mean annual precipitation and the chemical index of alteration without potassium within Bt or Bw subsoil horizons (Sheldon et al., 2002). Mean annual precipitation was calculated using equation 7 and equation 8 displayed below (R^2=.72) (Sheldon et al., 2002). Additionally, the CIA-K value can also be used to distinguish between Alfisols and Ultisols (CIA-K > 80) (Sheldon et al., 2002). The modern precipitation range within the Belize River Valley is 1,350 to 3,700 mm/yr (Akers et al. 2016). Because the CIA-K equation is most useful in areas with a MAP range of 200 to 1600 mm/yr (Sheldon et al., 2002), the results presented here should be taken as a probable indicator of lower-estimate trends in MAP and are used instead for soil identification.

$$CIA - K = \frac{Al_2O_3}{Al_2O_3 + CaO + Na_2O} \tag{7}$$

$$MAP = 221e^{0.0197(CIA-K)} \tag{8}$$

A second way to estimate the MAP is by using the paleosol-paleoclimate model ($PPM_{1.0}$), which is a data focused model that uses the geochemistry of subsoil horizons in multiple environments to predict the MAP and MAT of a soil. The model was created using 685 mineral soil B horizons forming in MAP environments ranging from 130 to 6900 mm/yr and MAT ranging from 0 to 27 °C (Stinchcomb et al., 2016). The soils were combined in a partial least squares regression (PLSR) and a nonlinear spline to understand which regressor would predict MAP and MAT most accurately (Stinchcomb et al., 2016). Gary Stinchcomb (PhD) at Murray State University ran the XRF results through this model and provided the MAP results. The model predicted a low, best, and highest MAP value in mm/yr. Due to the wide precipitation range that this model is designed to predict it will likely provide a better estimate of MAP than CIA-K.

CHAPTER FOUR

Results and Discussion

Organic Carbon Abundance

Fields

The average organic carbon content in the A horizon is 1.7 wt.%. Organic carbon abundance is highest in the A horizons and begins to decrease in the transitional area between the A and underlying Bw horizons. With increasing soil depth, the wt. % organic C decreases rapidly and stabilizes at an average value of 0.25 wt.% (Figure 6). In field locations 1 and 2, the organic carbon content is higher throughout the profile than in the other field profiles although the decline in OC with depth is similar. The soil profile at Field site 10 has a lower organic carbon content at the surface, but it also follows a similar trend to the other field profiles below the surface.

Drainage canals

Within the canal profiles, the organic carbon content in A horizons is typically higher than the field locations although the trend of decreasing wt. % C with depth is similar (Figure 7). The average organic C content within the canal A horizons is 1.52 wt.%. Organic carbon decreases gradationally within the transition from the A horizon to the underlying Bw horizons. After this interval, the organic C decreases more rapidly with depth in Canal sites 5-9 to a value of approximately .18 wt.%. Canal 10 exhibits a more complex pattern of OC decline with two intervals of stable C values. The first has a value at approximately 0.52 wt.% followed by a decrease to approximately 0.13 wt.%.

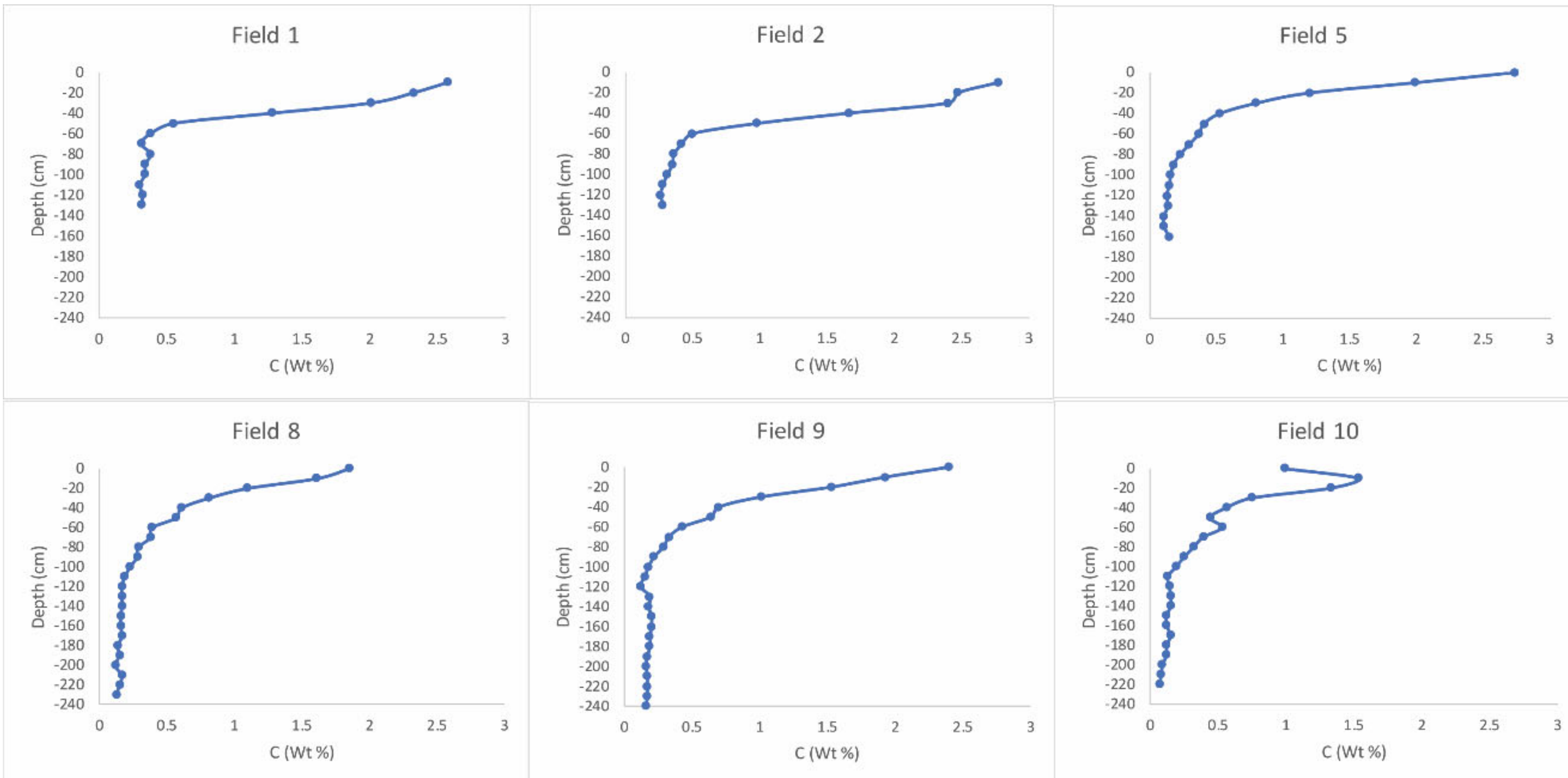

Figure 6: The total soil organic carbon content within the field profiles in weight percent with depth.

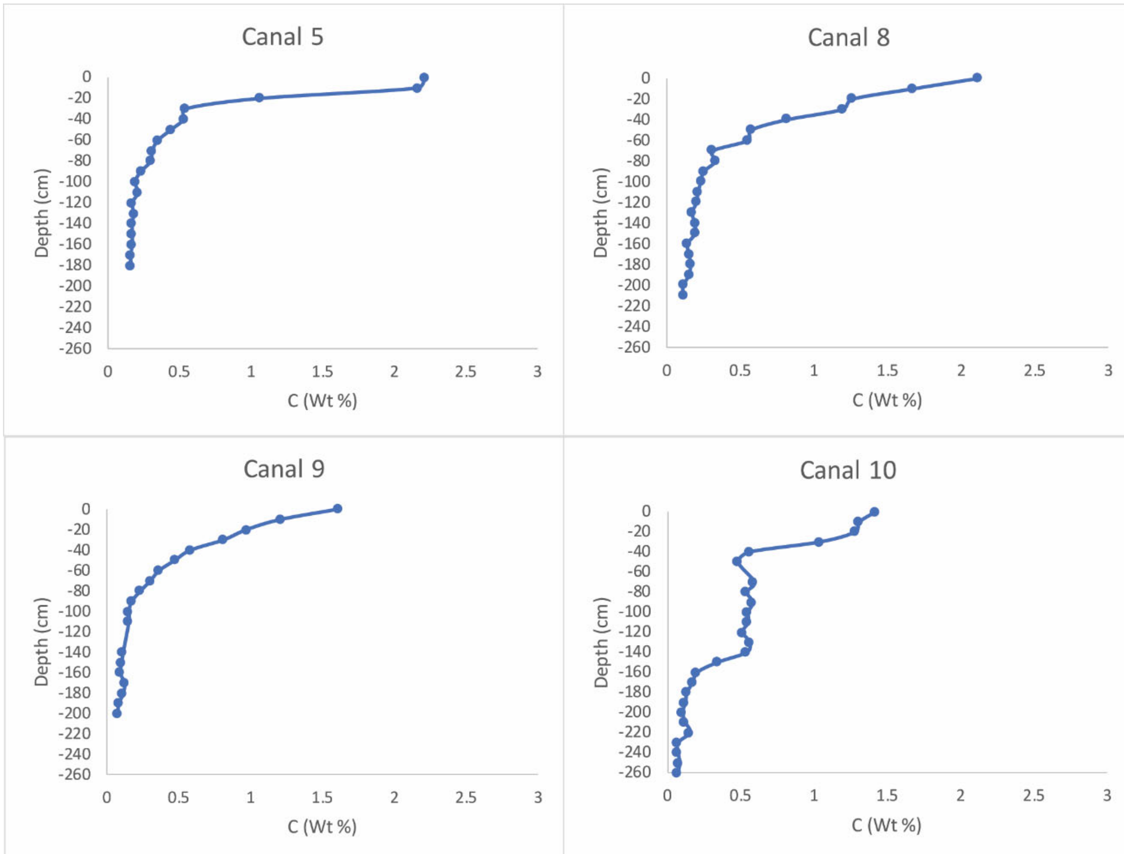

Figure 7: The total soil organic carbon within the canal profiles in weight percent with depth.

Carbon Isotope Ratios from the Field and Canal Soil-Profiles

Three distinct time periods were identified based on the trends of $\delta^{13}C$ in the canal and field profiles (Figure 8, 9, 10 and11). The first period represents the pre-Maya time period and is observed in the lower parts of the soil profiles where the SOM has the most negative carbon isotope ratios. The pre-Maya period consistently is observed in the soil profiles at 80 cm below the surface to the base of the soil profiles. The pre-Maya soil horizons have OC with $\delta^{13}C$ values that are the most negative, with an average $\delta^{13}C$ value of -20.2‰ in the field profiles and -19.6‰ in the canal profiles. Two isotopic trends were identified in the pre-Maya period. The first is from the base of the canal and field profiles to approximately 160 cm. These values are the most negative across the profiles with an average $\delta^{13}C$ value of -21.4‰ in the field profiles and -20.8‰ in the canal profiles. These light carbon isotope ratios indicate a mixed plant community with approximately 40% C_4 vegetation.

The second isotopic trend is identified as a carbon isotope excursion between approximately 160-80 cm. The $\delta^{13}C$ values within this section of the pre-Maya period become less negative up the profile. The average $\delta^{13}C$ value of this section is -19.4‰ in the fields and -16.6‰ in the canals. These enriched carbon isotope rations are equal to 58% C_4 in the field profiles and 51% C_4 in the canal profiles. This is consistent with plant communities in virgin grasslands in this area which are known to be a mixture of roughly 50% C_3 and C_4 grasses (Webb, 2004); therefore, this area may have previously been a mixed community grassland or forest before the Maya began cultivation.

The second period is the Maya occupation period that probably corresponds to the Early Classic Period (250-600 CE) through the Terminal Classic Period (600-900 CE). The occupation period was identified by the enrichment of the heavier carbon isotope in association with Maya Classic to Late Classic ceramics. The peak of the $\delta^{13}C$ values likely occur during the Late Classic to Terminal Classic Periods when the Baking Pot site was experiencing population growth, influx in monumental architecture, and abundant agricultural activity (Hoggarth et al., 2014). The occupation period is stratigraphically located from approximately 30 cm below the current land surface to the top of the pre-Maya period at 80 cm. During the period of occupation, the $\delta^{13}C$ values of soil organic matter increases and reaches their maximum values between 40 cm to 70 cm below the current land surface reaching approximately 65-85% C_4 vegetation. The $\delta^{13}C$ values in the occupation period in the field and canal profiles range between -19.9‰ to -14.7‰. Canal 8 site has the least negative $\delta^{13}C$ values across all the profiles collected at -14.7‰ and 84.7% C_4 vegetation. In the Field 10 site and Canal 8 site, this peak correlates with the occurrence of Late Classic (600-800 CE) ceramics and chert flakes supporting the interpretation that the change in isotope ratio is influenced by Maya agriculture. The canals also had less negative $\delta^{13}C$ peak values in the occupation period. This could be explained by the accumulation of C_4 plant-derived organic matter during the growth of maize and the runoff after the ditched fields were no longer in use. Field site 1 and field site 2 were not excavated deep enough to show the pre-Maya period.

A change between the subsoil and the surface of more than 4‰ is attributed to either a change in vegetation type, or to a change from C_3 to C_4 dominance (Martinelle et al., 1996). Every canal profile displayed a change greater than 4‰ from the base of the profile to the peak interval. The length of roots in *Zea mays* can be up to 130 cm (Mi et al., 2016), therefore, the gradual increase in the heavier carbon isotope (less negative $\delta^{13}C$ values) above 140 cm in the pre-Maya period could be attributed to maize root decomposition in the profile. The canals have a higher $\delta^{13}C$ peak average value at -15.5‰ equating to 78% C_4 plants, whereas the fields were at -16.4‰ and 73% C_4. The $\delta^{13}C$ values in the canals may be less negative due to the accumulation of maize-derived organic C detritus within the canal.

The third period is the post-Maya period representing modern soil accumulation after the abandonment of the agricultural field. This layer mostly consists of the A horizon and upper Bw1 horizon. Within the post-Maya layer, the $\delta^{13}C$ values exhibit a decline within a range of -20.8‰ to -16.2‰ indicating an increase in C_3 vegetation. The canals displayed a more significant shift to C_3 vegetation in the A horizon than the field profiles equating to 63.8% C_4 plants in the canals and 67% C_4 plants in the fields. A stronger decrease in $\delta^{13}C$ values was expected after Maya agricultural activity ceased, however, the lack of a strong return to pre-Maya values may be due to an increase in C_4 grasses growing on the flood plain today.

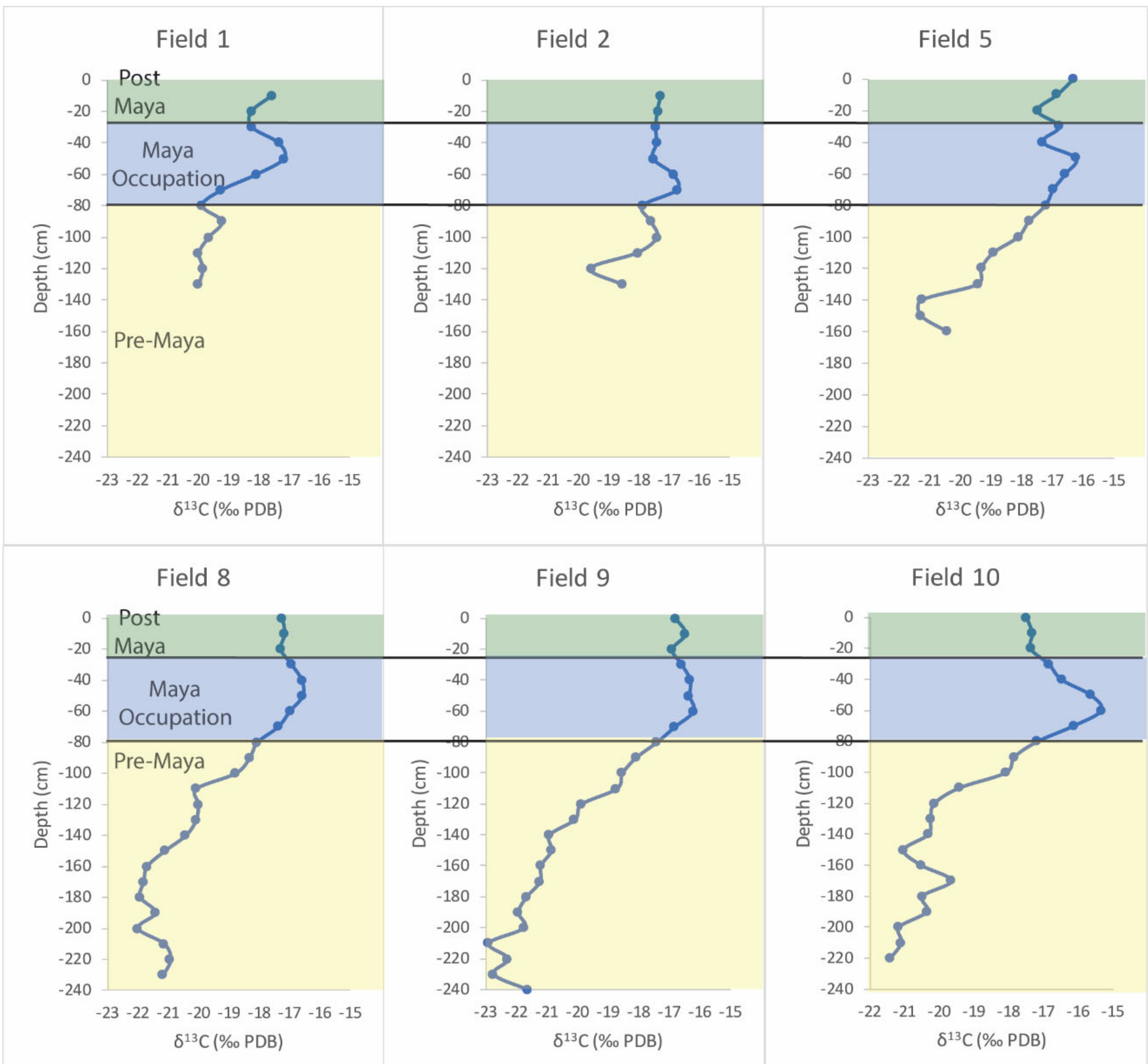

Figure 8: Carbon isotopic soil profiles from field sample locations.

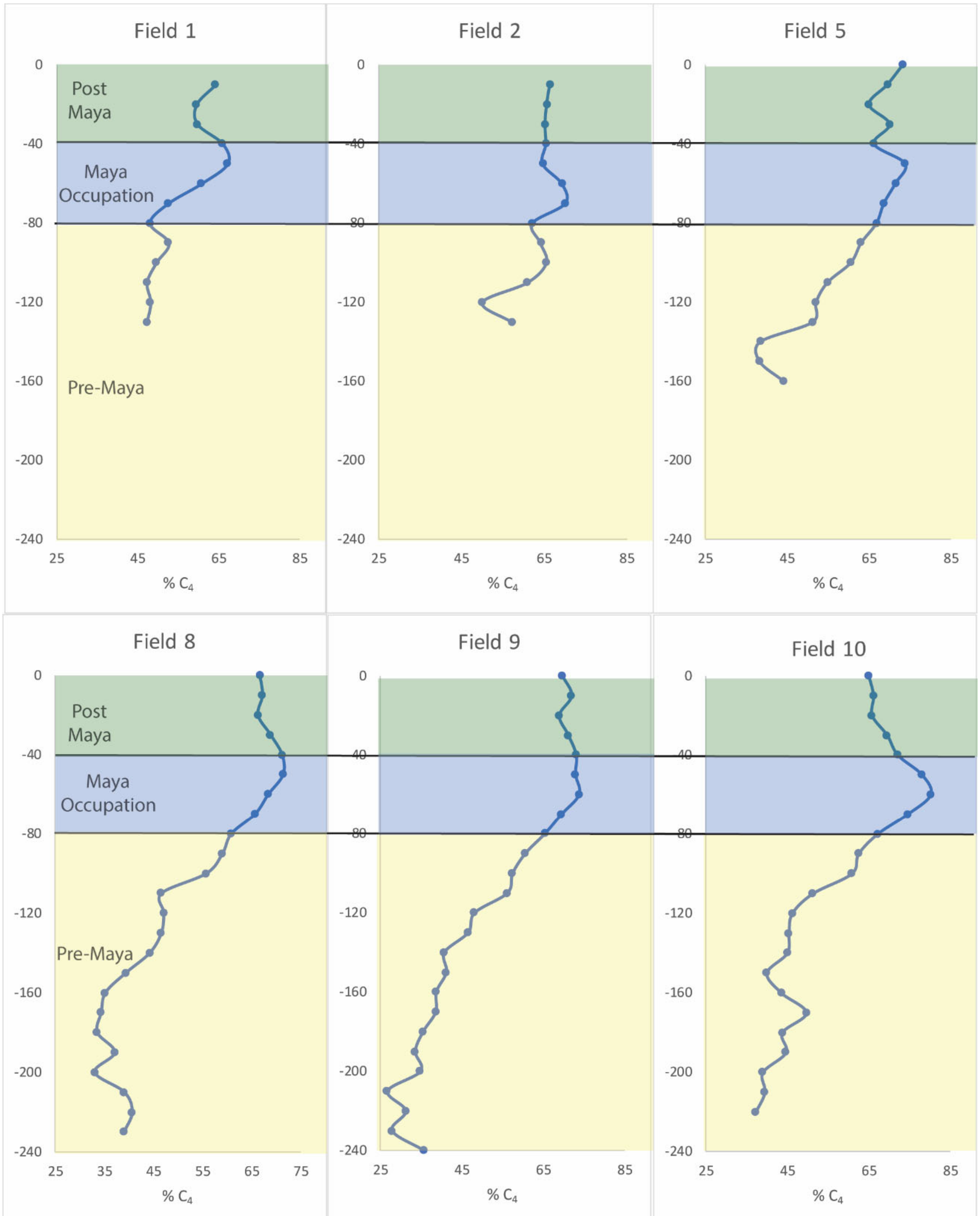

Figure 9: The modeled abundance of C_4 plants in the field soil profiles.

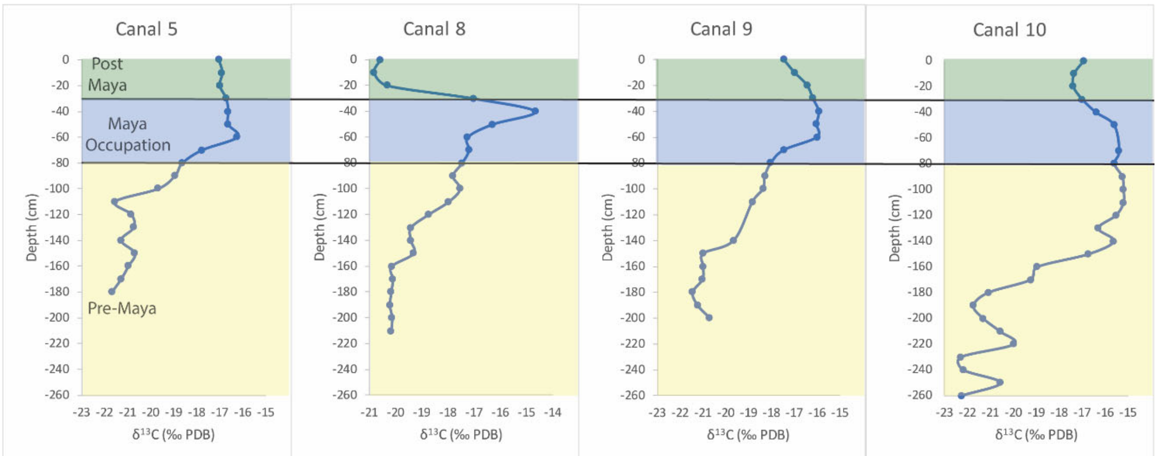

Figure 10: The $\delta^{13}C$ values with depth in the canal soil profiles.

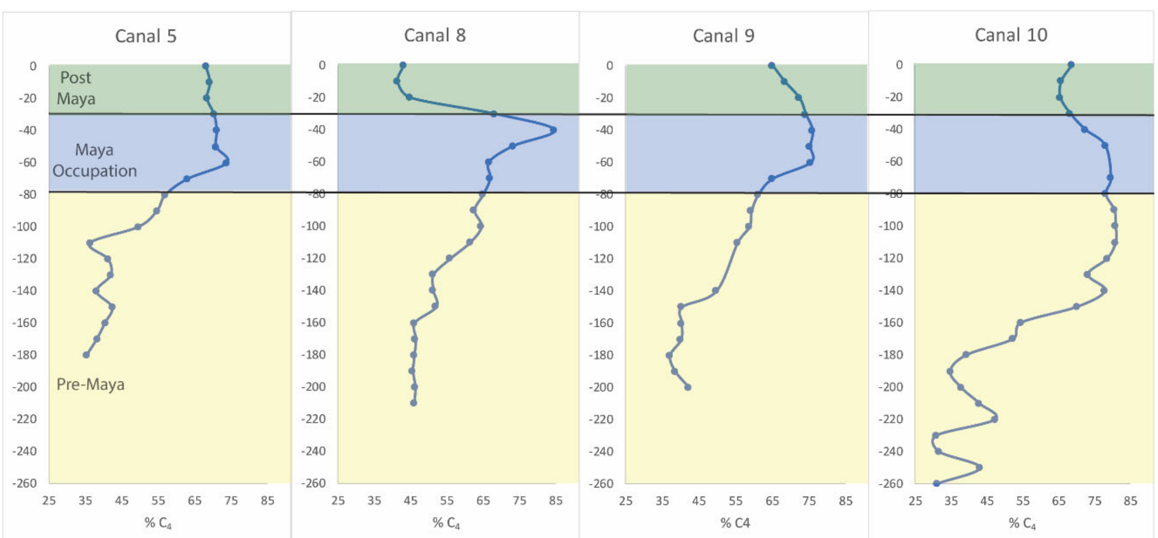

Figure 11: The abundance of C_4 plants within the canal soil profiles with depth.

Nitrogen Isotope Results

The trends in the isotopic composition of nitrogen within the field (Figure 12) and canal profiles (Figure 13) were not as pronounced as the $\delta^{13}C$ values. Throughout the pre-Maya period the $\delta^{15}N$ values fluctuate with an average of 7.6‰ AIR, and increase overall. In the Maya occupation period the $\delta^{15}N$ values fluctuate with an average of 8.2‰, but decrease overall into the post-Maya period. In the post-Maya period the $\delta^{15}N$ values continue to decrease with an average of 7‰. There are multiple biogeochemical processes that affect the abundance of ^{15}N in plant-soil systems (Szpak, 2014). During the decomposition of organic matter and the development of SOM soil micro-organisms cause denitrification, which is promoted when soils are wet (Clercq, et al., 2015). Fractionation of nitrogen during these processes bring about the loss of the lighter ^{14}N isotope from the SOM, causing an increase in the ^{15}N within the soil, this was not observed in the canal or field profiles (Clercq et al., 2015). The decrease in the $\delta^{15}N$ values near the end of the occupation period into the post-Maya period correlate with decreased agricultural activity and precipitation.

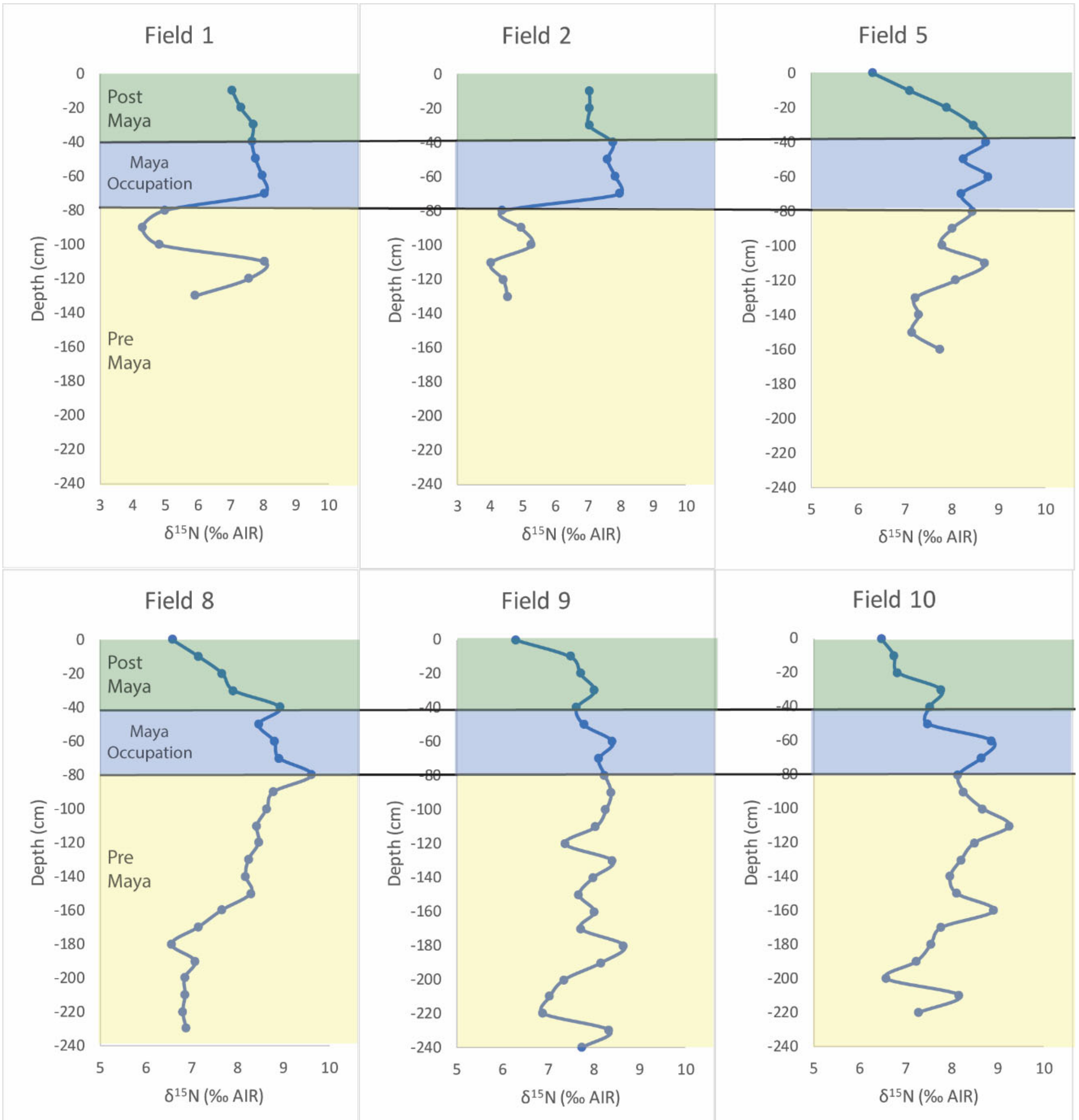

Figure 12: The $\delta^{15}N$ values with depth in the field profiles.

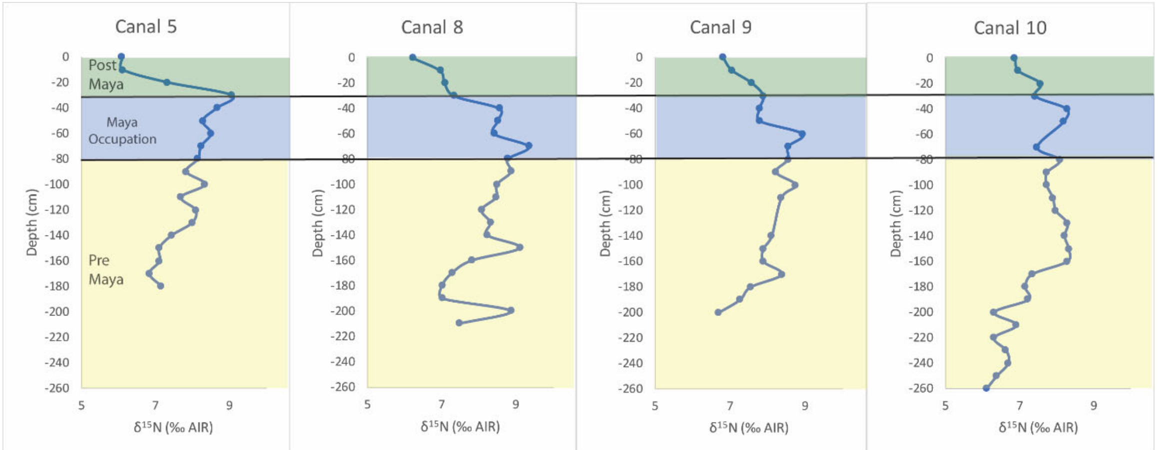

Figure 13: The $\delta^{15}N$ values with depth in the canal profiles.

Element Concentrations

The concentration of elements within the field and canal profiles displayed similar trends. Sodium fluctuated between 0.25-0.45 wt % with depth. At the base of the profile within the pre-Maya period, magnesium (MgO), aluminum (Al_2O_3), potassium (K_2O), and iron (Fe2O3) were present in higher concentrations followed by a decline with depth into the A horizon/post-Maya period (Figure 14). Silica (SiO_2), titanium (TiO_2) and zirconium (Zr) were present in lower concentrations within the pre-Maya period, and increased with depth into the post-Maya period (Figure 14). Manganese concentrations varied throughout the profiles and does not show a significant trend. Calcium concentrations are lower in the pre-Maya soil horizons and increase in the occupation and post-Maya periods. The interval of increased calcium may be due to decreased weathering intensity during the drought at the end of the occupation period, whereas the increase within the pre-Maya period, might be related to an increase in MAP. Phosphorus (P_2O_5) was present in higher concentrations within the pre-Maya period, lower concentrations in the occupation period, and higher concentrations in the post-Maya period. The decrease in phosphorus (P_2O_5) within the occupation period varies with increased $\delta^{13}C$ values, which indicates that the decrease in P might be the result of an increase in C_4 vegetation. In general, phosphorus availability is highest at the surface and decreases significantly in the subsoil horizons (Zhu et al., 2005). Because there are higher concentrations of P_2O_5 within the pre-Maya and post-Maya periods, and because of the high nutrient requirements of maize, this variation likely indicates that maize was the leading cause of the phosphorus reduction and carbon isotopic change in the occupation period.

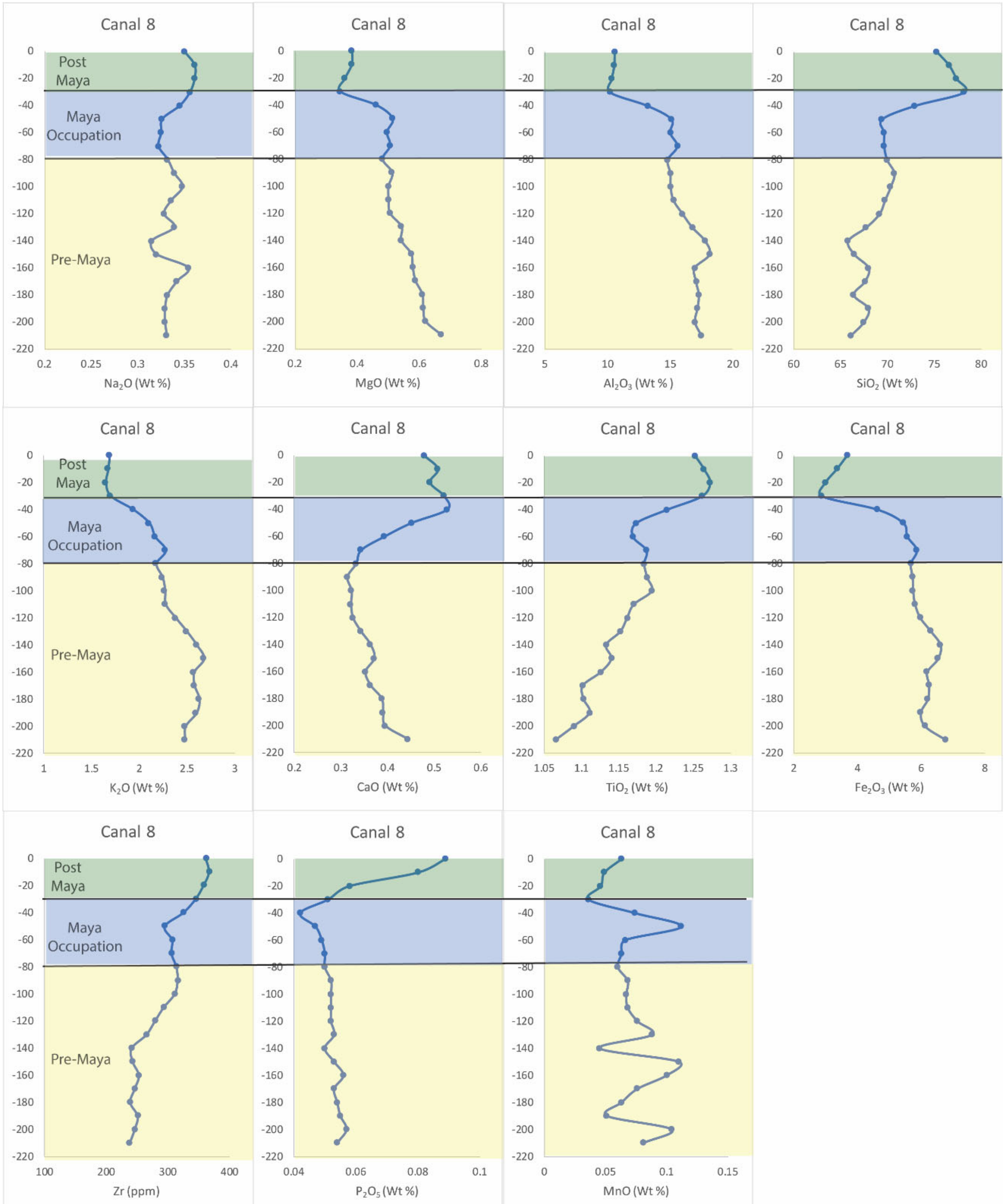

Figure 14: The concentration of major and minor elements within the Field site 8 profile, representative of all profiles.

Hydrolysis. The canal and field profiles display similar hydrolysis results. Higher ratios in hydrolysis indicate higher weathering intensities. Hydrolysis was high within the pre-Maya period and increased to the Maya occupation layer (Figure 15-16). Within the occupation period, hydrolysis decreases indicating a decrease in weathering intensity. The decrease in weathering intensities as the occupation period approaches the post-Maya period is likely due to droughts between 820-870 CE (Kennett et al., 2012). Higher ratios were expected due to the high concentration of clays within the B horizons.

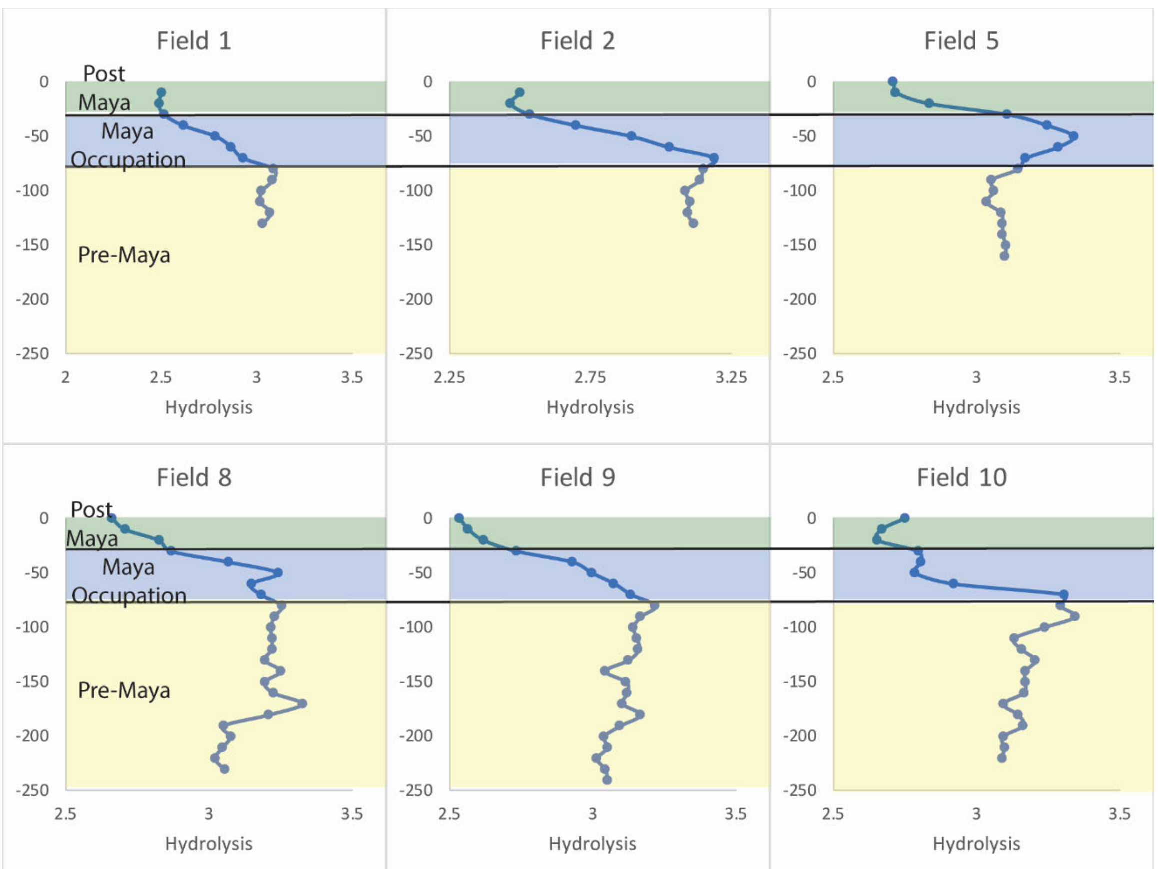

Figure 15: Field hydrolysis results with depth (cm).

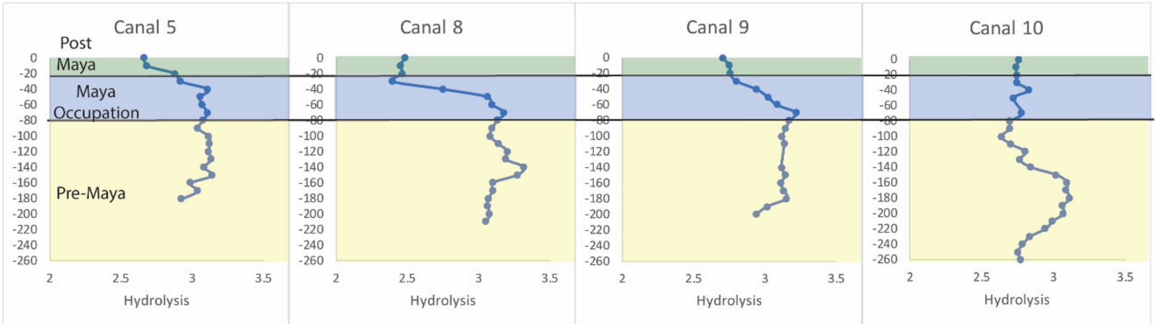

Figure 16: Canal hydrolysis results with depth (cm).

Mean Annual Precipitation (MAP)

CIA-K

The CIA-K pedotransfer function estimates a range of MAP values between 1347-1480 mm/yr in the field profiles, and 1356-1477 mm/yr in the canal profiles. This range is lower than the average modern precipitation in the area and does not display evidence of any of the droughts over the last few thousand years. Therefore, CIA-K values were used, instead, as a verification of soil type. The CIA-K values were greater than 80, with an average of 95.5 in the field and canal profiles indicating the soils experienced intense weathering and confirms their designation as Ultisols.

PPM 1.0

Using the PPM1.0 model to estimate MAP reveals that several of the soil profiles show changes over time. The soil profiles at field sites 5-10 have MAP estimates within the range of 1500-1750 mm/yr (Figure 17), and the canal profiles range between 1250-2000 mm/yr (Figure 18). Field site 1 and field site 2 show a significant decrease in MAP at the end of the Maya occupation period. This contrasts with the other field profiles which show little to no change in MAP (Figure 17). Soil profiles in canal 8, 9, and 10 also show a decrease in MAP (Figure 18) although the decline is less than that indicated by the field soil profiles.

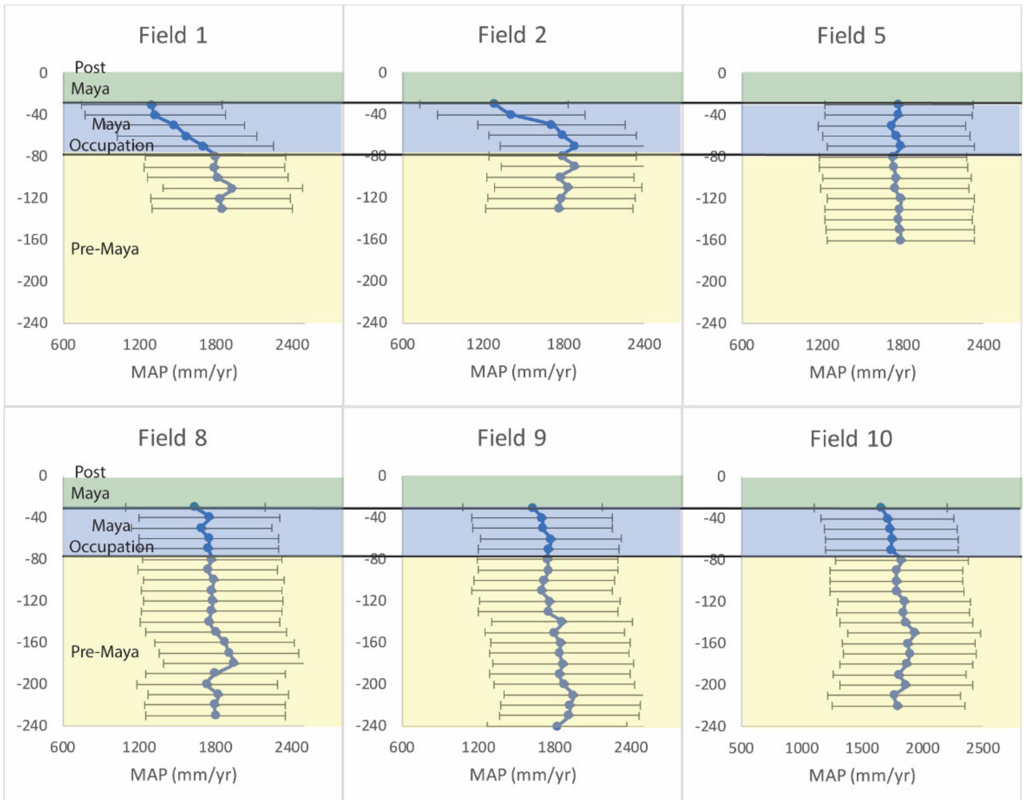

Figure 17: MAP estimates with depth based on the PPM1.0 model for the field profiles.

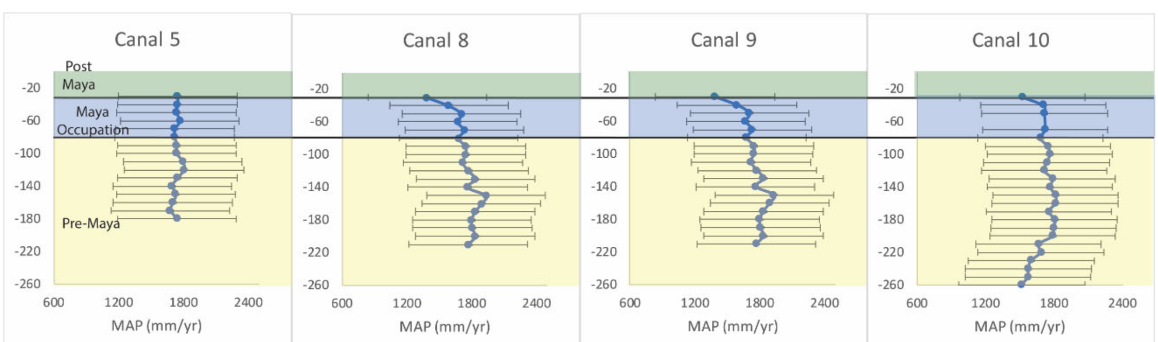

Figure 18: MAP estimates with depth based on the PPM1.0 model for the canal profiles.

CHAPTER FIVE

Conclusion

Based on the geochemistry of the Maya soil profiles three distinct time periods were identified: pre-Maya, Maya occupation, and post-Maya. Before the ancient Maya began cultivation of *Zea mays*, the average $\delta^{13}C$ of soil organic matter was -20.2‰ in the field sites and -19.6‰ within the canal soil profiles. This equates to a modeled C_4 vegetation abundance of between 46 to 50%. It therefore appears that the study area was originally a grassland, occupied by a mixed plant community including subequal amounts of C_3 and C_4 vegetation. A positive carbon isotope excursion in the pre-Maya soil horizons indicates that C_4 vegetation began to become more abundant in response to a changing climate.

During the occupation period, preserved organic matter has the highest $\delta^{13}C$ values and the soils are depleted in phosphorus. This geochemical signature occurs in soil horizons that contain ceramics, charcoal, and flint. Modeled plant communities during this time were composed of 73 to 78% C_4 plants indicating that *Zea mays* was cultivated by the ancient Maya in the ditched field system near Baking Pot, Belize. At the end of the occupation period, soil weathering intensity decreased indicating a decline in precipitation that was likely associated with the drought between 820-870 CE.

The post-Maya period is characterized by a decrease in the $\delta^{13}C$ values of soil organic matter. The soil profile in the canal 8 site has the best preservation of this trend and reveals a return to pre-Maya carbon isotope values. This return to more negative

$\delta^{13}C$ values is associated with a decrease in estimates of MAP, along with a decrease in weathering intensity (hydrolysis) and is indicative of the return of higher proportions of C_3 plants in the absence of Maya agriculture.

Future work to further understand the processes that influenced the ditched field system include micromorphological study using thin-sections, a well constrained age model, pollen analysis, X-ray diffraction, analysis of clay minerals, and soil particle-size analysis to further understand the depositional setting of the profiles.

APPENDICES

APPENDIX A

Comparison Graphs

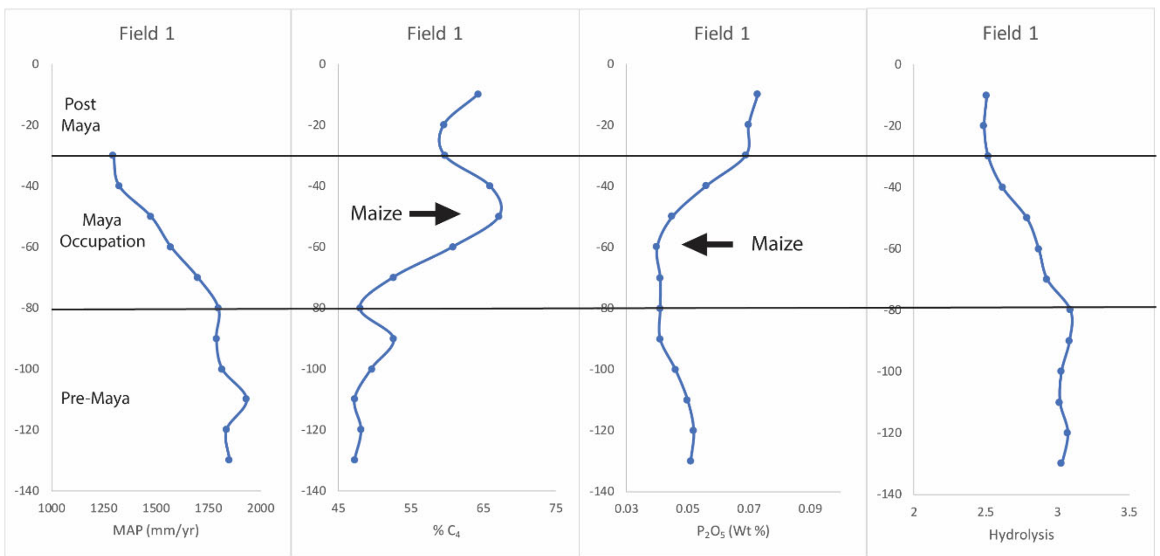

Figure A.1: The comparison of MAP, percentage of C_4, phosphorus, and hydrolysis at field site 1.

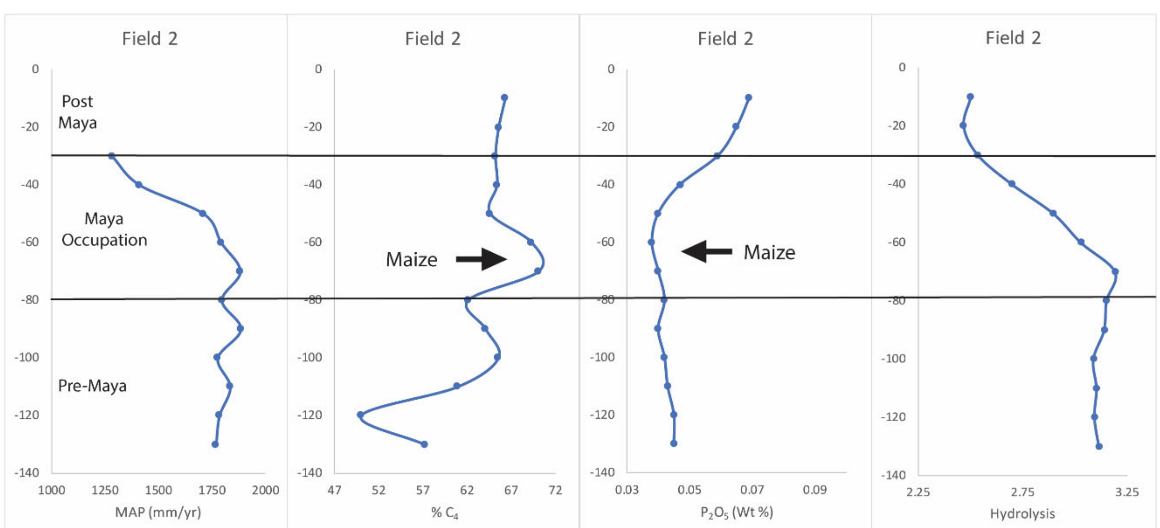

Figure A.2: The comparison of MAP, percentage of C_4, phosphorus, and hydrolysis at field site 2.

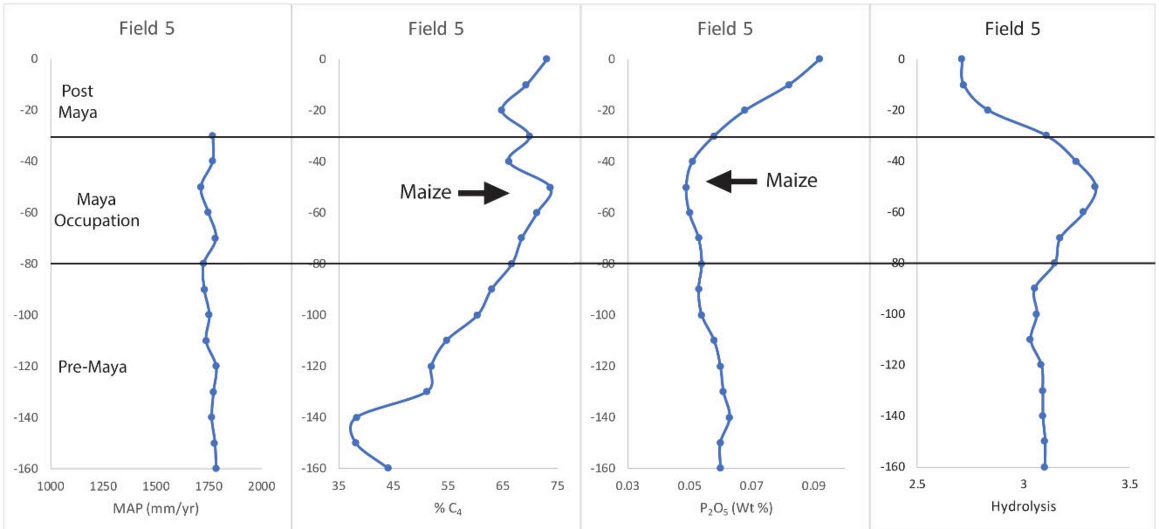

Figure A.3: The comparison of MAP, percentage of C_4, phosphorus, and hydrolysis at field site 5.

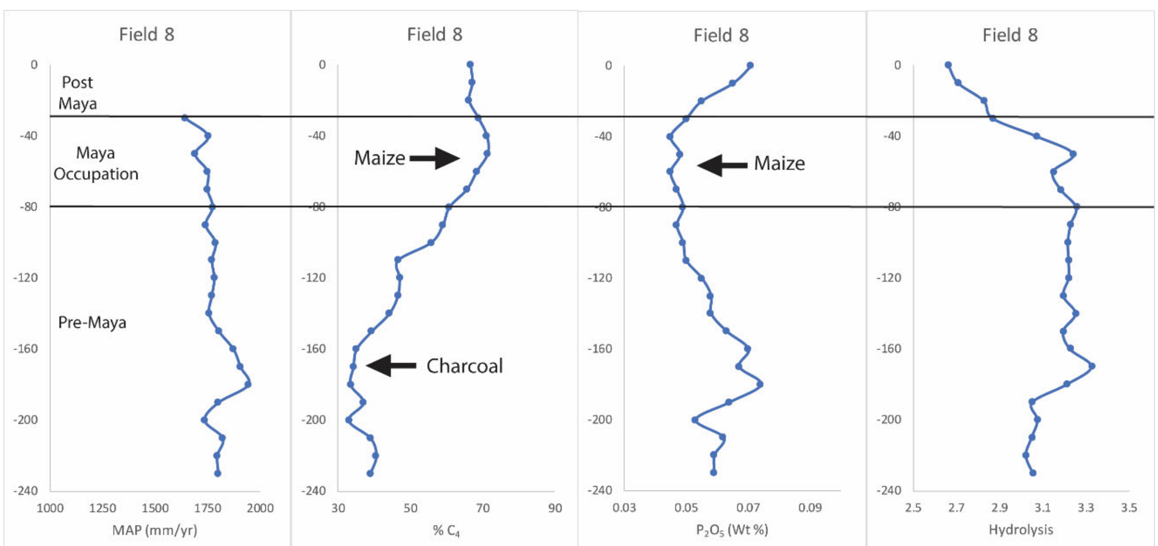

Figure A.4: The comparison of MAP, percentage of C_4, phosphorus, and hydrolysis at field site 8.

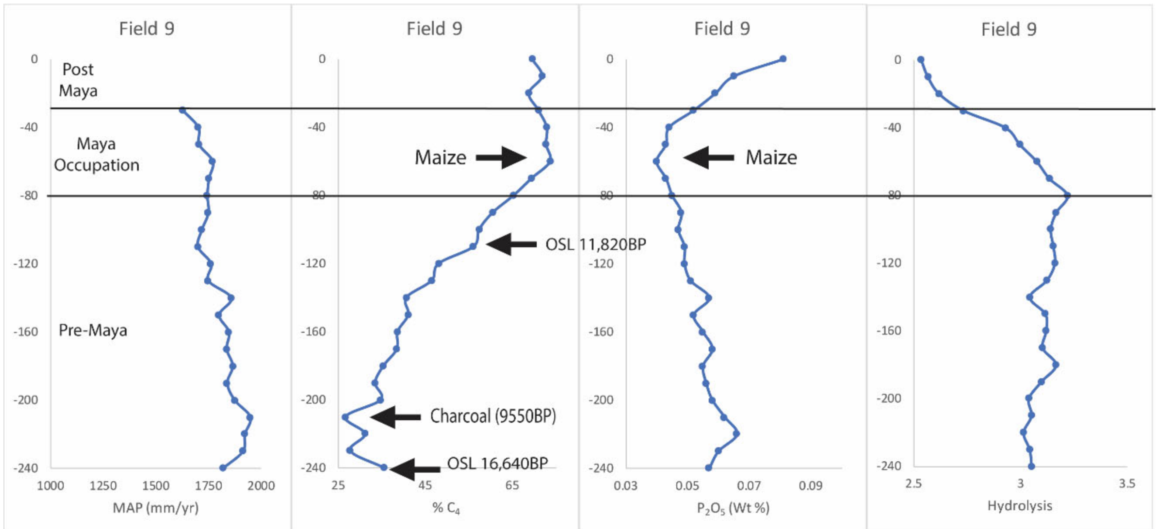

Figure A.5: The comparison of MAP, percentage of C_4, phosphorus, and hydrolysis at field site 9.

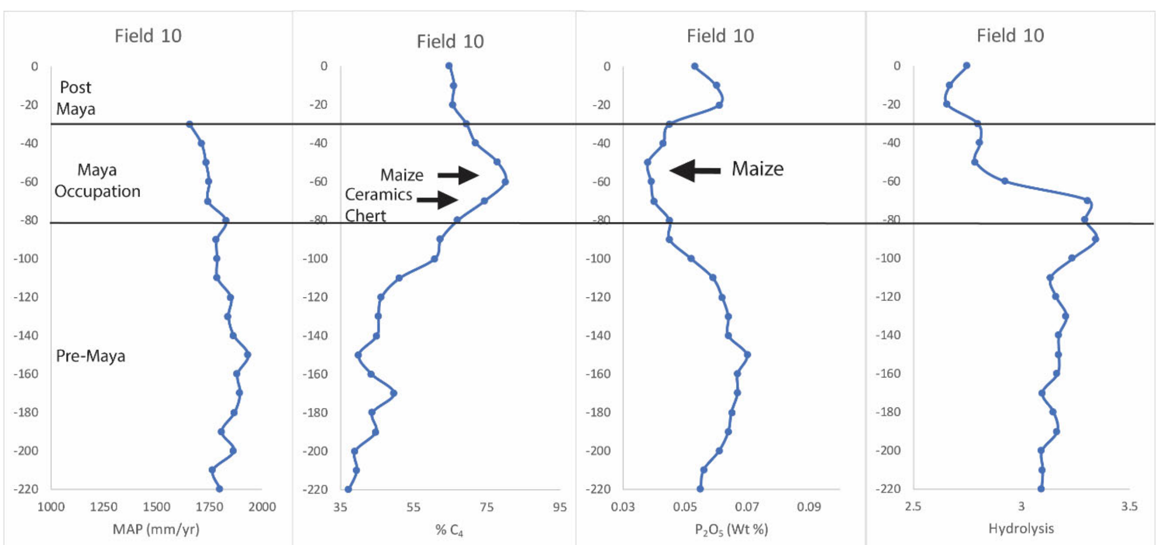

Figure A.6: The comparison of MAP, percentage of C_4, phosphorus, and hydrolysis at field site 10.

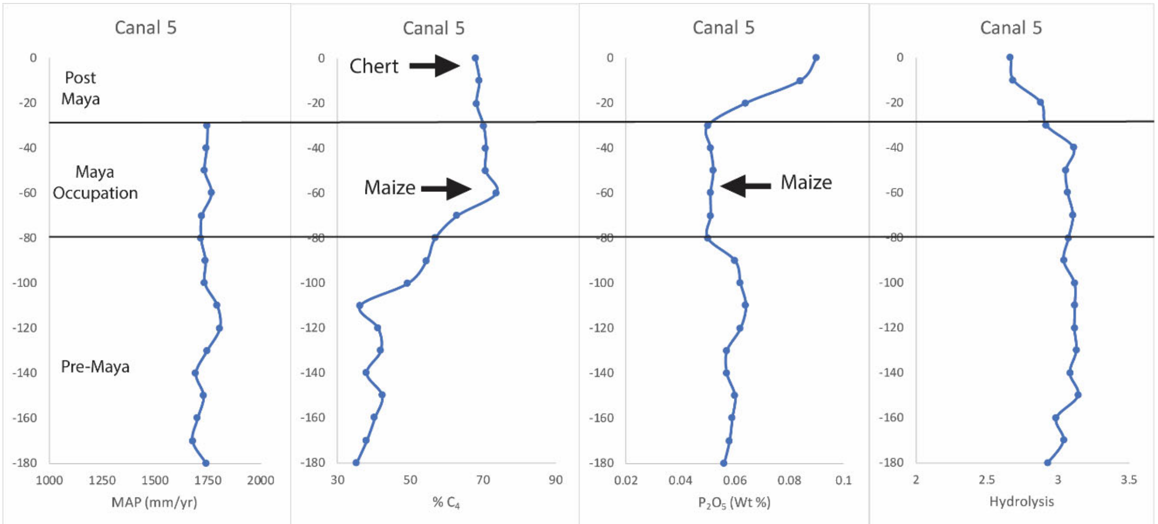

Figure A.7: The comparison of MAP, percentage of C_4, phosphorus, and hydrolysis within canal site 5.

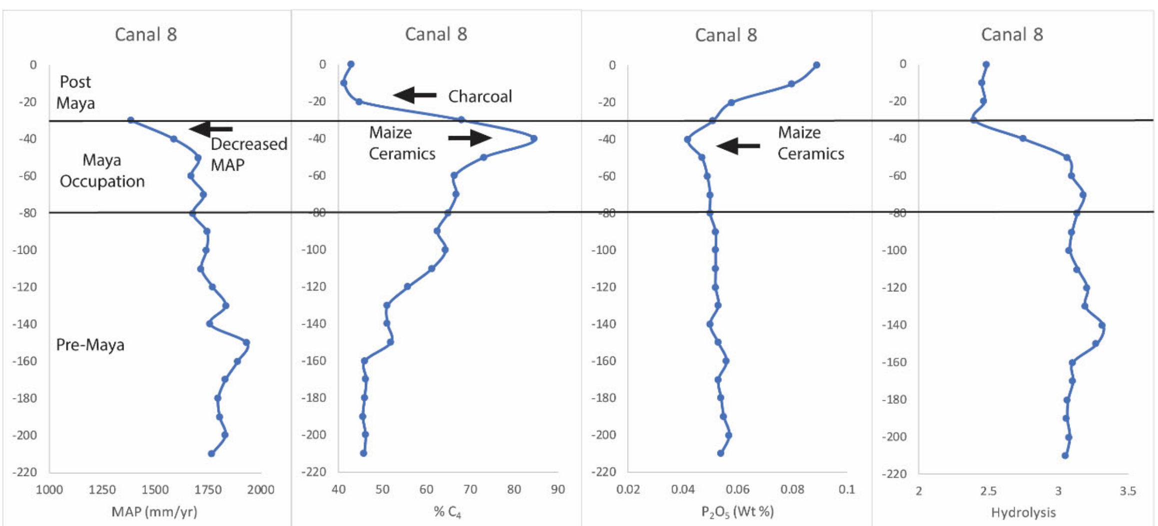

Figure A.8: The comparison of MAP, percentage of C_4, phosphorus, and hydrolysis within canal site 8.

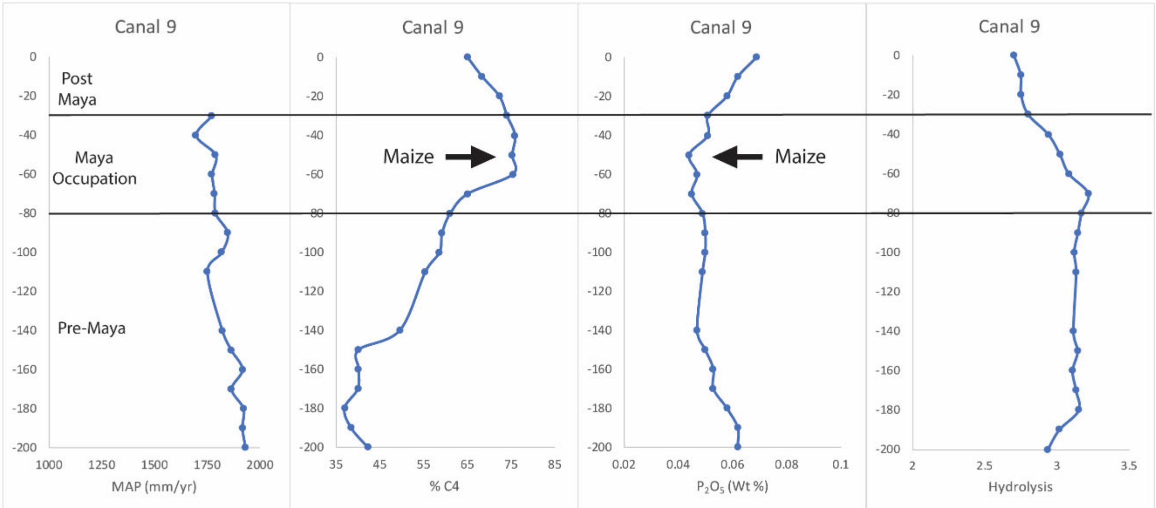

Figure A.9: Figure A.7: The comparison of MAP, percentage of C_4, phosphorus, and hydrolysis within canal site 9.

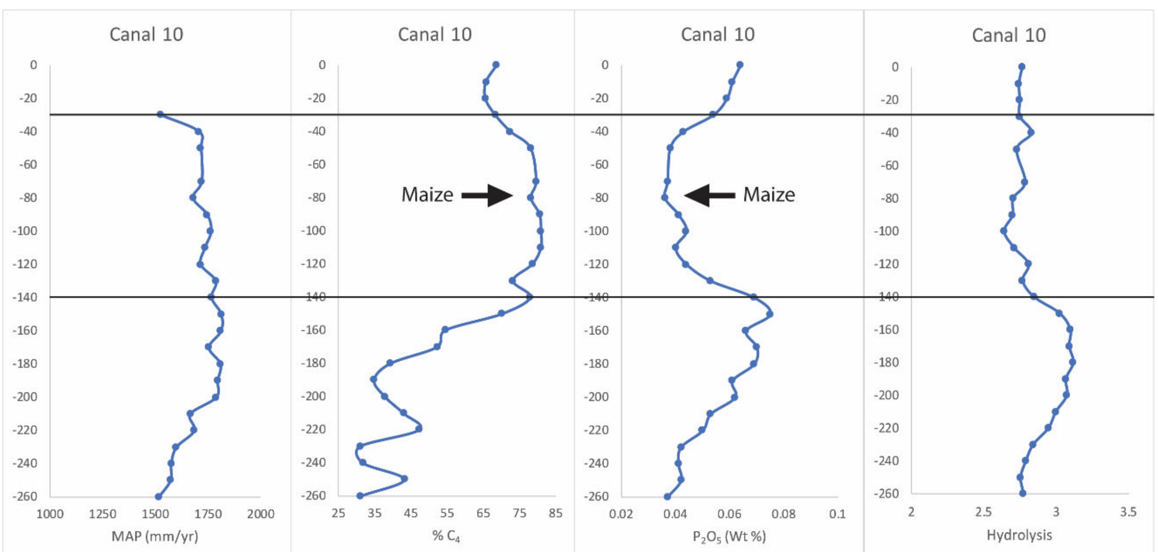

Figure A.10: Figure A.7: The comparison of MAP, percentage of C_4, phosphorus, and hydrolysis within canal site 10.

APPENDIX B

Soil Profile Descriptions

Table B.1

Canal 5 Profile Description

Depth	Horizon	Munsell Color	Grain Size	Soil Features
0-30	A	10YR 6/3-5/3	Silt, Clay	Crumby peds, roots, chert flake
30-50	B1	10YR 5/4	Clay	Mottled, manganese or iron nodules, redox features
50-90	B2	10YR 5/6	Clay	Clay rich
90-150	B3	10YR 6/6	Clay	Clay rich
150-180	B4	10YR 6/6	Clay	Loamy, wetter than overlying layer

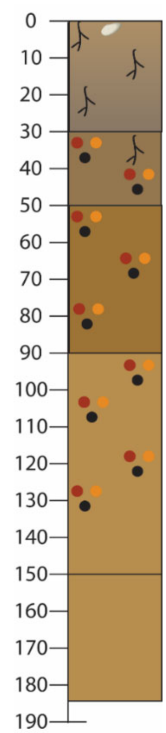

Figure B.1: The profile of Canal Site 5.

Figure B.2: A photo of Canal Site 5 in the field.

Table B.2

Field 5 Profile Description

Depth	Horizon	Munsell Color	Grain Size	Soil Features
0-30	A	10YR 5/3	Silt Clay	Crumby Peds
30-50	B1	10YR 6/4	Clay	Transition layer for colors, clay rich
50-70	B2	10YR 5/6	Clay	
70-140	B3	10YR 5/6	Clay	Redox features, manganese or iron nodules
140-160	B4	10YR 5/6	Clay	

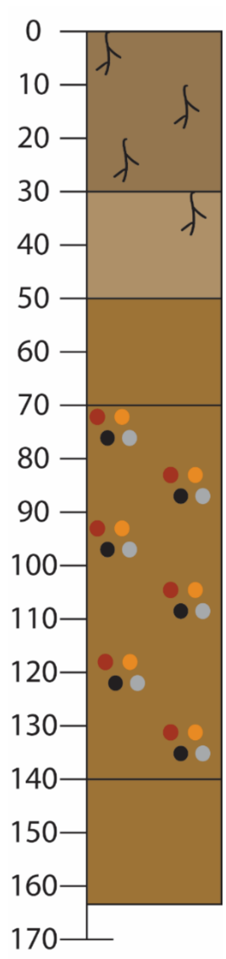

Figure B.3: The profile of field 5.

Table B.3

Canal 8 Profile Description

Depth	Horizon	Munsell Color	Grain Size	Soil Features
0-30	A	10YR 2/1	Silt Clay	Crumby peds, roots, charcoal at 20 cm
30-50	B1	10YR 3/2-3/3	Clay	Transition layer for color, ceramics between 40-50cm, iron or manganese nodules
50-120	B2	10YR 4/6	Clay	Manganese or iron nodules
120-170	B4	10YR 5/6	Clay	Clay rich
170-210	B5	10YR 5/6	Clay	Slightly lighter yellow

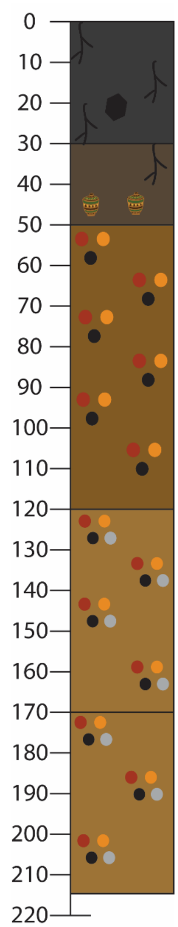

Figure B.4: The profile of Canal Site 8.

Figure B.5: A photo of Canal Site 8.

Table B.4

Field 8 Profile Description

Depth	Horizon	Munsell Color	Grain Size	Soil Features
0-30	A	10YR 3/3	Silt Clay	Crumby Peds, roots, clay rich
30-60	B1	10YR ¾	Silt Clay	Crumby peds, roots
60-110	B2	7.5YR 4/4	Clay	Iron manganese nodules, some gray clay present,
110-150	B3	10YR 5/6	Clay	Iron manganese nodules
150-230	B4	10YR 6/4	Clay	Iron manganese nodules, charcoal at 170 cm, at 170 and 210 slighty darker orange (10YR 5/4),

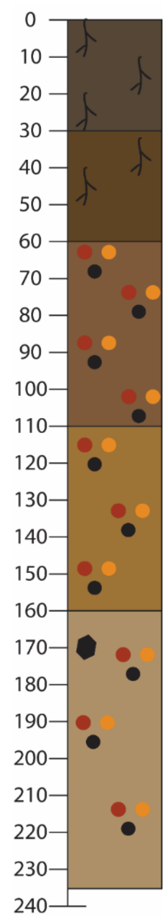

Figure B.6: The profile of Field Site 8.

Figure B.7: A photo of Field Site 8.

Table B.5

Canal 9 Profile Description

Depth	Horizon	Munsell Color	Grain Size	Soil Features
0-20	A	10YR 3/2	Silt Clay	Crumby peds, clay rich, roots present
20-40	B1	10YR 4/3	Clay	Crumby peds, roots
40-60	B2	10YR ¾	Clay	Gray clay nodules, orange nodules
60-100	B3	10YR 4/6	Clay	Gray clay nodules, orange nodules
100-190	B4	10YR 5/6	Clay	Gray clay nodules, orange nodules, iron manganese nodules below 130cm
190-200	B5	10YR 5/4	Clay	Iron manganese nodules

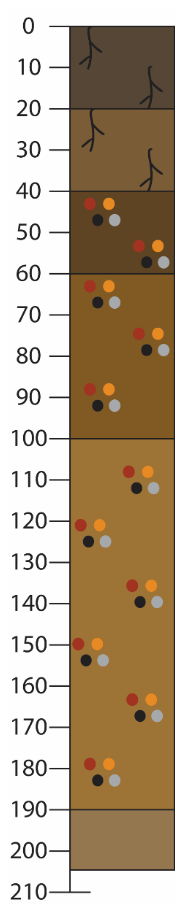

Figure B.8: The profile of Canal Site 9.

Figure B.9: A photo of Canal Site 9.

Table B.6

Field 9 Profile Description

Depth	Horizon	Munsell Color	Grain Size	Soil Features
0-30	A	10YR 3/2	Silt clay	Crumby peds, roots
30-50	B1	10YR 4/2	Clay	Crumby peds, roots
50-70	B2	10YR 4/4	Clay	Gray clay nodules, iron manganese nodules, orange nodules
70-90	B3	10YR 4/6	Clay	Gray clay nodules, iron manganese nodules, orange nodules
90-200	B4	10YR 5/6	Clay	Clay columns and nodules present
200-210	B5	10YR 5/4	Clay	
210-240	B6	10YR 4/6	clay	Charcoal and chert at 210cm

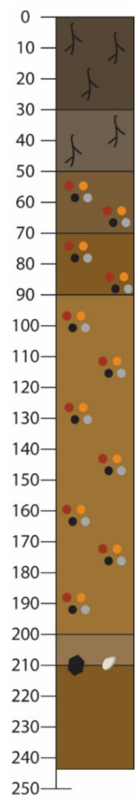

Figure B.10: The profile of Field Site 9.

Figure B.11: A photo of Field Site 9.

Table B.7

Canal 10 Profile Description

Depth	Horizon	Munsell Color	Grain Size	Soil Features
0-30	A	10YR 4/2	Silt Clay	Crumby peds, roots
30-90	B1	10YR 4/2	Clay	Clay rich
90-140	B2	10YR 4/2	Clay	Gray clay nodules, orange nodules
140-260	B3	10YR 5/4	Clay	Wet and soft, clay nodules

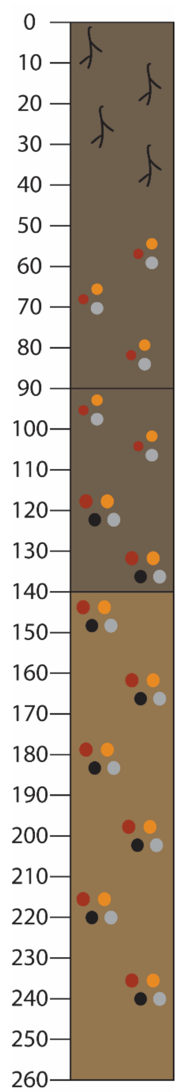

Figure B.12: The profile of Canal Site 10.

Figure B.13: A photo of Canal Site 10.

Table B.8

Field 10 Profile Description

Depth	Horizon	Munsell Color	Grain Size	Soil Features
0-40	A	10YR 3/2	Silt Clay	Roots present
40-60	B1	10YR 4/3	Clay	Roots present
60-80	B2	10YR 5/4	Clay	Clay nodules, iron manganese nodules, Ceramics and chert at 70 cm
80-100	B3	10YR 4/6	Clay	Clay nodules, iron manganese nodules,
100-160	B4	10YR 5/6	Clay	Iron manganese nodules
160-220	B5	10YR 5/8	Clay	Larger clay nodules present

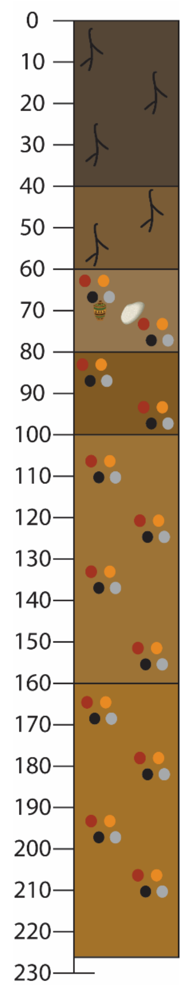

Figure B.14: The profile of Field Site 10.

APPENDIX C

Elemental Concentrations

Table C.1

NaO within the field profiles (wt. %)

Depth	Field 1	Field 2	Field 5	Field 8	Field 9	Field 10
0	-	-	0.373	0.347	0.351	0.401
-10	0.282	0.282	0.397	0.359	0.364	0.369
-20	0.347	0.347	0.453	0.361	0.375	0.384
-30	0.292	0.292	0.412	0.373	0.377	0.395
-40	0.306	0.306	0.332	0.357	0.379	0.398
-50	0.31	0.31	0.335	0.341	0.366	0.412
-60	0.34	0.34	0.342	0.344	0.355	0.396
-70	0.337	0.337	0.356	0.334	0.353	0.344
-80	0.344	0.344	0.336	0.318	0.338	0.336
-90	0.33	0.33	0.367	0.328	0.35	0.329
-100	0.345	0.345	0.351	0.346	0.361	0.343
-110	0.34	0.34	0.368	0.342	0.35	0.351
-120	0.339	0.339	0.357	0.347	0.345	0.353
-130	0.369	0.369	0.357	0.351	0.348	0.339
-140	-	-	0.358	0.318	0.396	0.344
-150	-	-	0.36	0.353	0.358	0.344
-160	-	-	0.347	0.325	0.367	0.356
-170	-	-	-	0.306	0.368	0.43
-180	-	-	-	0.343	0.356	0.356
-190	-	-	-	0.364	0.344	0.345
-200	-	-	-	0.334	0.38	0.363
-210	-	-	-	0.329	0.351	0.328
-220	-	-	-	0.343	0.377	0.334
-230	-	-	-	0.337	0.32	-
-240	-	-	-	-	0.323	-

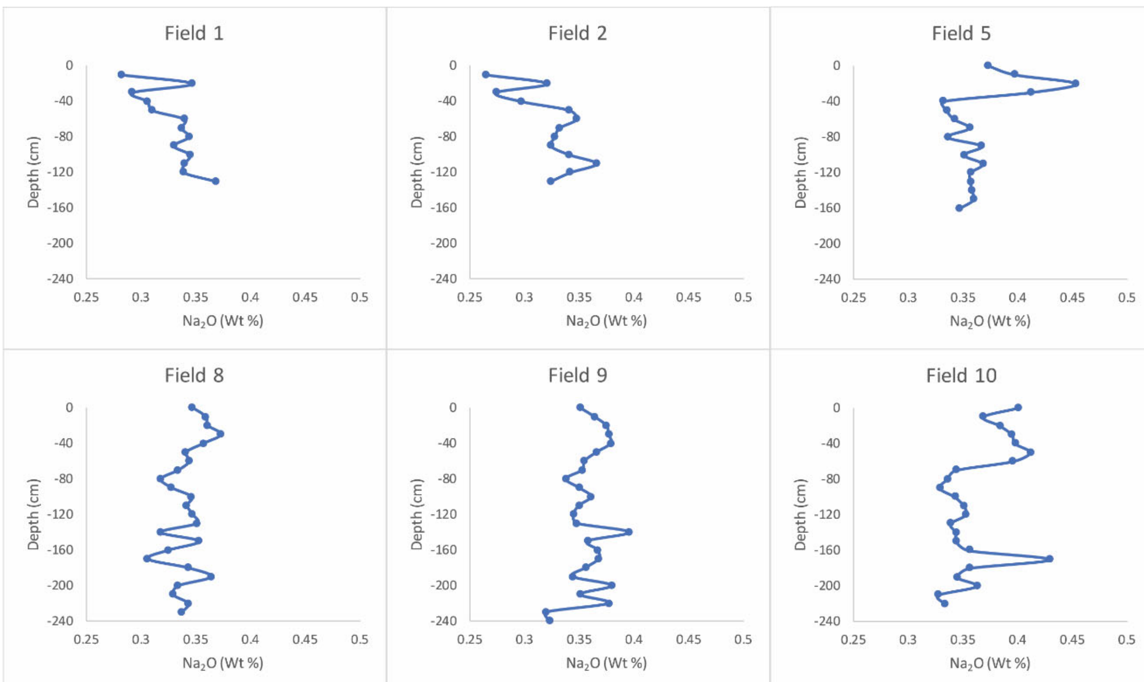

Figure C.1: The weight percent of Na_2O with depth in centimeters from the surface.

Table C.2

MgO within the field profiles (Wt. %)

Depth	Field 1	Field 2	Field 5	Field 8	Field 9	Field 10
0	-	-	0.366	0.39	0.391	0.344
-10	0.624	0.707	0.353	0.382	0.401	0.324
-20	0.605	0.696	0.381	0.395	0.393	0.326
-30	0.633	0.689	0.426	0.436	0.42	0.353
-40	0.614	0.662	0.456	0.461	0.473	0.372
-50	0.564	0.555	0.454	0.466	0.474	0.399
-60	0.522	0.536	0.466	0.462	0.483	0.456
-70	0.522	0.508	0.467	0.475	0.481	0.477
-80	0.496	0.513	0.461	0.451	0.473	0.469
-90	0.493	0.523	0.465	0.44	0.463	0.479
-100	0.494	0.523	0.478	0.452	0.463	0.491
-110	0.494	0.532	0.51	0.455	0.445	0.494
-120	0.494	0.539	0.53	0.465	0.481	0.522
-130	0.519	0.543	0.545	0.477	0.484	0.556
-140	-	-	0.553	0.497	0.521	0.572
-150	-	-	0.548	0.505	0.542	0.596
-160	-	-	0.547	0.556	0.574	0.571
-170	-	-	-	0.601	0.603	0.573
-180	-	-	-	0.617	0.651	0.574
-190	-	-	-	0.593	0.645	0.573
-200	-	-	-	0.6	0.654	0.571
-210	-	-	-	0.618	0.658	0.598
-220	-	-	-	0.635	0.681	0.576
-230	-	-	-	0.648	0.701	-
-240	-	-	-	-	0.702	-

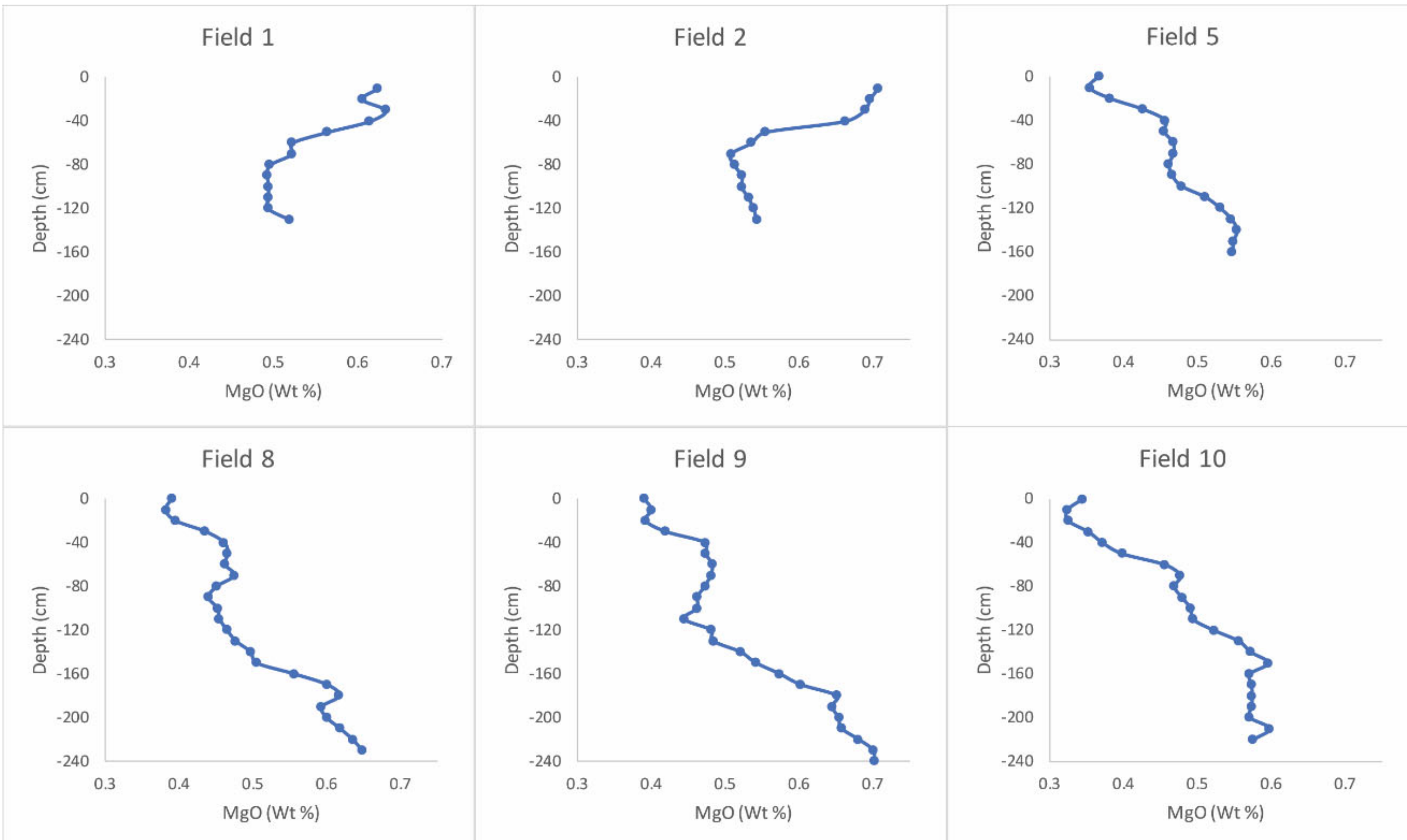

Figure C.2: The weight percent of MgO in the field profiles with depth in cm from the surface.

Table C.3

Al_2O_3 within the field profiles (Wt. %)

Depth	Field 1	Field 2	Field 5	Field 8	Field 9	Field 10
0	-	-	10.307	11.028	10.695	10.799
-10	13.967	14.746	10.579	11.261	11.049	9.768
-20	13.96	14.923	11.735	11.991	11.101	9.81
-30	14.133	14.862	13.909	12.925	12.107	11.228
-40	14.35	15.26	14.587	14.273	13.981	11.619
-50	14.347	14.783	14.92	15.046	14.217	12.114
-60	15.179	15.347	14.82	14.591	14.69	13.72
-70	15.548	15.916	14.243	14.919	14.893	15.425
-80	15.446	15.687	13.702	14.873	15.22	15.322
-90	15.497	15.79	13.471	14.585	14.839	15.559
-100	15.278	15.763	13.66	14.858	14.589	15.064
-110	15.259	16.229	14.007	14.831	14.397	14.539
-120	15.062	16.105	14.835	15.225	15.186	15.43
-130	15.73	16.399	15.176	15.36	14.955	16.694
-140	-	-	15.287	15.821	15.247	16.824
-150	-	-	15.468	15.916	15.879	17.189
-160	-	-	15.466	17.112	16.694	16.721
-170	-	-	-	18.684	17.075	16.914
-180	-	-	-	18.36	18.709	16.862
-190	-	-	-	16.654	17.711	16.658
-200	-	-	-	16.966	17.669	16.271
-210	-	-	-	17.214	17.82	16.491
-220	-	-	-	17.248	18.234	16.151
-230	-	-	-	17.221	18.372	-
-240	-	-	-	-	18.122	-

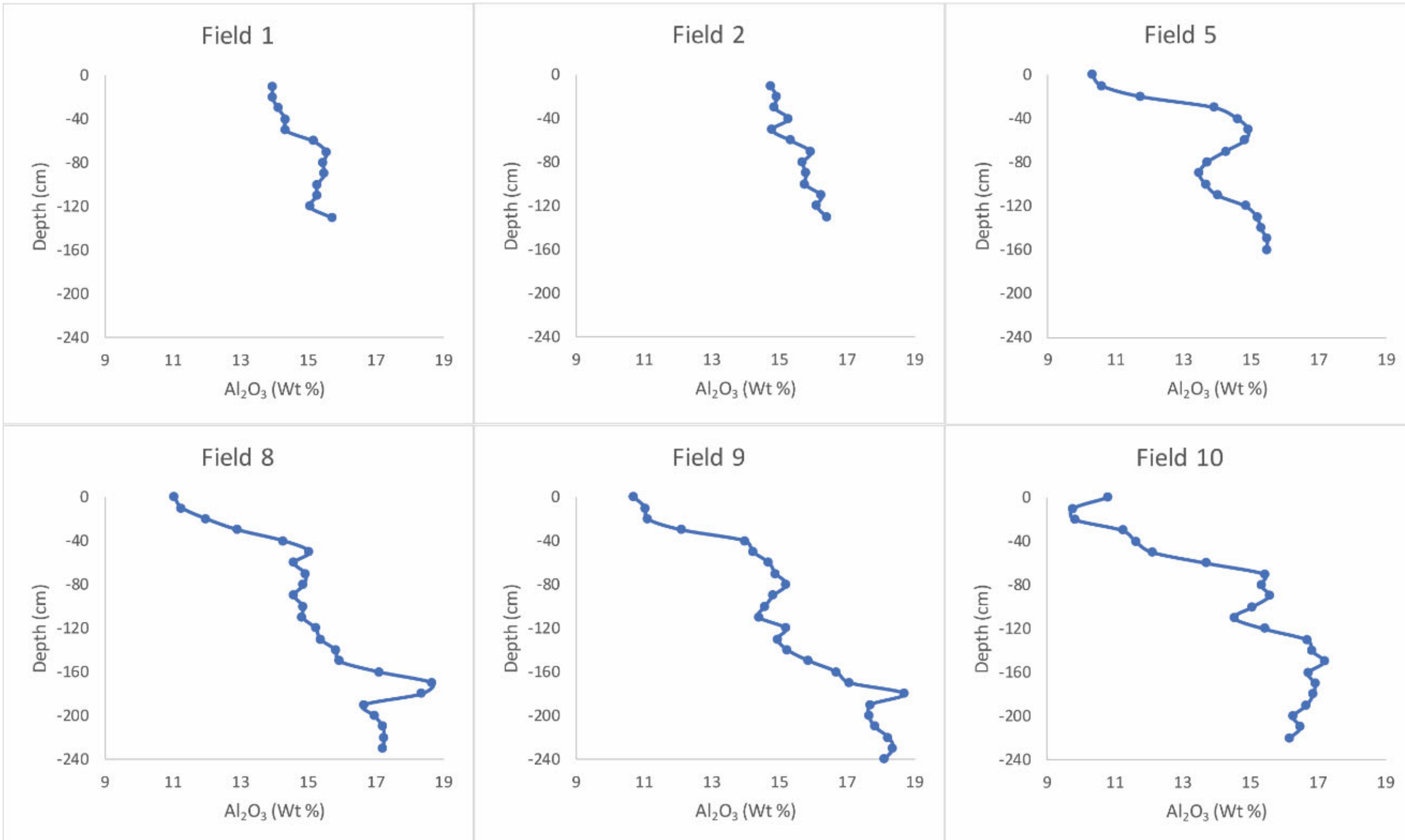

Figure C.3: The weight percent of Al_2O_3 with depth (cm) in the field profiles.

Table C.4

SiO_2 within the field profiles (Wt. %)

Depth	Field 1	Field 2	Field 5	Field 8	Field 9	Field 10
0	-	-	75.523	75.167	75.525	77.889
-10	64.545	63.429	75.559	75.016	75.44	78.648
-20	64.656	63.963	73.556	74.105	76.137	77.919
-30	64.842	63.578	71.413	72.011	74.417	76.87
-40	65.501	65.175	70.693	71.695	72.111	76.373
-50	66.697	66.28	69.761	69.737	71.751	75.678
-60	67.701	67.621	70.974	70.36	71.647	73.398
-70	66.869	67.42	72.13	70.709	71.042	70.042
-80	67.124	67.728	72.618	70.688	70.39	69.912
-90	67.828	68.226	73.078	70.539	70.737	70.622
-100	68.811	67.384	72.684	71.008	71.401	70.877
-110	67.948	68.397	72.138	70.905	70.485	71.927
-120	68.712	68.252	71.222	70.659	69.938	70.443
-130	69.09	67.367	70.35	69.886	70.424	67.502
-140	-	-	69.963	69.07	70.663	67.494
-150	-	-	69.663	68.822	69.587	67.966
-160	-	-	70.078	66.851	68.211	67.954
-170	-	-	-	64.664	68.273	67.61
-180	-	-	-	65.263	64.331	67.571
-190	-	-	-	68.404	66.627	68.224
-200	-	-	-	66.643	66.989	69.184
-210	-	-	-	66.31	66.899	68.502
-220	-	-	-	66.949	66.013	68.603
-230	-	-	-	66.897	65.296	-
-240	-	-	-	-	65.33	-

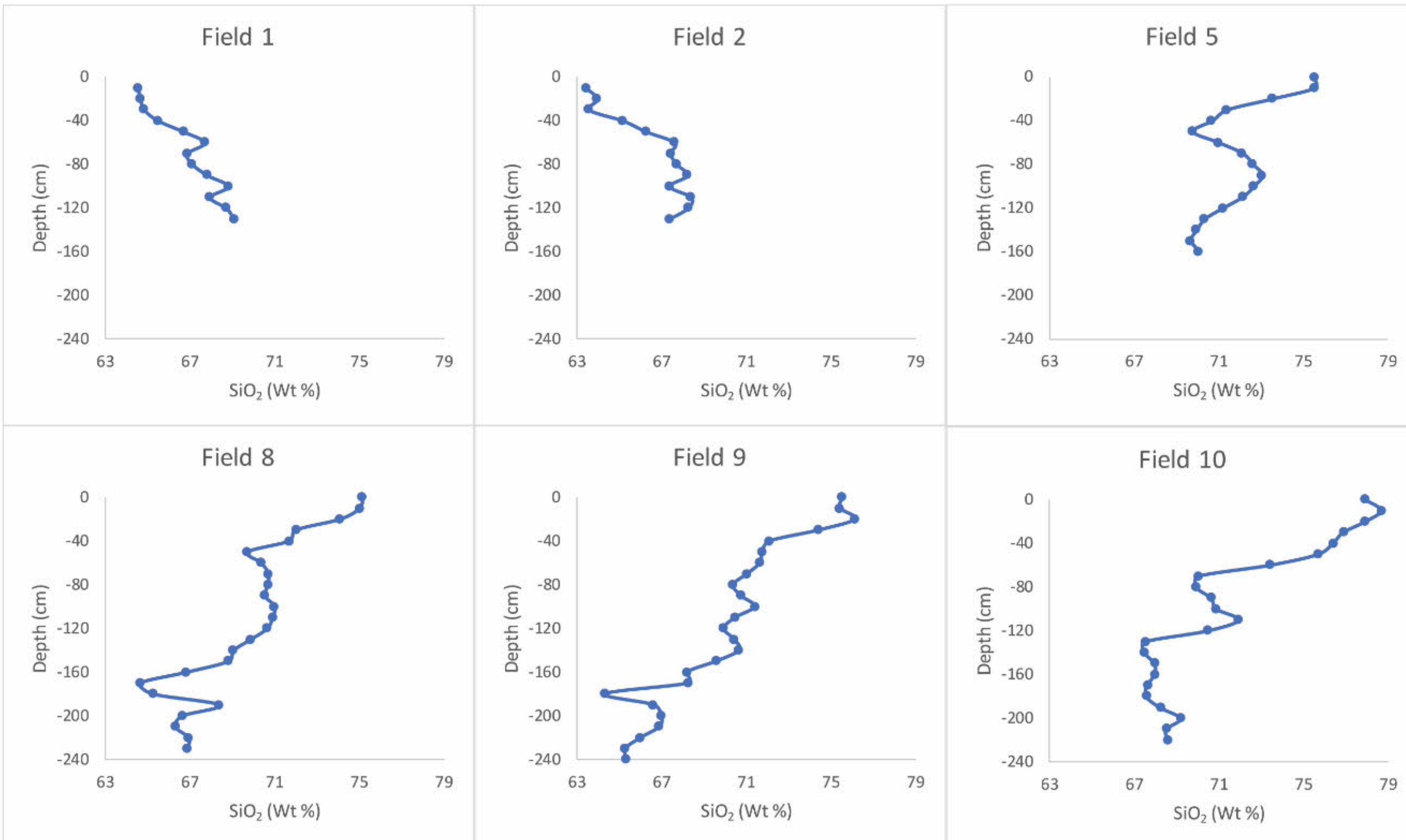

Figure C.4: The weight percent of silica with depth (cm) in the field profiles.

Table C.5

K_2O within the field profiles (Wt. %)

Depth	Field 1	Field 2	Field 5	Field 8	Field 9	Field 10
0	-	-	1.711	1.702	1.603	1.774
-10	1.583	1.623	1.744	1.732	1.591	1.582
-20	1.6	1.635	1.855	1.817	1.607	1.602
-30	1.623	1.648	2.148	1.989	1.799	1.831
-40	1.657	1.771	2.245	2.122	2.114	1.909
-50	1.746	2.021	2.231	2.149	2.119	2.015
-60	2.117	2.203	2.235	2.186	2.197	2.177
-70	2.171	2.276	2.196	2.223	2.217	2.232
-80	2.254	2.274	2.125	2.221	2.247	2.286
-90	2.277	2.299	2.132	2.191	2.224	2.274
-100	2.257	2.304	2.165	2.228	2.185	2.233
-110	2.307	2.361	2.197	2.234	2.181	2.214
-120	2.292	2.359	2.315	2.311	2.319	2.352
-130	2.356	2.441	2.372	2.349	2.298	2.548
-140	-	-	2.377	2.388	2.34	2.584
-150	-	-	2.392	2.414	2.396	2.633
-160	-	-	2.389	2.582	2.526	2.536
-170	-	-	-	2.743	2.575	2.573
-180	-	-	-	2.784	2.784	2.56
-190	-	-	-	2.555	2.661	2.482
-200	-	-	-	2.593	2.675	2.428
-210	-	-	-	2.657	2.727	2.405
-220	-	-	-	2.646	2.786	2.36
-230	-	-	-	2.557	2.785	-
-240	-	-	-	-	2.66	-

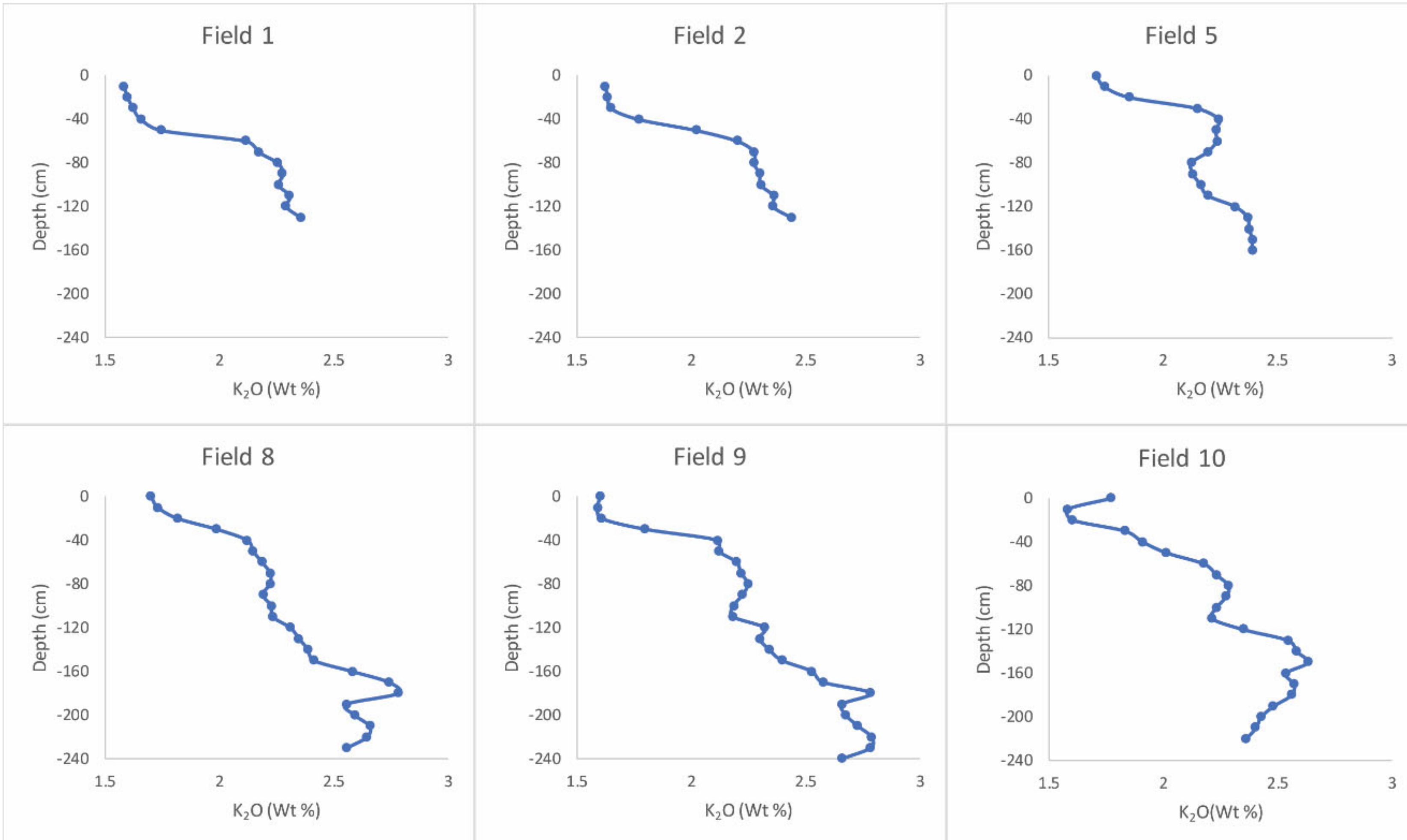

Figure C.5: The weight percent of K_2O with depth (cm) within the field profiles.

Table C.6

CaO within the field profiles

Depth	Field 1	Field 2	Field 5	Field 8	Field 9	Field 10
0	-	-	0.226	0.408	0.504	0.262
-10	0.999	1.051	0.251	0.4	0.533	0.286
-20	0.976	1.093	0.233	0.376	0.488	0.277
-30	0.976	1.035	0.217	0.35	0.439	0.269
-40	0.898	0.865	0.2	0.33	0.366	0.262
-50	0.727	0.523	0.195	0.317	0.357	0.263
-60	0.616	0.414	0.194	0.294	0.326	0.293
-70	0.596	0.38	0.19	0.292	0.305	0.261
-80	0.406	0.373	0.185	0.276	0.299	0.242
-90	0.424	0.376	0.18	0.271	0.292	0.24
-100	0.432	0.399	0.182	0.272	0.283	0.237
-110	0.413	0.399	0.189	0.261	0.277	0.229
-120	0.338	0.399	0.207	0.264	0.281	0.241
-130	0.396	0.393	0.208	0.264	0.277	0.266
-140	-	-	0.212	0.275	0.279	0.272
-150	-	-	0.231	0.281	0.298	0.273
-160	-	-	0.247	0.312	0.309	0.279
-170	-	-	-	0.344	0.321	0.288
-180	-	-	-	0.32	0.365	0.302
-190	-	-	-	0.326	0.353	0.309
-200	-	-	-	0.353	0.352	0.325
-210	-	-	-	0.367	0.356	0.368
-220	-	-	-	0.37	0.38	0.365
-230	-	-	-	0.371	0.398	-
-240	-	-	-	-	0.413	-

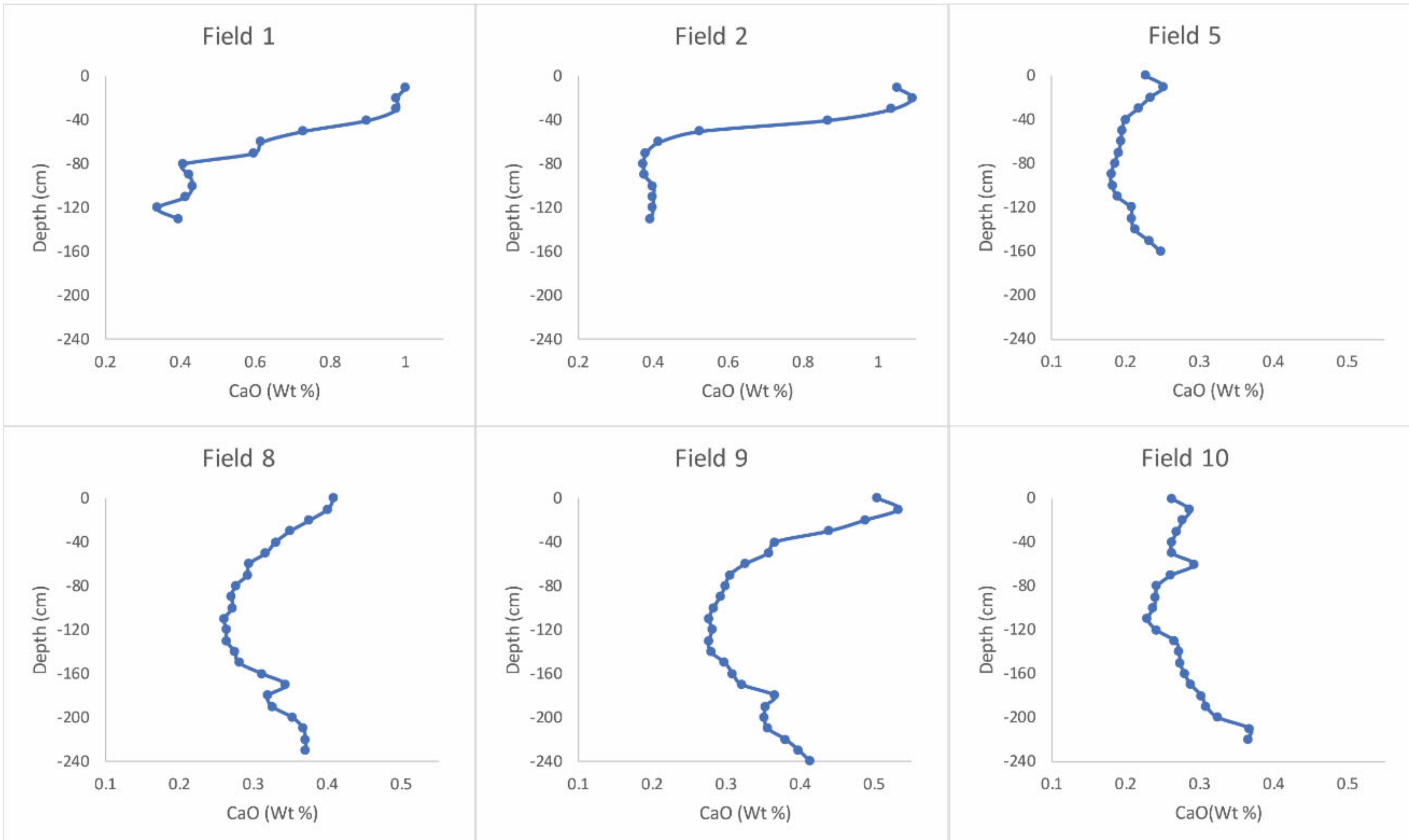

Figure C.6: The weight percent of CaO within the field profiles with depth (cm). Field 1 and Field 2 have a different scale due to higher values.

Table C.7

TiO_2 within the field profiles (Wt. %)

Depth	Field 1	Field 2	Field 5	Field 8	Field 9	Field 10
0	-	-	1.237	1.259	1.237	1.313
-10	1.068	1.029	1.245	1.257	1.231	1.301
-20	1.077	1.05	1.213	1.252	1.255	1.298
-30	1.071	1.054	1.211	1.233	1.25	1.319
-40	1.098	1.098	1.22	1.205	1.216	1.304
-50	1.137	1.125	1.204	1.172	1.196	1.309
-60	1.148	1.142	1.228	1.195	1.191	1.267
-70	1.128	1.131	1.251	1.19	1.191	1.176
-80	1.143	1.128	1.267	1.193	1.175	1.172
-90	1.15	1.147	1.276	1.204	1.197	1.191
-100	1.158	1.128	1.271	1.2	1.204	1.216
-110	1.152	1.144	1.24	1.193	1.198	1.226
-120	1.152	1.134	1.207	1.181	1.174	1.193
-130	1.152	1.134	1.197	1.174	1.185	1.143
-140	-	-	1.194	1.166	1.168	1.14
-150	-	-	1.175	1.167	1.153	1.142
-160	-	-	1.184	1.16	1.141	1.151
-170	-	-	-	1.116	1.143	1.147
-180	-	-	-	1.121	1.093	1.148
-190	-	-	-	1.152	1.122	1.136
-200	-	-	-	1.125	1.121	1.14
-210	-	-	-	1.099	1.103	1.112
-220	-	-	-	1.11	1.089	1.127
-230	-	-	-	1.093	1.072	-
-240	-	-	-	-	1.064	-

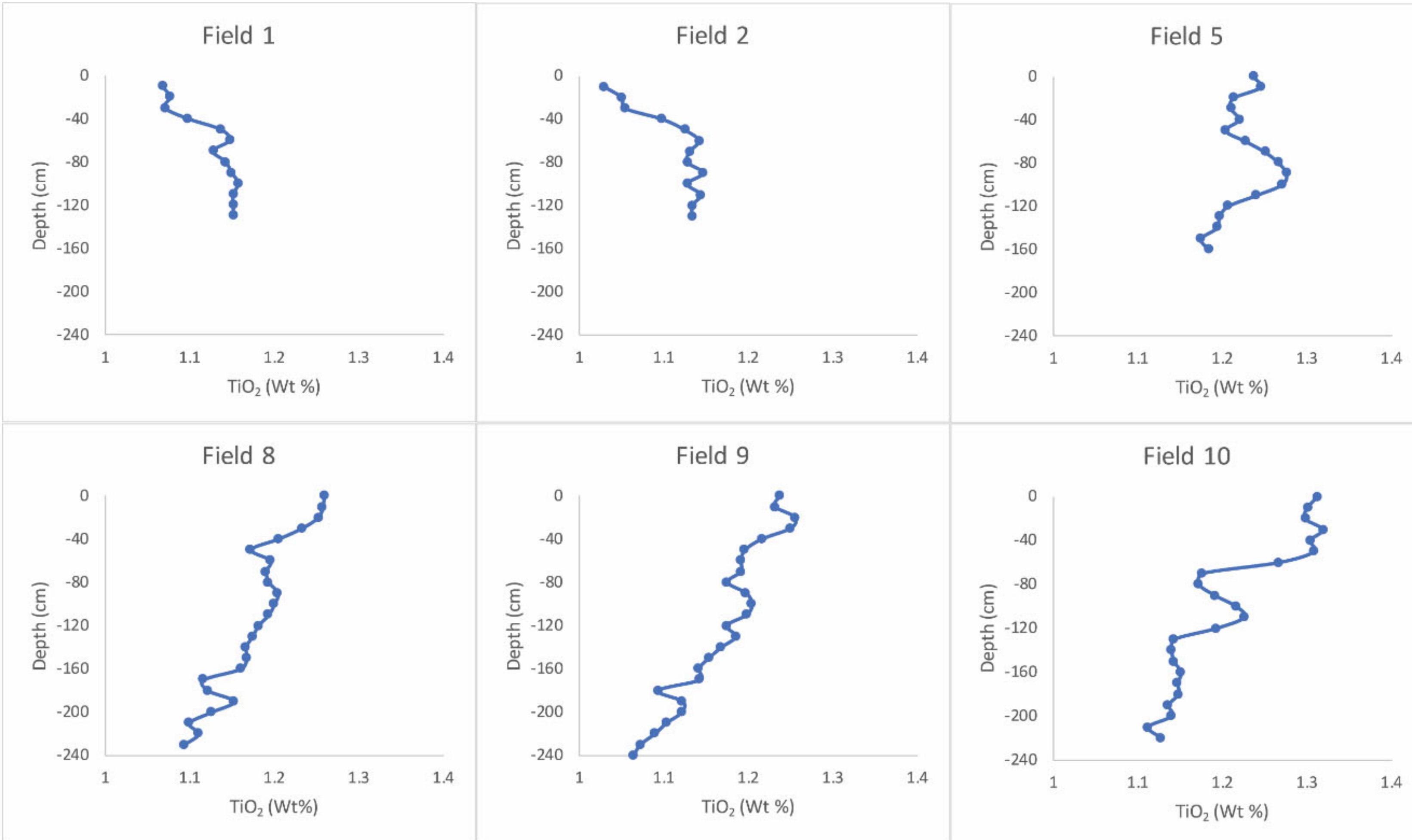

Figure C.7: The weight percent of TiO_2 with depth (cm) in the field profiles.

Table C.8

Fe_2O_3 within field profiles (Wt. %)

Depth	Field 1	Field 2	Field 5	Field 8	Field 9	Field 10
0	-	-	3.677	3.62	3.43	3.799
-10	4.905	5.344	3.849	4.057	3.557	3.195
-20	5.126	5.212	4.86	4.309	3.814	4.116
-30	5.076	5.276	5.246	4.783	4.249	4.266
-40	5.192	5.796	5.484	5.341	4.913	4.211
-50	5.922	7.351	5.711	5.718	5.144	4.437
-60	5.836	6.633	5.667	5.71	5.42	4.642
-70	6.229	6.995	5.535	5.69	5.681	5.696
-80	6.646	6.342	5.379	5.772	5.897	5.839
-90	6.434	6.701	5.249	5.762	5.761	5.935
-100	6.39	6.432	5.359	5.831	5.661	5.844
-110	6.658	6.278	5.352	5.701	5.799	5.619
-120	6.556	6.318	5.675	5.769	5.816	5.978
-130	6.169	6.554	5.704	5.869	5.782	6.39
-140	-	-	5.718	6.131	5.801	6.229
-150	-	-	5.775	6.064	5.982	6.411
-160	-	-	5.7	6.469	6.249	6.279
-170	-	-	-	6.952	6.168	6.358
-180	-	-	-	6.626	6.815	6.313
-190	-	-	-	5.983	6.368	6.102
-200	-	-	-	6.105	6.382	6.047
-210	-	-	-	6.019	6.343	5.997
-220	-	-	-	5.99	6.265	5.923
-230	-	-	-	6.156	6.581	-
-240	-	-	-	-	6.466	-

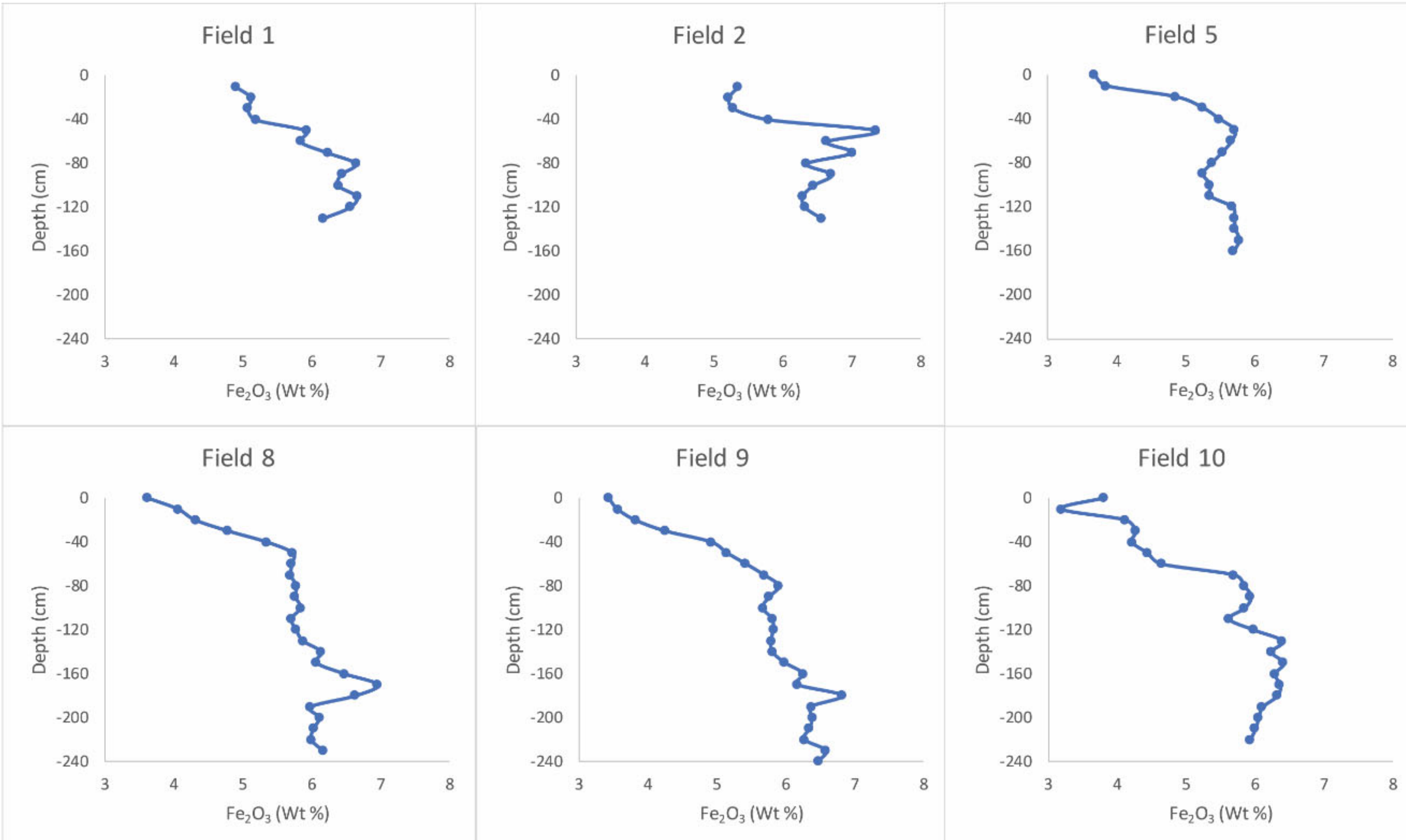

Figure C.8: The weight percent of Fe_2O_3 within the field profiles with depth (cm).

Table C.9

P_2O_5 within field profiles (Wt. %)

Depth	Field 1	Field 2	Field 5	Field 8	Field 9	Field 10
0	-	-	0.092	0.071	0.081	0.053
-10	0.073	0.069	0.082	0.065	0.065	0.06
-20	0.07	0.065	0.068	0.055	0.059	0.061
-30	0.069	0.059	0.058	0.05	0.052	0.045
-40	0.056	0.047	0.051	0.045	0.044	0.043
-50	0.045	0.04	0.049	0.048	0.043	0.038
-60	0.04	0.038	0.05	0.045	0.04	0.039
-70	0.041	0.04	0.053	0.047	0.043	0.04
-80	0.041	0.042	0.054	0.049	0.045	0.045
-90	0.041	0.04	0.053	0.047	0.048	0.045
-100	0.046	0.042	0.054	0.049	0.047	0.052
-110	0.05	0.043	0.058	0.05	0.049	0.059
-120	0.052	0.045	0.06	0.055	0.049	0.062
-130	0.051	0.045	0.061	0.058	0.051	0.064
-140	-	-	0.063	0.058	0.057	0.064
-150	-	-	0.06	0.063	0.052	0.07
-160	-	-	0.06	0.07	0.055	0.067
-170	-	-	-	0.067	0.058	0.067
-180	-	-	-	0.074	0.055	0.065
-190	-	-	-	0.064	0.056	0.064
-200	-	-	-	0.053	0.058	0.061
-210	-	-	-	0.062	0.062	0.056
-220	-	-	-	0.059	0.066	0.055
-230	-	-	-	0.059	0.06	-
-240	-	-	-	-	0.057	-

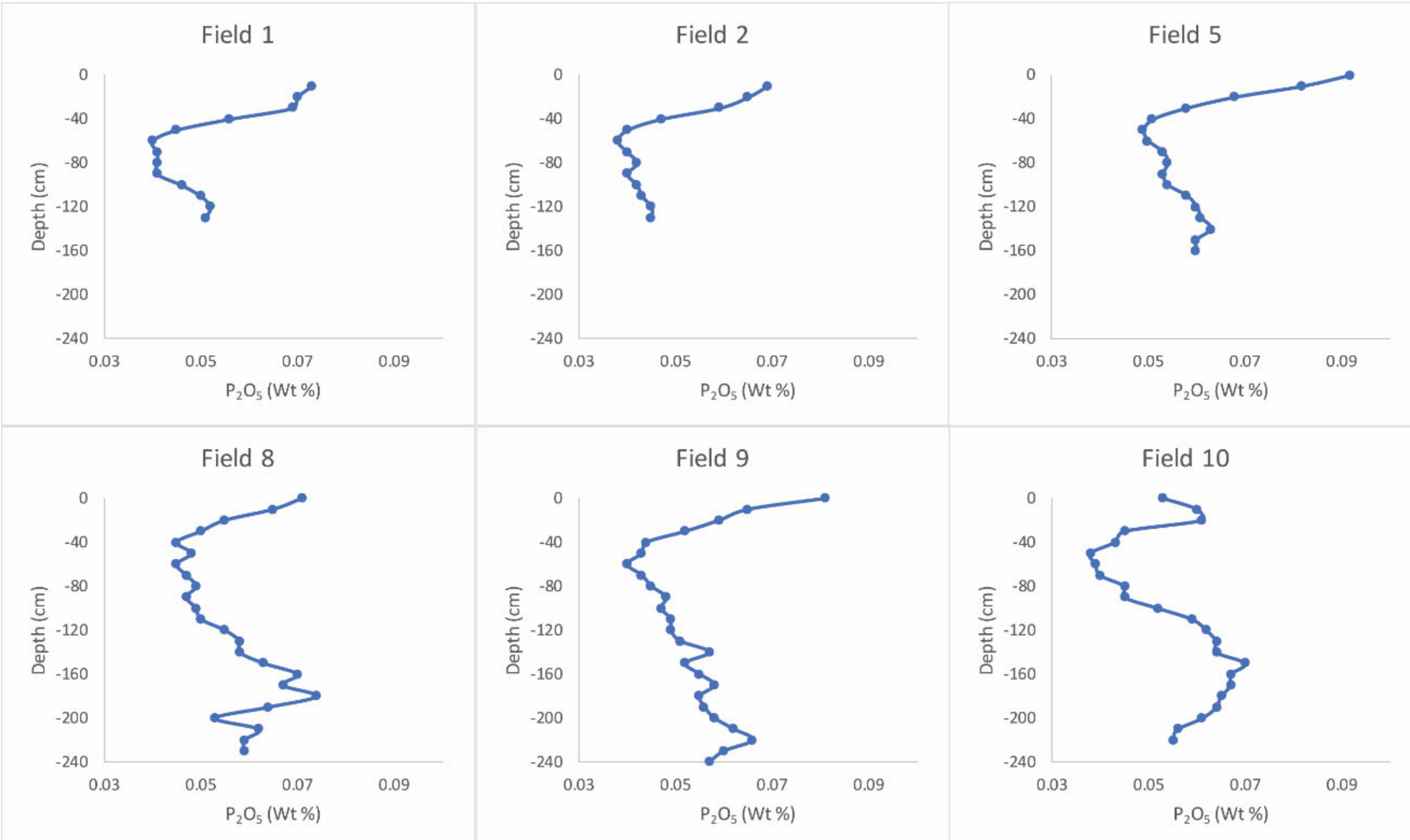

Figure C.9: The weight percent of P_2O_5 with depth (cm) in the field profiles.

Table C.10

Zr within the field profiles (ppm)

Depth	Field 1	Field 2	Field 5	Field 8	Field 9	Field 10
0	-	-	364	365	361	369
-10	274	265	360	363	365	375
-20	277	277	347	361	373	375
-30	280	271	330	349	362	368
-40	286	284	330	338	333	364
-50	295	286	317	323	339	362
-60	304	297	331	330	338	343
-70	295	285	348	320	321	309
-80	295	285	355	318	318	312
-90	296	294	354	325	328	319
-100	302	279	350	321	328	323
-110	283	287	330	310	315	342
-120	283	279	307	299	295	310
-130	288	260	292	286	302	260
-140	-	-	281	275	298	259
-150	-	-	281	277	279	254
-160	-	-	286	254	258	258
-170	-	-	-	224	259	251
-180	-	-	-	227	225	257
-190	-	-	-	259	243	260
-200	-	-	-	239	242	267
-210	-	-	-	237	235	263
-220	-	-	-	240	233	269
-230	-	-	-	240	229	-
-240	-	-	-	-	227	-

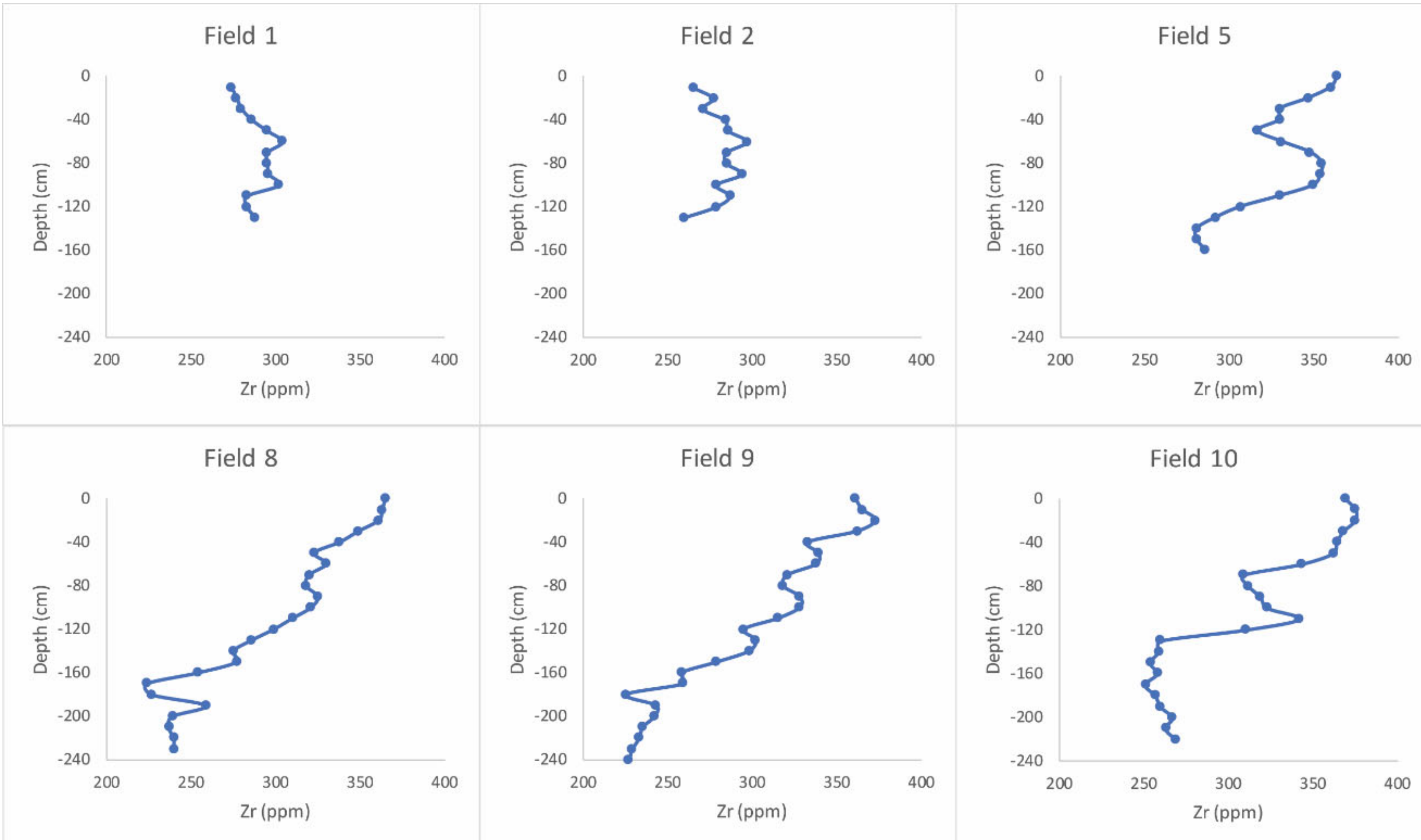

Figure C.10: The concentration of Zr (ppm) with depth (cm) within the field profiles.

Table C.11

NaO within the canal profiles (Wt. %)

Depth	Canal 5	Canal 8	Canal 9	Canal 10
0	0.362	0.35	0.368	0.374
-10	0.344	0.361	0.375	0.395
-20	0.352	0.361	0.403	0.403
-30	0.363	0.356	0.393	0.401
-40	0.33	0.345	0.397	0.39
-50	0.354	0.326	0.386	0.434
-60	0.36	0.325	0.39	-
-70	0.368	0.322	0.349	0.411
-80	0.361	0.332	0.358	0.449
-90	0.36	0.339	0.372	0.422
-100	0.339	0.348	0.359	0.444
-110	0.348	0.336	0.359	0.434
-120	0.348	0.328	-	0.394
-130	0.326	0.339	-	0.399
-140	0.347	0.315	0.374	0.4
-150	0.318	0.32	0.353	0.368
-160	0.442	0.354	0.352	0.371
-170	0.349	0.342	0.335	0.371
-180	0.433	0.332	0.336	0.341
-190	-	0.329	0.367	0.343
-200	-	0.329	0.385	0.352
-210	-	0.331	-	0.36
-220	-	-	-	0.371
-230	-	-	-	0.355
-240	-	-	-	0.372
-250	-	-	-	0.372
-260	-	-	-	0.36

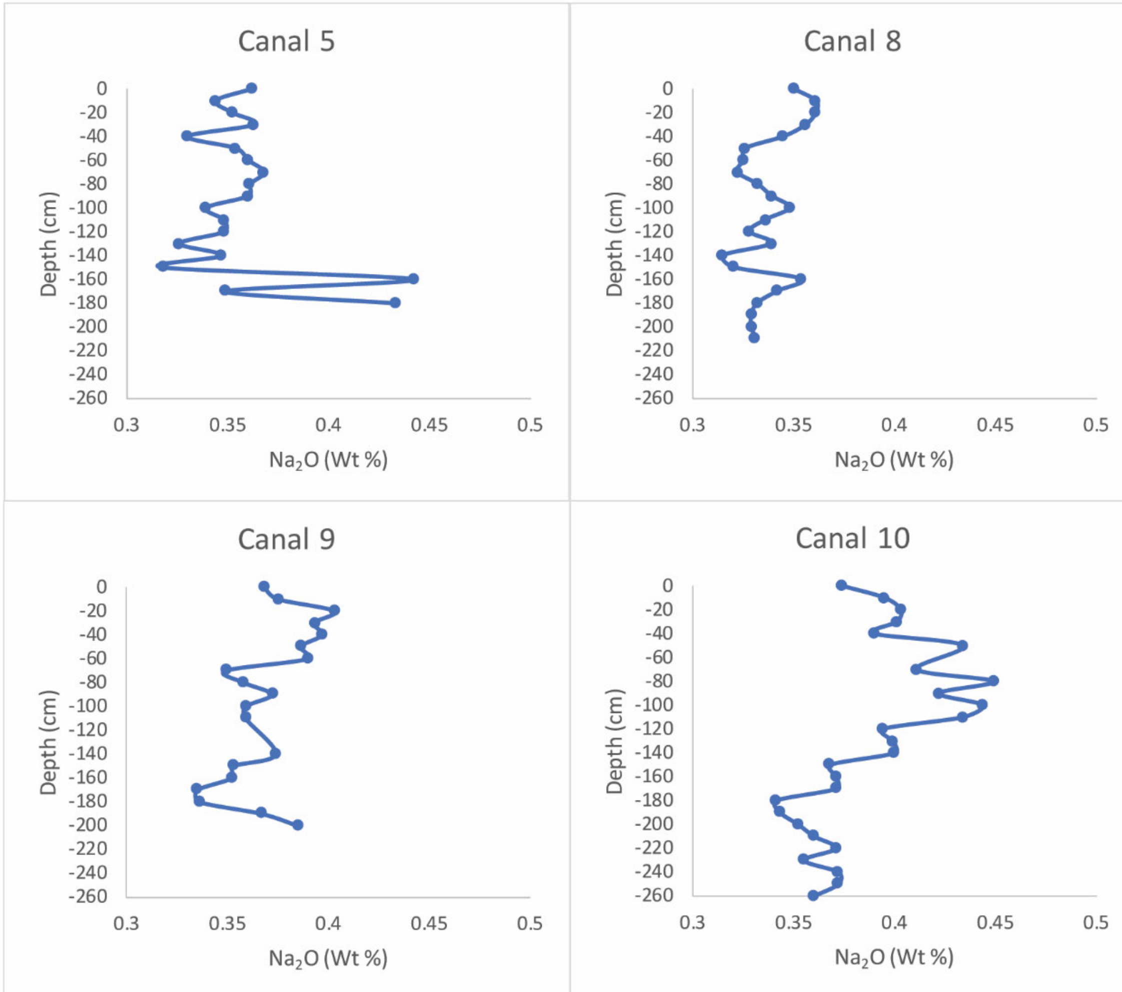

Figure C.11: The Na_2O within the canal profiles with depth (cm).

Table C.12

MgO within the canal profiles (Wt. %)

Depth	Canal 5	Canal 8	Canal 9	Canal 10
0	0.382	0.384	0.441	0.328
-10	0.376	0.382	0.446	0.34
-20	0.402	0.361	0.452	0.334
-30	0.444	0.346	0.466	0.349
-40	0.489	0.462	0.483	0.38
-50	0.5	0.514	0.476	0.41
-60	0.509	0.496	0.472	-
-70	0.485	0.506	0.457	0.468
-80	0.489	0.482	0.469	0.444
-90	0.506	0.513	0.46	0.457
-100	0.527	0.501	0.482	0.465
-110	0.547	0.501	0.489	0.473
-120	0.543	0.506	-	0.497
-130	0.534	0.543	-	0.507
-140	0.553	0.542	0.548	0.545
-150	0.565	0.574	0.579	0.529
-160	0.575	0.579	0.62	0.516
-170	0.578	0.588	0.673	0.537
-180	0.586	0.61	0.727	0.568
-190	-	0.613	0.684	0.583
-200	-	0.621	0.661	0.61
-210	-	0.671	-	0.572
-220	-	-	-	0.555
-230	-	-	-	0.57
-240	-	-	-	0.58
-250	-	-	-	0.592
-260	-	-	-	0.563

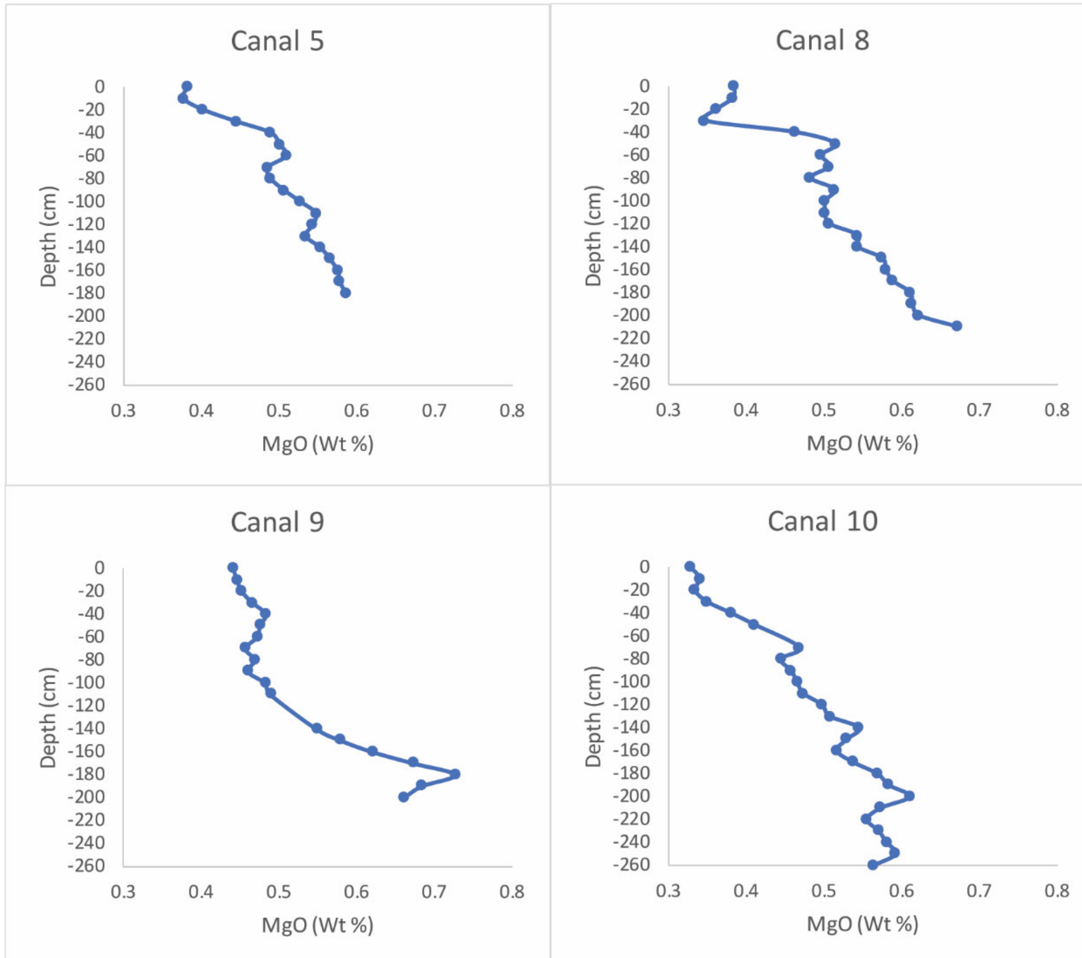

Figure C.12: The weight percent of MgO with depth (cm) in the canal profiles.

Table C.13

Al_2O_3 within the canal profiles (Wt. %)

Depth	Canal 5	Canal 8	Canal 9	Canal 10
0	11.033	10.554	12.335	10.221
-10	10.838	10.527	12.506	10.531
-20	11.965	10.335	12.807	10.445
-30	12.765	10.185	13.379	10.85
-40	14.309	13.178	14.248	12.039
-50	14.235	15.104	14.608	12.186
-60	14.507	14.997	14.913	-
-70	14.346	15.567	15.165	13.633
-80	14.149	14.804	15.195	12.821
-90	14.211	15.015	14.841	12.907
-100	14.972	15.033	14.785	12.889
-110	15.672	15.268	15.147	13.521
-120	15.66	15.99	-	14.057
-130	15.393	16.767	-	14.343
-140	15.411	17.795	16.429	15.42
-150	15.712	18.15	16.99	15.527
-160	15.606	16.962	17.487	15.415
-170	15.428	17.061	18.665	15.838
-180	15.337	17.288	20.057	16.353
-190	-	17.179	18.323	16.337
-200	-	16.985	17.077	16.857
-210	-	17.49	-	15.699
-220	-	-	-	15.073
-230	-	-	-	14.385
-240	-	-	-	14.214
-250	-	-	-	14.43
-260	-	-	-	13.965

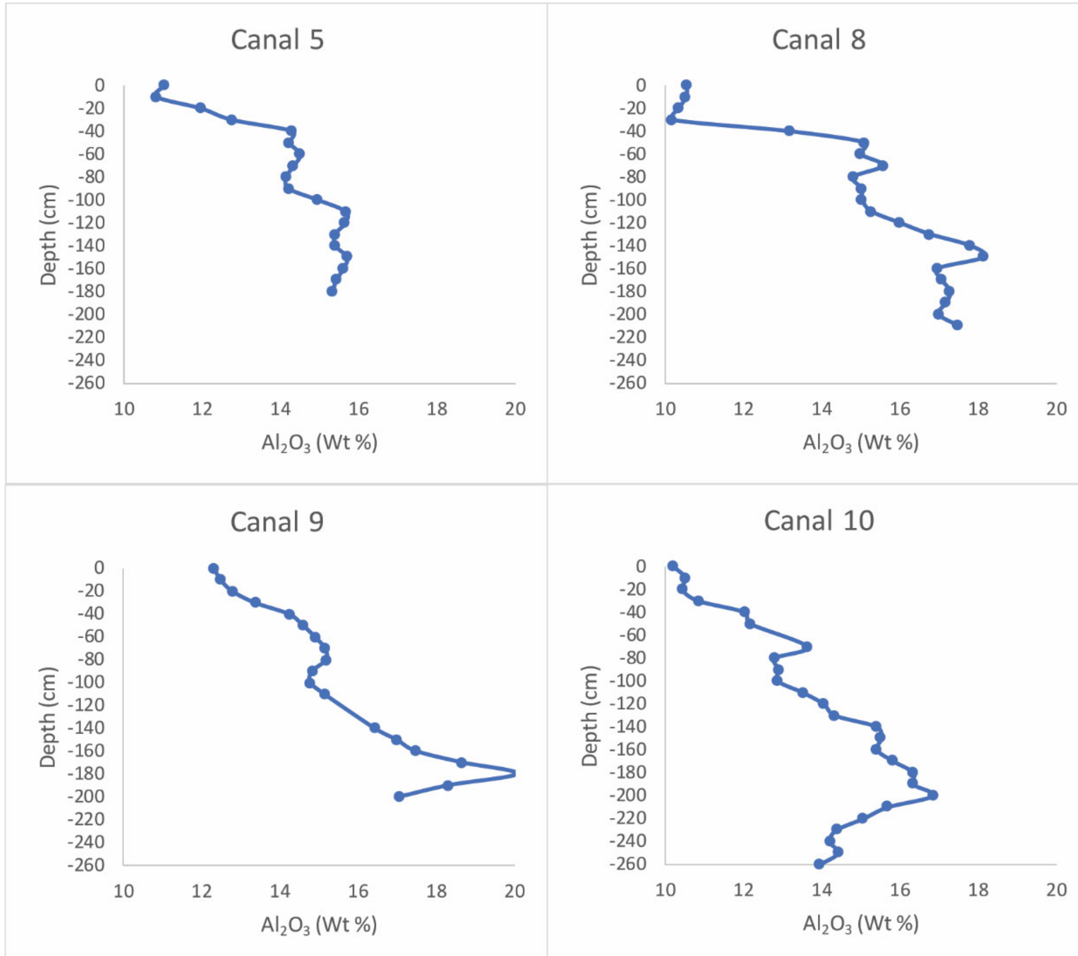

Figure C.13: The weight percent of Al_2O_3 with depth (cm) in the canal profiles.

Table C.14

SiO_2 within the canal profiles (Wt. %)

Depth	Canal 5	Canal 8	Canal 9	Canal 10
0	74.754	75.263	73.856	78.206
-10	74.89	76.569	73.139	77.721
-20	74.238	77.372	73.036	77.873
-30	74.21	78.218	72.916	77.259
-40	71.271	72.949	70.793	76.124
-50	71.273	69.431	71.409	76.14
-60	71.397	69.64	71.69	-
-70	71.043	69.641	70.625	73.583
-80	72.261	69.962	70.607	75.01
-90	72.521	70.742	71.489	74.338
-100	70.23	70.351	71.489	74.549
-110	68.981	69.743	71.3	74.365
-120	69.772	69.157	-	72.567
-130	70.026	67.745	-	71.722
-140	70.405	65.817	69.533	70.807
-150	69.585	66.462	67.909	69.606
-160	68.43	67.99	67.57	69.855
-170	69.408	67.606	65.234	69.389
-180	71.19	66.415	62.256	68.289
-190	-	67.976	65.574	68.356
-200	-	67.495	67.591	67.903
-210	-	66.122	-	69.495
-220	-	-	-	70.739
-230	-	-	-	72.152
-240	-	-	-	71.735
-250	-	-	-	71.421
-260	-	-	-	72.007

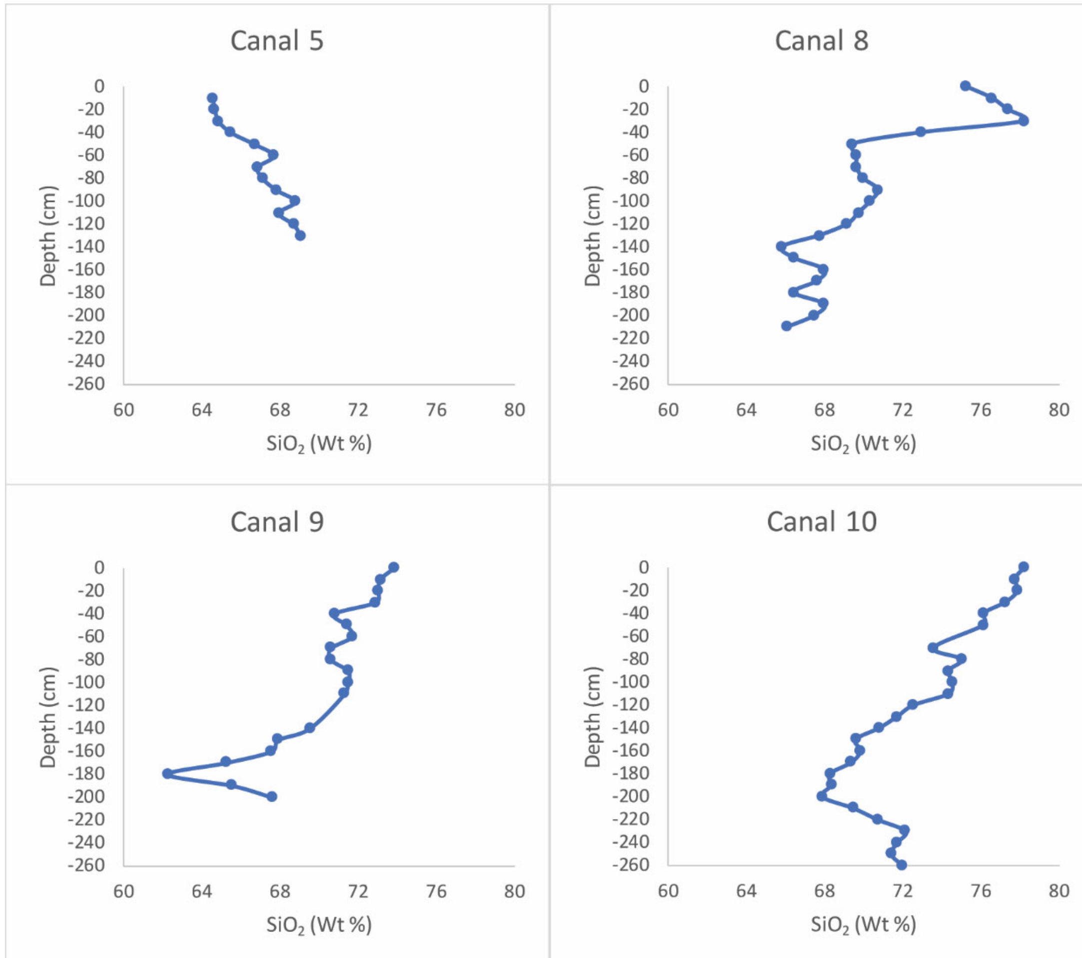

Figure C.14: The weight percent of SiO_2 with depth (cm) in the canal profiles.

Table C.15

K_2O within the canal profiles (Wt. %)

Depth	Canal 5	Canal 8	Canal 9	Canal 10
0	2.001	1.688	1.818	1.678
-10	1.94	1.674	1.857	1.736
-20	1.973	1.65	1.907	1.709
-30	2.082	1.701	2.014	1.797
-40	2.221	1.937	2.123	2.016
-50	2.216	2.104	2.177	2.047
-60	2.256	2.164	2.214	-
-70	2.214	2.274	2.223	2.199
-80	2.21	2.178	2.249	2.081
-90	2.236	2.242	2.23	2.102
-100	2.321	2.268	2.211	2.134
-110	2.44	2.275	2.272	2.183
-120	2.436	2.381	-	2.209
-130	2.386	2.497	-	2.287
-140	2.328	2.6	2.473	2.405
-150	2.29	2.675	2.544	2.371
-160	2.262	2.572	2.621	2.341
-170	2.285	2.577	2.76	2.413
-180	2.252	2.627	2.927	2.448
-190	-	2.597	2.78	2.4
-200	-	2.482	2.606	2.445
-210	-	2.476	-	2.265
-220	-	-	-	2.16
-230	-	-	-	1.956
-240	-	-	-	1.91
-250	-	-	-	1.969
-260	-	-	-	1.843

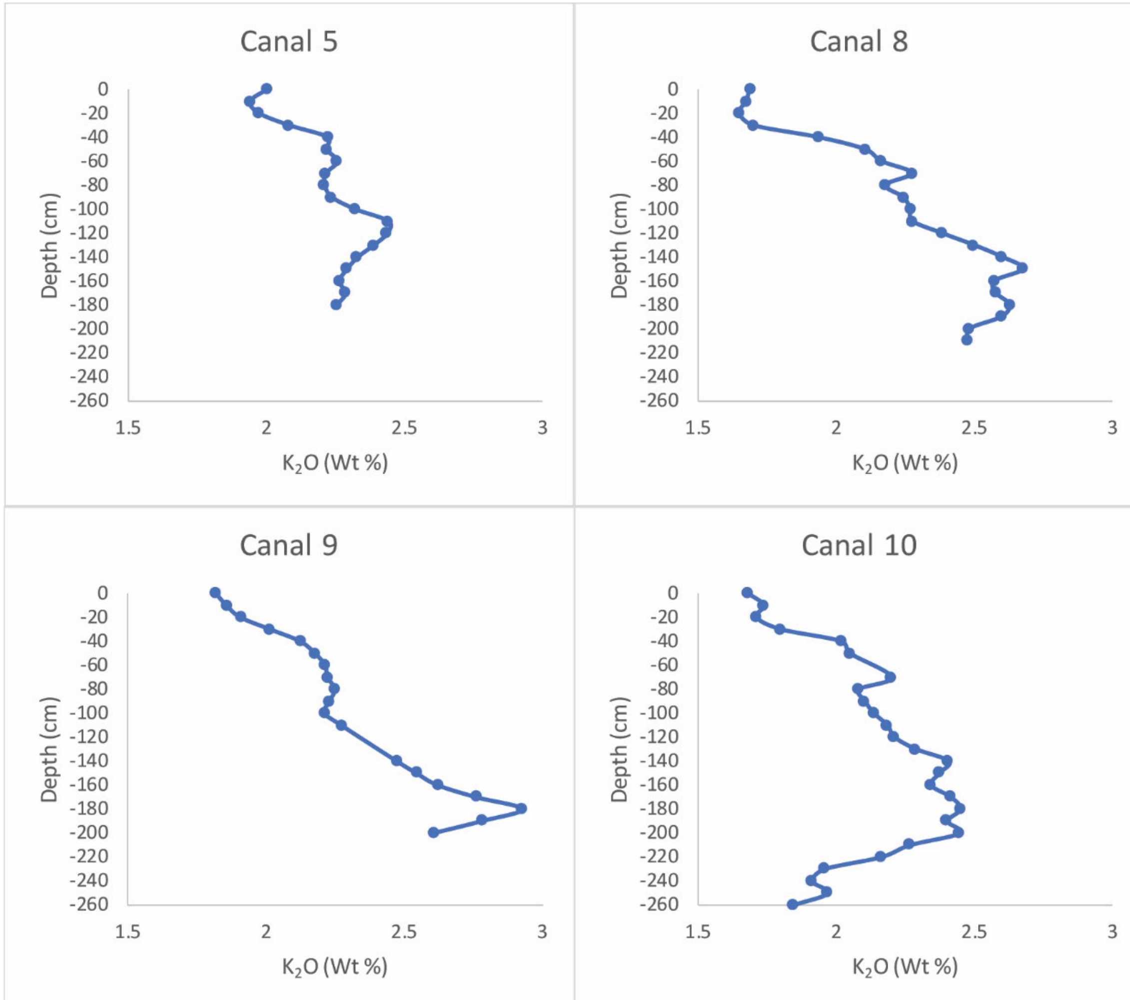

Figure C.15: The weight percent of K_2O with depth (cm) in the canal profiles.

Table C.16

CaO within the canal profiles (Wt. %)

Depth	Canal 5	Canal 8	Canal 9	Canal 10
0	0.226	0.478	0.48	0.241
-10	0.232	0.508	0.435	0.249
-20	0.233	0.491	0.429	0.245
-30	0.221	0.521	0.422	0.254
-40	0.229	0.528	0.37	0.259
-50	0.227	0.451	0.353	0.277
-60	0.222	0.393	0.333	-
-70	0.214	0.343	0.318	0.362
-80	0.208	0.332	0.32	0.349
-90	0.21	0.313	0.291	0.363
-100	0.22	0.322	0.295	0.367
-110	0.234	0.321	0.301	0.397
-120	0.243	0.325	-	0.391
-130	0.246	0.342	-	0.423
-140	0.279	0.363	0.328	0.429
-150	0.313	0.371	0.333	0.345
-160	0.326	0.352	0.352	0.291
-170	0.312	0.363	0.394	0.301
-180	0.336	0.387	0.443	0.33
-190	-	0.39	0.403	0.381
-200	-	0.395	0.378	0.395
-210	-	0.444	-	0.412
-220	-	-	-	0.422
-230	-	-	-	0.508
-240	-	-	-	0.523
-250	-	-	-	0.551
-260	-	-	-	0.564

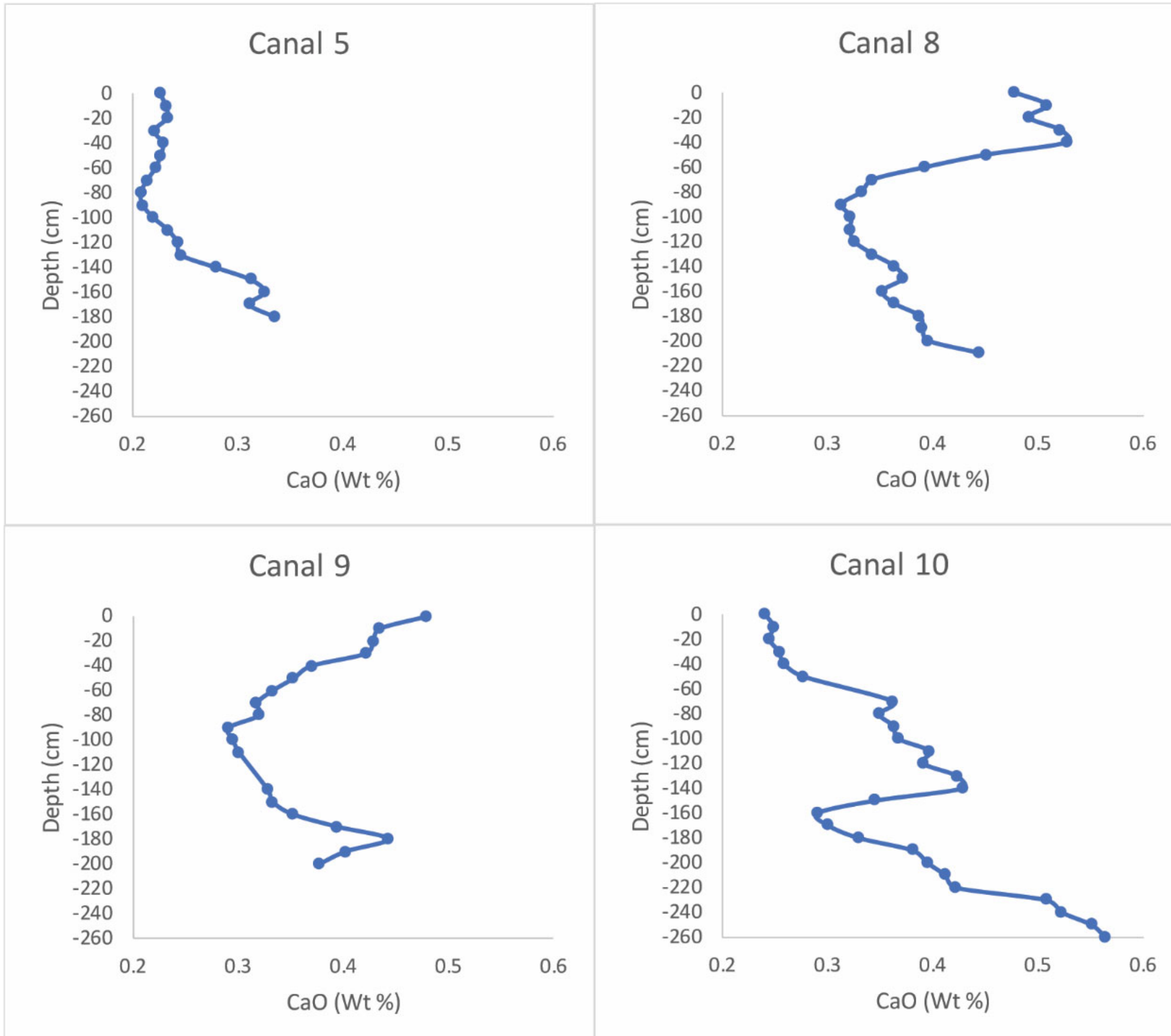

Figure C.16: The weight percent of CaO with depth (cm) in the canal profiles.

Table C.17

TiO_2 within the canal profiles (Wt. %)

Depth	Canal 5	Canal 8	Canal 9	Canal 10
0	1.23	1.252	1.219	1.312
-10	1.222	1.264	1.219	1.3
-20	1.235	1.272	1.22	1.303
-30	1.251	1.261	1.225	1.303
-40	1.208	1.214	1.191	1.322
-50	1.203	1.173	1.196	1.306
-60	1.207	1.169	1.198	-
-70	1.199	1.187	1.181	1.238
-80	1.213	1.184	1.194	1.253
-90	1.219	1.188	1.202	1.238
-100	1.181	1.194	1.211	1.236
-110	1.176	1.17	1.191	1.232
-120	1.177	1.161	-	1.203
-130	1.175	1.152	-	1.195
-140	1.176	1.133	1.16	1.186
-150	1.154	1.14	1.135	1.165
-160	1.141	1.126	1.148	1.176
-170	1.168	1.102	1.116	1.15
-180	1.187	1.103	1.081	1.125
-190	-	1.111	1.108	1.128
-200	-	1.09	1.123	1.118
-210	-	1.066	-	1.138
-220	-	-	-	1.146
-230	-	-	-	1.154
-240	-	-	-	1.132
-250	-	-	-	1.132
-260	-	-	-	1.138

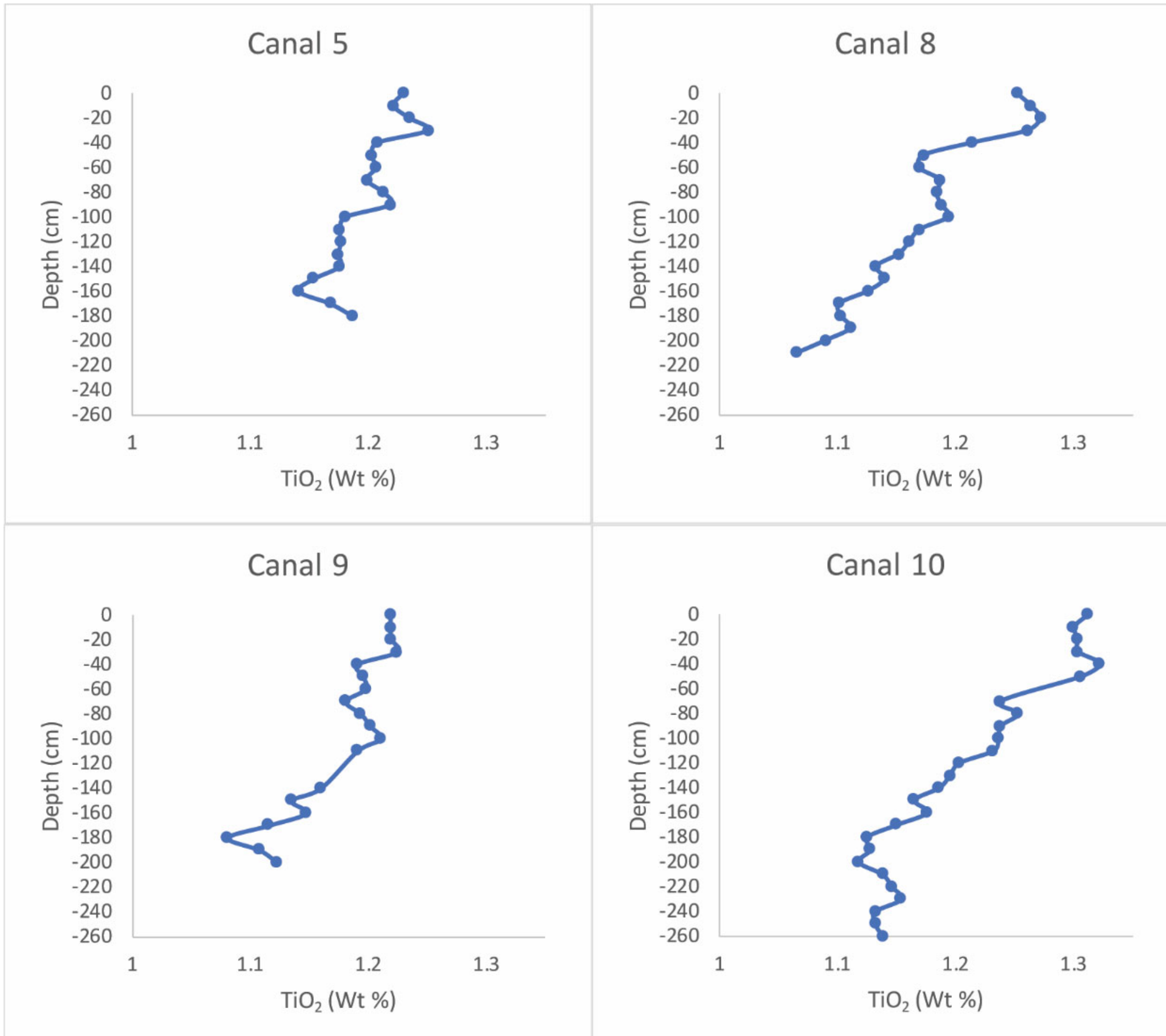

Figure C.17: The weight percent of TiO_2 with depth (cm) in the canal profiles.

Table C.18

Fe_2O_3 within the canal profiles (Wt. %)

Depth	Canal 5	Canal 8	Canal 9	Canal 10
0	3.761	3.678	4.201	2.947
-10	3.655	3.356	4.465	3.37
-20	4.595	3	4.606	3.419
-30	4.777	2.875	4.832	3.655
-40	5.377	4.624	5.284	3.961
-50	5.457	5.435	5.358	3.945
-60	5.447	5.561	5.488	-
-70	5.478	5.857	5.711	4.218
-80	5.306	5.671	5.842	4.224
-90	5.385	5.724	5.927	4.35
-100	5.701	5.741	5.736	4.263
-110	5.918	5.802	5.732	4.148
-120	5.742	5.967	-	4.712
-130	5.447	6.302	-	4.596
-140	5.435	6.599	6.113	4.731
-150	5.816	6.528	6.373	5.561
-160	5.999	6.185	6.472	5.84
-170	5.706	6.242	6.695	6.055
-180	5.38	6.201	7.208	5.966
-190	-	5.984	6.628	5.831
-200	-	6.115	6.123	6.085
-210	-	6.757	-	5.609
-220	-	-	-	5.317
-230	-	-	-	4.947
-240	-	-	-	5.11
-250	-	-	-	5.187
-260	-	-	-	4.935

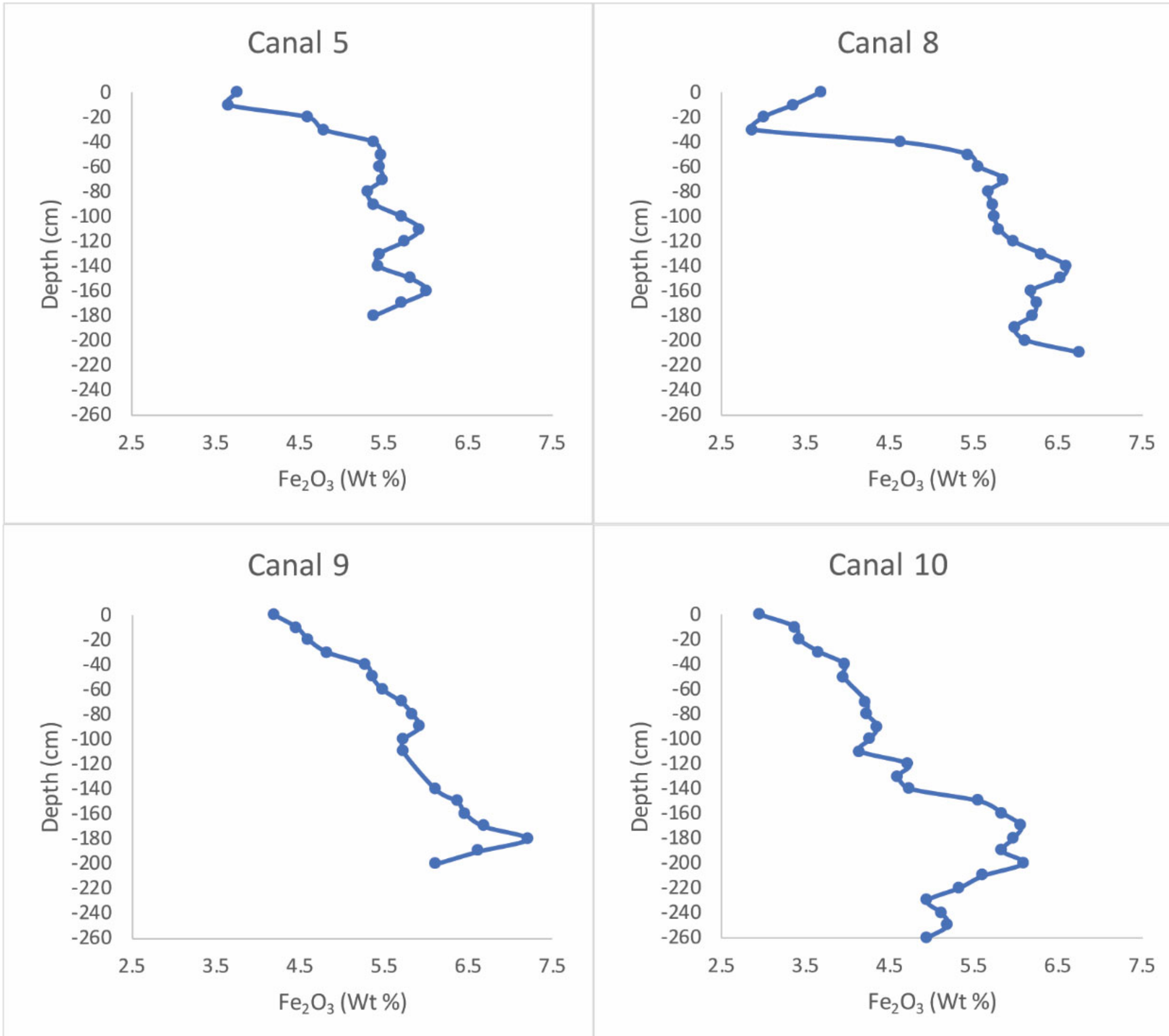

Figure C.18: The weight percent of Fe_2O_3 with depth (cm) in the canal profiles.

Table C.19

P_2O_5 within the canal profiles (Wt. %)

Depth	Canal 5	Canal 8	Canal 9	Canal 10
0	0.09	0.089	0.069	0.064
-10	0.084	0.08	0.062	0.061
-20	0.064	0.058	0.058	0.059
-30	0.05	0.051	0.051	0.054
-40	0.051	0.042	0.051	0.043
-50	0.052	0.047	0.044	0.038
-60	0.051	0.049	0.047	-
-70	0.051	0.05	0.045	0.037
-80	0.05	0.05	0.049	0.036
-90	0.06	0.052	0.05	0.041
-100	0.062	0.052	0.05	0.044
-110	0.064	0.052	0.049	0.04
-120	0.062	0.052	-	0.044
-130	0.057	0.053	-	0.053
-140	0.057	0.05	0.047	0.069
-150	0.06	0.053	0.05	0.075
-160	0.059	0.056	0.053	0.066
-170	0.058	0.053	0.053	0.07
-180	0.056	0.054	0.058	0.069
-190	-	0.055	0.062	0.061
-200	-	0.057	0.062	0.062
-210	-	0.054	-	0.053
-220	-	-	-	0.05
-230	-	-	-	0.042
-240	-	-	-	0.041
-250	-	-	-	0.042
-260	-	-	-	0.037

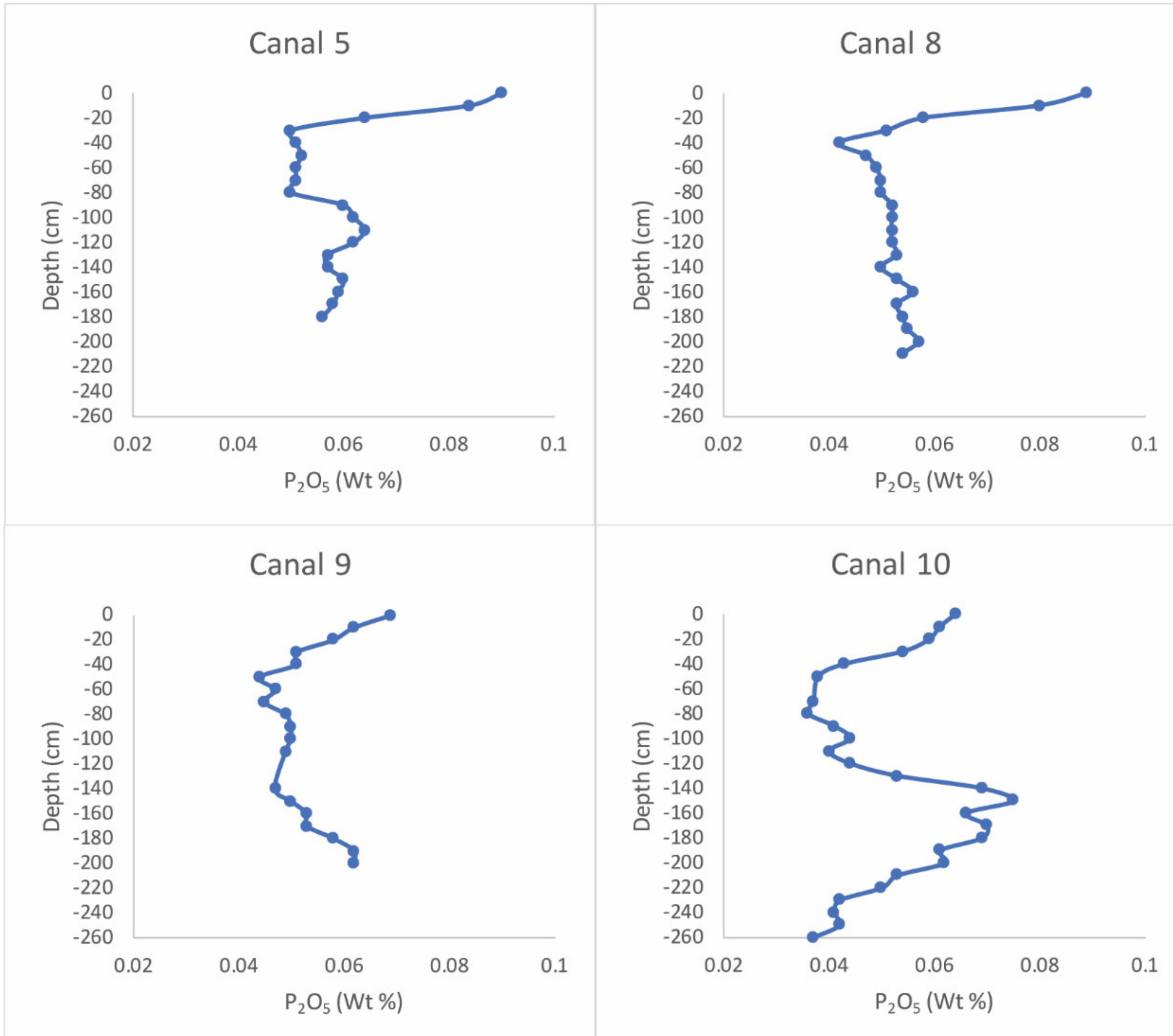

Figure C.19: The weight percent of P_2O_5 with depth (cm) in the canal profiles.

Table C.20

Zr within the canal profiles (ppm)

Depth	Canal 5	Canal 8	Canal 9	Canal 10
0	338	362	348	374
-10	345	367	339	369
-20	344	358	342	366
-30	345	345	343	360
-40	323	325	329	343
-50	326	295	334	345
-60	324	307	332	-
-70	316	306	308	306
-80	322	314	313	331
-90	314	316	326	323
-100	281	311	322	320
-110	270	293	311	320
-120	279	279	-	306
-130	279	265	-	289
-140	280	241	276	289
-150	281	243	255	286
-160	279	253	250	300
-170	284	246	231	275
-180	295	239	205	262
-190	-	251	230	269
-200	-	246	244	258
-210	-	238	-	277
-220	-	-	-	292
-230	-	-	-	312
-240	-	-	-	306
-250	-	-	-	299
-260	-	-	-	312

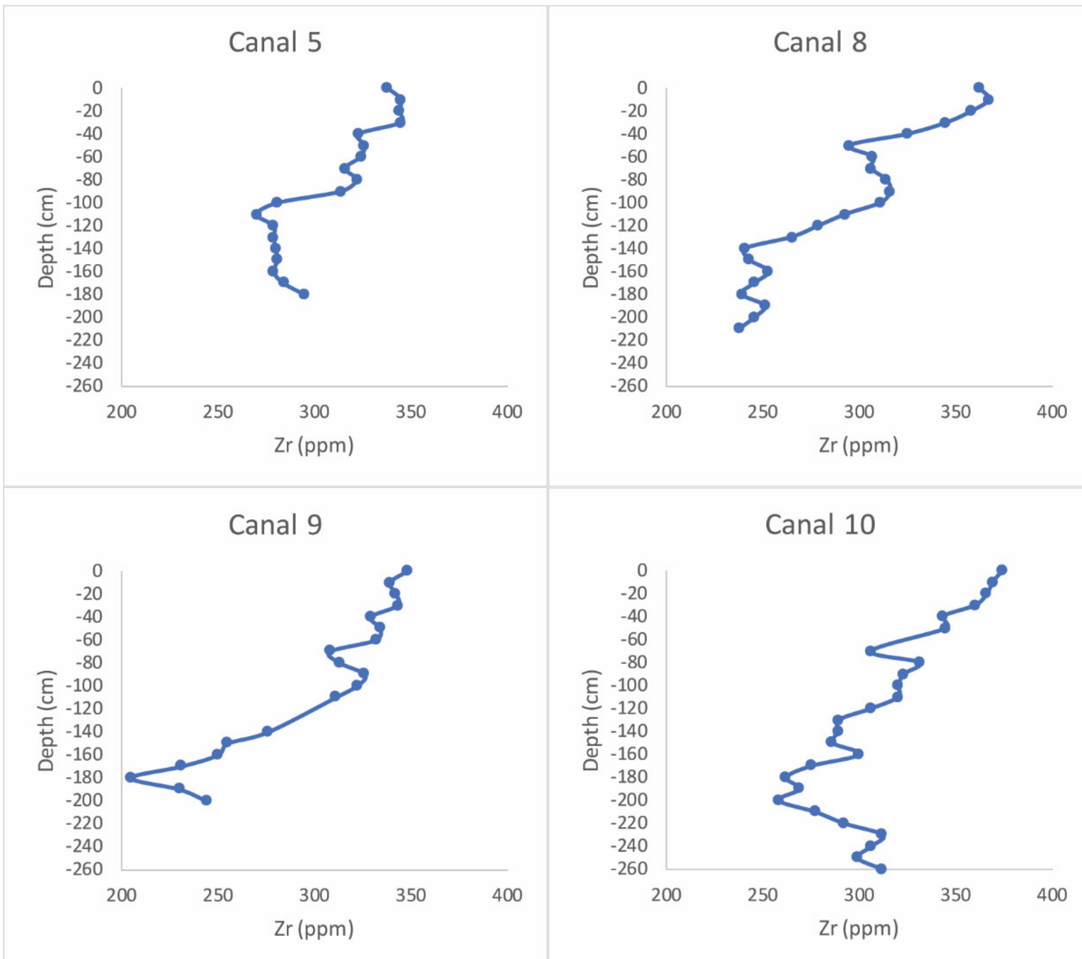

Figure C.20: The concentration of Zr (ppm) with depth in the canal profiles.

BIBLIOGRAPHY

Akers, P. D., G. A. Brook, L. B. Railsback, A. Cherkinksy, F. Liang, C. E. Ebert, J. A. Hoggarth, J. J. Awe, H. Cheng, and R. L. Edwards, 2019, Integrating U-Th, 14C, and 210PB methods to produce a Chronologically reliable isotope record for the Belize River valley Maya from A LOW-URANIUM STALAGMITE: The Holocene, v. 29, no. 7, p. 1234–1248, doi:10.1177/0959683619838047.

Audet, C. M., and J. J. Awe, 2001, What's cooking at Baking Pot: a report of the 2001 to 2003 seasons: Research Reports in Belizean Archaeology, v. 1, p. 49–59.

Balesdent, J., C. Girardin, and A. Mariotti, 1993, Site-Related ^(13)C of Tree Leaves and Soil Organic Matter in a Temperate Forest: Ecology, v. 74, no. 6, p. 1713–1721, doi:10.2307/1939930.

Beach, T., N. Dunning, S. Luzzadder-Beach, D. Cook, and J. Lohse, 2006, Impacts of the ancient Maya on soils and soil erosion in the central Maya Lowlands: Catena, v. 65, no. 2, p. 166–178, doi:10.1016/j.catena.2005.11.007.

Beach, T., S. Luzzadder-Beach, N. Dunning, and D. Cook, 2008, Human and natural impacts on fluvial and karst depressions of the Maya Lowlands: Geomorphology, v. 101, no. 1-2, p. 308–331, doi:10.1016/j.geomorph.2008.05.019.

Beach, T., S. Luzzadder-Beach, N. Dunning, J. Jones, J. Lohse, T. Guderjan, S. Bozarth, S. Millspaugh, and T. Bhattacharya, 2009, A review of human and natural changes in Maya Lowland wetlands over the Holocene: Quaternary Science Reviews, v. 28, no. 17-18, p. 1710–1724, doi:10.1016/j.quascirev.2009.02.004.

Beach, T., S. Luzzadder-Beach, R. Terry, N. Dunning, S. Houston, and T. Garrison, 2011, Carbon isotopic ratios of wetland and terrace soil sequences in the Maya Lowlands of Belize and Guatemala: Catena, v. 85, no. 2, p. 109–118, doi:10.1016/j.catena.2010.08.014.

Boutton, T. W., and S.-ichi Yamasaki, 1996, Stable carbon isotope ratios of soil organic matter and their use as indicators of vegetation and climate change, essay, *in* Mass spectrometry of soils: New York, New York, M. Dekker, p. 47–82.

Boutton, T. W., S.-ichi Yamasaki, and A. Mariotti, 1996, Measurement of soil organic matter turnover using 13C natural abundance , essay, *in* Mass spectrometry of soils: New York, New York, M. Dekker, p. 83–111.

Clercq, T. D. et al., 2015, Predicting soil organic matter stability in agricultural fields through carbon and nitrogen stable isotopes: Soil Biology and Biochemistry, v. 88, p. 29–38, doi:10.1016/j.soilbio.2015.05.011.

Coe, W., 1965, Tikal: Ten Years of Study of a Mayan Ruin in the Lowlands of Guatemala: Expedition, v. 7, p. 5–56.

Collins, M. E., B. J. Carter, B. G. Gladfelter, R. J. Southard, and J. S. Jacob, 1995, Archaeological Pedology in the Maya Lowlands: Pedological Perspectives in Archaeological Research SSSA Special Publication, p. 51–80, doi:10.2136/sssaspecpub44.c4.

Cowgill, U. M., 1962, An Agricultural Study of the Southern Maya Lowlands: American Anthropologist, v. 64, no. 2, p. 273–286, doi:10.1525/aa.1962.64.2.02a00030.

Dunning, N., T. Beach, P. Farrell, and S. Luzzadder-Beach, 1998, Prehispanic Agrosystems and Adaptive Regions in the Maya Lowlands: Culture Agriculture, v. 20, no. 2-3, p. 87–101, doi:10.1525/cag.1998.20.2-3.87.

Ebert, C. E., J. A. Hoggarth, and J. J. Awe, 2016, Integrating Quantitative Lidar Analysis and Settlement Survey in the Belize River Valley: Advances in Archaeological Practice, v. 4, no. 3, p. 284–300, doi:10.7183/2326-3768.4.3.284.

Ehleringer, J. R., N. Buchmann, and L. B. Flanagan, 2000, Carbon Isotope Ratios in Belowground Carbon Cycle Processes: Ecological Applications, v. 10, no. 2, p. 412, doi:10.2307/2641103.

Evans, N. P., T. K. Bauska, F. Gázquez-Sánchez, M. Brenner, J. H. Curtis, and D. A. Hodell, 2018, Quantification of drought during the collapse of the classic Maya civilization: Science, v. 361, no. 6401, p. 498–501, doi:10.1126/science.aas9871.

Farquhar, G., 1989, Carbon Isotope Discrimination And Photosynthesis: Annual Review of Plant Physiology and Plant Molecular Biology, v. 40, no. 1, p. 503–537, doi:10.1146/annurev.arplant.40.1.503.

Fedick, S. L., K. Pope, M. Pohl, and J. Jacob, 1996, Formation of ancient Maya wetland fields: Natural and anthropogenic processes, essay, *in* The managed mosaic: ancient Maya agriculture and resource use: Salt Lake City, Utah, Univ. of Utah Press, p. 165–176.

Fuller, G. D., and C. L. Lundell, 1937, The Vegetation of Peten: Ecology, v. 18, no. 4, p. 538, doi:10.2307/1930582.

Garber, J. F., J. M. Conlon, and T. G. Powis, 2004, Major Center Identifiers at a Plazuela Group near the Ancient Maya Site of Baking Pot, essay, *in* Ancient Maya of the Belize Valley Half a Century of Archaeological Research: Gainesville, Florida, University Press of Florida, p. 70–85.

Gischler, E., and A. J. Lomando, 1999, Recent sedimentary facies of isolated carbonate platforms, Belize-Yucatan system, Central America: Journal of Sedimentary Research, v. 69, no. 3, p. 747–763, doi:10.2110/jsr.69.747.

Golden, C. W., G. Borgstede, N. P. Dunning, and T. Beach, 2004, Noxious or Nurturing Nature? Maya Civilization in Environmental Context, essay, *in* Continuities and changes in Maya archaeology: perspectives at the millennium: New York, New York, Routledge, p. 111–126.

Gómez-Pompa Arturo, E. R. Boose, D. Foster, A. Barker Plotkin, and B. Hall, 2003, Geographical and historical variation in hurricanes across the Yucatan Peninsula., essay, *in* The Lowland Maya area: three millennia at the human-wildland interface: New York, New York, Haworth Press Bingham, p. 495–516.

Helmke, C., F. Sachse, J. J. Awe, J. A. Hoggarth, and C. Helmke, 2014, Prehistoric settlement patterns in the Upper Belize River Valley and their implications for models of Low-density urbanism, essay, *in* A celebration of the life and work of Pierre ROBERT COLAS: Munich, Bavaria, Verlag Anton Saurwein, p. 263–285.

Hoggarth, J. A., B. J. Culleton, J. J. Awe, and D. J. Kennett, 2014, Questioning Postclassic Continuity at Baking Pot, Belize, Using Direct AMS 14C Dating of Human Burials: Radiocarbon, v. 56, no. 3, p. 1057–1075, doi:10.2458/56.18100.

Hoggarth, J. A., B. S. F, C. B. J, C. E. Ebert, M. A. Masson, and D. J. Kennett, 2016, The political collapse of Chichén Itzá in climatic and cultural context: Global and Planetary Change, v. 138, p. 25–42.

Hoggarth, J. A., M. Restall, J. W. Wood, and D. J. Kennett, 2017, Drought and Its Demographic Effects in the Maya Lowlands: Current Anthropology, v. 58, no. 1, p. 82–113, doi:10.1086/690046.

Jenny, H., 1941, Factors of Soil Formation. A system of quantitative pedoogy: Soil Science, v. 52, no. 5, p. 415, doi:10.1097/00010694-194111000-00009.

Johnson, K. D., D. R. Wright, and R. E. Terry, 2007, Application of carbon isotope analysis to ancient maize agriculture in the Petexbatún region of Guatemala: Geoarchaeology, v. 22, no. 3, p. 313–336, doi:10.1002/gea.20155.

Kaplan, L., and T. F. Lynch, 1999, Phaseolus (Fabaceae) in Archaeology: AMS radiocarbon dates and their significance for Pre-Columbian agriculture: Economic Botany, v. 53, no. 3, p. 261–272, doi:10.1007/bf02866636.

Kennett, D. J. et al., 2012, Development and Disintegration of Maya Political Systems in Response to Climate Change: Science, v. 338, no. 6108, p. 788–791, doi:10.1126/science.1226299.

Kennett, D. J., and T. P. Beach, 2013, Archeological and environmental lessons for the Anthropocene from the Classic Maya collapse: Anthropocene, v. 4, p. 88–100, doi:10.1016/j.ancene.2013.12.002.

Keter, J. K. A., and P. M. Ahn, 2006, Profile characteristics, and form and surface activity of inorganic phosphorus in a deep red Kenya coffee soil (Nitosol): John Wiley & Sons, Ltd (10.1111): <http://onlinelibrary.wiley.com/doi/10.1111/j.1365-2389.1986.tb00010.x/abstract> (accessed October 25, 2019).

Kirke, C. M. S. G., 1980, Prehistoric agriculture in the Belize River valley: World Archaeology, v. 11, no. 3, p. 281–286, doi:10.1080/00438243.1980.9979767.

Lucero, L. J., J. D. Gunn, and V. L. Scarborough, 2011, Climate Change and Classic Maya Water Management: Water, v. 3, no. 2, p. 479–494, doi:10.3390/w3020479.

Markewich, H., and M. Pavich, 1991, Soil chronosequence studies in temperate to subtropical, low-latitude, low-relief terrain with data from the eastern United States: Geoderma, v. 51, no. 1-4, p. 213–239, doi:10.1016/0016-7061(91)90072-2.

Marshall, J. S., 2007, Geomorphology and physiographic provinces of Central America: Central America: Geology, Resources and Hazards, p. 75–122, doi:10.1201/9780203947043.pt2.

Martinelle, M., M. Holmquist, I. G. Clausen, S. Patkar, A. Svendsen, and K. Hult, 1996, The role of Glu87 and Trp89 in the lid of Humicola lanuginosa lipase: "Protein Engineering, Design and Selection", v. 9, no. 6, p. 519–524, doi:10.1093/protein/9.6.519.

Mathewson, K., 1984, Pulltrouser Swamp: Ancient Maya habitat, agriculture, and settlement in northern Belize: Journal of Historical Geography, v. 10, no. 4, p. 445–446, doi:10.1016/0305-7488(84)90097-5.

Medina-Elizalde, M., and E. J. Rohling, 2012, Collapse of Classic Maya Civilization Related to Modest Reduction in Precipitation: Science, v. 335, no. 6071, p. 956–959, doi:10.1126/science.1216629.

Meggers, B. J., 1954, Environmental Limitation on the Development of Culture: American Anthropologist, v. 56, no. 5, p. 801–824, doi:10.1525/aa.1954.56.5.02a00060.

Mi, G., F. Chen, L. Yuan, and F. Zhang, 2016, Ideotype Root System Architecture for Maize to Achieve High Yield and Resource Use Efficiency in Intensive Cropping Systems: Advances in Agronomy, p. 73–97, doi:10.1016/bs.agron.2016.05.002.

Piperno, D. R., A. J. Ranere, I. Holst, J. Iriarte, and R. Dickau, 2009, Starch grain and phytolith evidence for early ninth millennium B.P. maize from the Central Balsas River Valley, Mexico: Proceedings of the National Academy of Sciences, v. 106, no. 13, p. 5019–5024, doi:10.1073/pnas.0812525106.

Piperno, D. R., and B. D. Smith, 2012, The Origins of Food Production in Mesoamerica: Oxford Handbook of Mesoamerican Archaeology, p. 151–164, doi:10.1093/oxfordhb/9780195390933.013.0011.

Powers, J. S., and W. H. Schlesinger, 2002, Geographic and vertical patterns of stable carbon isotopes in tropical rain forest soils of Costa Rica: Geoderma, v. 109, no. 1-2, p. 141–160, doi:10.1016/s0016-7061(02)00148-9.

Retallack, G. J., 2001, Soils of the past: an introduction to paleopedology: Hoboken, New Jersey, John Wiley & Sons, Inc.

Sage, R. F., 2001, Environmental and evolutionary preconditions for the origin and diversification of the C_4 photosynthetic syndrome: Plant Biology, v. 3, no. 3, p. 202–213, doi:10.1055/s-2001-15206.

Sage, R. F., D. A. Wedin, and M. Li, 1999, The Biogeography of C_4 Photosynthesis: Patterns and Controlling Factors: C_4 Plant Biology, doi:10.1016/b978-012614440-6/50011-2.

Sharer, R. J., and L. P. Traxler, 2009, The ancient Maya: Stanford, California, Stanford University Press.

Sheldon, N. D., G. J. Retallack, and S. Tanaka, 2002, Geochemical Climofunctions from North American Soils and Application to Paleosols across the Eocene-Oligocene Boundary in Oregon: The Journal of Geology, v. 110, no. 6, p. 687–696, doi:10.1086/342865.

Siemens, A. H., and D. E. Puleston, 1972, Ridged Fields and Associated Features in Southern Campeche: New Perspectives on the Lowland Maya: American Antiquity, v. 37, no. 2, p. 228–239, doi:10.2307/278209.

Smith, B. D., 1997, The Initial Domestication of Cucurbita pepo in the Americas 10,000 Years Ago: Science, v. 276, no. 5314, p. 865–996, doi:10.1126/science.276.5314.932.

Soil Survey Staff, 2014, Natural Resources Conservation Service, United States Department of Agriculture. Official Soil Series Descriptions: Ultisol Soil Series. Available online.

Stinchcomb, G. E., L. C. Nordt, S. G. Driese, W. E. Lukens, F. C. Williamson, and J. D. Tubbs, 2016, A data-driven spline model designed to predict paleoclimate using paleosol geochemistry: American Journal of Science, v. 316, no. 8, p. 746–777, doi:10.2475/08.2016.02.

Szpak, P., 2014, Complexities of nitrogen isotope biogeochemistry in plant-soil systems: implications for the study of ancient agricultural and animal management practices: Frontiers in Plant Science, v. 5, doi:10.3389/fpls.2014.00288.

Taiz, L., and E. Zeiger, 1998, Plant physiology: Sunderland, MA, Sinauer Associates.

Tate, K. R., and I. Salcedo, 1988, Phosphorus control of soil organic matter accumulation and cycling: Biogeochemistry, v. 5, no. 1, p. 99–107, doi:10.1007/bf02180319.

Tieszen, L. L., and T. Fagre, 1993, Carbon Isotopic Variability in Modern and Archaeological Maize: Journal of Archaeological Science, v. 20, no. 1, p. 25–40, doi:10.1006/jasc.1993.1002.

Tipple, B. J., and M. Pagani, 2007, The Early Origins of Terrestrial C_4 Photosynthesis: Annual Review of Earth and Planetary Sciences, v. 35, no. 1, p. 435–461, doi:10.1146/annurev.earth.35.031306.140150.

Turner, B. L., 1974, Prehistoric Intensive Agriculture in the Mayan Lowlands: Science, v. 185, no. 4146, p. 118–124, doi:10.1126/science.185.4146.118.

Turner, B. L., and P. D. Harrison, 1981, Prehistoric Raised-Field Agriculture in the Maya Lowlands: Science, v. 213, no. 4506, p. 399–405, doi:10.1126/science.213.4506.399.

Wahl, D., R. Byrne, T. Schreiner, and R. Hansen, 2007, Palaeolimnological evidence of late-Holocene settlement and abandonment in the Mirador Basin, Peten, Guatemala: The Holocene, v. 17, no. 6, p. 813–820, doi:10.1177/0959683607080522.

Webb, E. A., H. P. Schwarcz, and P. F. Healy, 2004, Detection of ancient maize in lowland Maya soils using stable carbon isotopes: evidence from Caracol, Belize: Journal of Archaeological Science, v. 31, no. 8, p. 1039–1052, doi:10.1016/j.jas.2004.01.001.

Willey, G. E., R. Wauchope, and E. W. Andrews IV, 1965, Archaeology and Prehistory in the Northern Lowlands, essay, *in* Archaeology of southern Mesoamerica: part 1: Austin, Texas, University of Texas Press, p. 288–330.

Wood, W. R., and D. L. Johnson, 1978, Advances in Archaeological Method and Theory: Academic Press, v. 1, p. 315–381, doi:10.1016/c2013-0-07001-6.

Wright, D. R., R. E. Terry, and M. Eberl, 2009, Soil properties and stable carbon isotope analysis of landscape features in the Petexbatún region of Guatemala: Geoarchaeology, v. 24, no. 4, p. 466–491, doi:10.1002/gea.20275.

Yaeger, J., 2008, Charting the collapse: Late classic to postclassic population dynamics in the Mopan Valley, Belize: Research Reports in Belizean Archaeology, v. 5, p. 13–21.

Zhu, J., S. M. Kaeppler, and J. P. Lynch, 2005, Topsoil foraging and phosphorus acquisition efficiency in maize (Zea mays): Functional Plant Biology, v. 32, no. 8, p. 749, doi:10.1071/fp05005.